ERDC/GSL TR-20-13

Geotechnical and Structures Laboratory

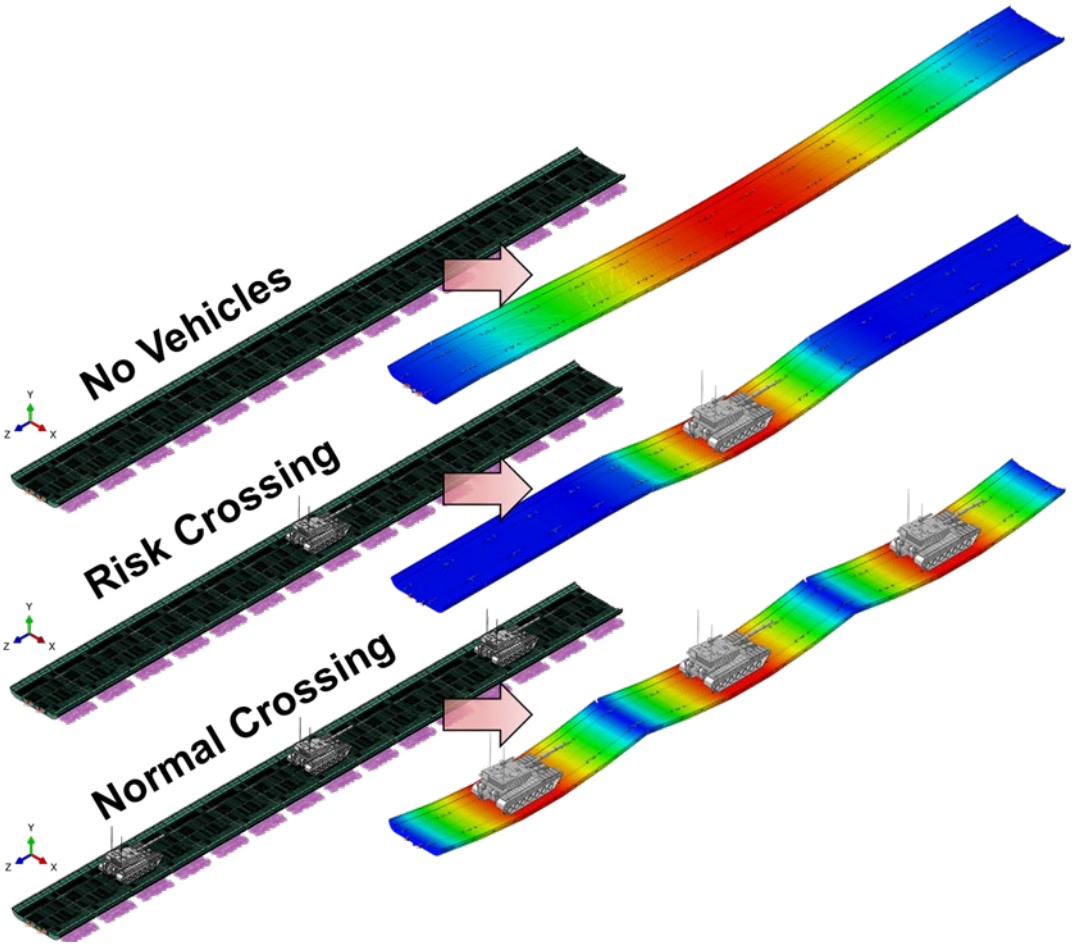
US Army Corps
of Engineers®
Engineer Research and
Development Center

ERDC
ENGINEER RESEARCH & DEVELOPMENT CENTER

Structural Analysis of an Improved Ribbon Bridge Subjected to Hydrodynamic and Vehicular Loading

M. Wesley Trim and Joseph A. Padula

April 2020



Approved for public release; distribution is unlimited

The US Army Engineer Research and Development Center (ERDC) solves the nation's toughest engineering and environmental challenges. ERDC develops innovative solutions in civil and military engineering, geospatial sciences, water resources, and environmental sciences for the Army, the Department of Defense, civilian agencies, and our nation's public good. Find out more at www.erdc.usace.army.mil.

To search for other technical reports published by ERDC, visit the ERDC online library at http://acwc.sdp.sirsi.net/client/default.

ERDC/GSL TR-20-13
April 2020

Structural Analysis of an Improved Ribbon Bridge Subjected to Hydrodynamic and Vehicular Loading

M. Wesley Trim and Joseph A. Padula

Geotechnical and Structures Laboratory
US Army Engineer Research and Development Center
3909 Halls Ferry Road
Vicksburg, MS 39180-6199

Final report

Approved for public release; distribution is unlimited

Prepared for Assistant Product Manager/Project Officer
Office of the Product Manager, Bridging
SFAE-CSS-FP-H, Bldg 230, Mail Stop #401
6501 East 11 Mile Road
Warren, MI 48397-5000

Under US Army, PdM Bridging; MIPR 11326139; Project No. 464569

Abstract

Structural modeling and simulations were performed to determine limit states of an Improved Ribbon Bridge (IRB) subjected to hydraulic and vehicle loadings. Measurements of as-built IRB bays were used to construct a three-dimensional, computer-aided design model. The model was used to create a computational finite element model (FEM) that was validated through correlations of simulation results and empirical data. The validated FEM was used to establish limit states (i.e., maximum current and vehicular loading conditions for 110 and 210 m IRB crossings).

Analyses revealed that the primary structural failure mode was yielding in the steel pins that link IRB bays. Assuming the IRB is adequately restrained at the shores, a 110 m IRB can withstand currents up to 11 ft/s with no vehicle traffic; a 210 m IRB can endure up to 7 ft/s under the same conditions. For risk crossings, one Military Load Classification-70 vehicle on the bridge, 110 and 210 m IRBs can tolerate currents up to 9 and 7 ft/s, respectively. Under normal crossing conditions vehicle spaced 100 ft apart, a 110 m IRB has the structural capacity to endure currents up to 9 ft/s; the maximum current for a 210 m IRB is 5 ft/s.

DISCLAIMER: The contents of this report are not to be used for advertising, publication, or promotional purposes. Citation of trade names does not constitute an official endorsement or approval of the use of such commercial products. All product names and trademarks cited are the property of their respective owners. The findings of this report are not to be construed as an official Department of the Army position unless so designated by other authorized documents.

DESTROY THIS REPORT WHEN NO LONGER NEEDED. DO NOT RETURN IT TO THE ORIGINATOR.

Contents

Abstract ii

Figures and Tables v

Preface x

1 Introduction 1

1.1 Background 1
1.2 Objective 2
1.3 Approach 2

2 Computational Modeling Methodology 3

2.1 Structural Improved Ribbon Bridge (IRB) computer-aided design (CAD) model development 3
2.2 Structural IRB finite element model development 10

3 Structural IRB Finite Element Model (FEM) Validation 18

3.1 Structural response validation 18
3.1.1 Structural response validation methodology 18
3.1.2 Correlation between experimental and simulated test results 27
3.1.3 Structural response correlation summary 40
3.2 Hydrodynamic loading approach and validation 40
3.2.1 Hydrodynamic loading approach for the IRB structural analysis 41
3.2.2 Hydrodynamic loading validation methodology 42
3.2.3 Six-bay raft push test/simulation correlation 47

4 Structural Analysis of the IRB Subjected to Hydrodynamic and Vehicular Loading 50

4.1 Structural analysis methodology 50
4.1.1 Analysis cases 50
4.1.2 IRB FEM conditioning procedure 51
4.1.3 Determination of allowable limits 54
4.2 Structural analysis of the 15-bay (110 m) IRB 58
4.2.1 Draft (vertical displacement) of the 15-bay IRB 59
4.2.2 Drag loading on the 15 bay IRB 60
4.2.3 Drag-induced displacement for the 15-bay IRB 63
4.2.4 Limit states for the 15-bay IRB 66
4.3 Structural analysis of the 30 bay (210 meter) IRB 79
4.3.1 Draft (vertical displacement) of the 30 bay IRB 80
4.3.2 Drag loading on the 30 bay IRB 82
4.3.3 Drag induced displacement for the 30-bay IRB 85
4.3.4 Limit states for the 30-bay IRB 88

5 Summary and Conclusions 102

References 104

Unit Conversion Factors 105

Acronyms and Abbreviations 106

Report Documentation Page

Figures and Tables

Figures

Figure 1. Unloading IRB bays at ERDC. 3
Figure 2. CAD modeling of an IRB interior bay at ERDC. 4
Figure 3. Interior IRB bay with access panels and lower main coupling removed. 4
Figure 4. IRB main coupling. 5
Figure 5. IRB inner ponton with skin-plate cutouts. 6
Figure 6. Outer ponton with skin-plate cutouts. 6
Figure 7. Interior of IRB bay at main coupling connection. 7
Figure 8. Ultrasonic thickness measurement of an interior stiffener. 7
Figure 9. Deck of interior ponton with top deck plate removed. 8
Figure 10. IRB interior bay CAD model showing interior details. 9
Figure 11. IRB interior bay CAD model overview with dimensions. 9
Figure 12. Inner ponton finite element mesh: (a) isometric view and (b) isometric view with deck removed to show interior structure. 11
Figure 13. Outer ponton finite element mesh: (a) isometric view and (b) isometric view with deck removed to show interior structure. 12
Figure 14. Shell-to-solid couplings on the outer and inner ponton mesh subassemblies. 13
Figure 15. IRB single bay finite element mesh showing shell element section thicknesses: (a) isometric view and (b) isometric section view below the deck, showing interior structure. Units are inches. 14
Figure 16. Multipoint constraint (spider element) locations on the inner and outer ponton FEMs. 15
Figure 17. Inner ponton (IP) to outer ponton (OP) connectors. 15
Figure 18. Interactions between adjacent IRB bays. 17
Figure 19. Complete IRB bridge mesh. 17
Figure 20. One-bay and two-bay test configurations in the structural response validation test series (Trim and Bennett 2018). 19
Figure 21. Structural response validation test arrangement and instrumentation overview for the one-bay configuration (a) from above, (b) from below, and (c) from end (Trim and Bennett 2018). 20
Figure 22. Structural response validation test arrangement and instrumentation overview for the two-bay configuration (a) from above, (b) from below, and (c) from end (Trim and Bennett 2018). 20
Figure 23. Load arrangements for one-bay structural response tests 1-1, 1-2, and 1-3 (Trim and Bennett (2018). 21
Figure 24. Load arrangements for two-bay structural response tests 2-1, 2-2, and 2-3 (Trim and Bennett 2018). 22
Figure 25. Schematic used for calculating principal stress/strain from rosette. 23

Figure 26. Single-bay structural response FEM. 26
Figure 27. Two-bay structural response FEM. 27
Figure 28. Test-versus-simulation comparison of reaction forces at supports for single-bay structural response tests. 28
Figure 29. Test-versus-simulation comparison of displacement measurements for single-bay structural response tests. 29
Figure 30. Test-versus-simulation comparison of axial stress, σzz, measurements for single bay structural response tests. 30
Figure 31. Test-versus-simulation comparison of von Mises stress, σvm, measurements for single-bay structural response tests. 31
Figure 32. Test versus simulation comparison of reaction forces at supports for dual bay structural response tests. 33
Figure 33. Test-versus-simulation comparison of pin connector forces between bays for dual-bay structural response tests. 34
Figure 34. Test-versus-simulation comparison of displacement measurements for dual-bay structural response tests. 35
Figure 35. Test-versus-simulation comparison of axial stress, σzz, measurements for dual-bay tests. 36
Figure 36. Test-versus-simulation comparison of von Mises stress, σvm, measurements for dual bay-structural response tests. 37
Figure 37. Six-bay IRB raft push test arrangement. 43
Figure 38. Photograph of six-bay IRB raft push test arrangement. 43
Figure 39. Six-bay raft instrumentation overview (Waller et al. 2018). 45
Figure 40. Six-bay IRB raft push test FEM. 46
Figure 41. Draft (*z*-displacement) test versus simulation comparison of the six-bay raft for tanks-empty and tanks-full conditions. 48
Figure 42. Drag force on six bay IRB raft: test versus simulation comparison for (a) tanks-empty condition and (b) tanks-full condition. 49
Figure 43. Overview of 15-bay (110 m) IRB bridge FEMs illustrating the three vehicular loading cases (no vehicles, risk crossing, and normal crossing), boundary conditions, and applied drag loading. 53
Figure 44. Overview of 30-bay (210 m) IRB bridge FEMs illustrating the three vehicular loading cases (no vehicles, risk crossing, and normal crossing), boundary conditions, and applied drag loading. 54
Figure 45. Tensile test results for the four ASTM-E8 specimens harvested from main coupling pin. 55
Figure 46. Lower main coupling pin connection schematic and load diagram. 56
Figure 47. Shear force and bending moment for unit load applied to pin. 57
Figure 48. Contour plots for the three vehicular loading cases showing draft (*y* displacement) of the 15-bay (110 m) IRB. Deformation scale = 5x. 59
Figure 49. Draft (y-displacement) of the 15-bay (110 m) IRB for the three vehicular loading cases, i.e., no vehicles, risk crossing, and normal crossing. 60
Figure 50. Drag force distribution along the 110 m (15-bay) IRB over a range of current velocities for the no-vehicles scenario. 61

Figure 51. Drag force distribution along the 110 m (15-bay) IRB over a range of current velocities for the risk-crossing scenario. 61

Figure 52. Drag force distribution along the 110 m (15-bay) IRB over a range of current velocities for the normal-crossing scenario. 62

Figure 53. Total drag force on the 15-bay (110 m) IRB as a function of current velocity for the three vehicular loading cases. 63

Figure 54. Representative transverse displacement, δx, contour plots for the 15-bay (110 m) IRB for the three vehicular loading cases. Flow is in the +x direction. For each vehicular loading case shown, v =11 ft/s, and the deformation scale is 5x. 64

Figure 55. Transverse displacement, δx, due to a range of flow velocities along the length of the 15-bay IRB for the three vehicular loading cases. 65

Figure 56. Maximum transverse displacement, $\delta x.\max$, as a function of flow velocity for the 15 bay IRB. 66

Figure 57. Main coupling pin connector forces over a range of current velocities for the 110 m (15-bay) 'no vehicles' scenario. 68

Figure 58. Main coupling pin connector forces over a range of current velocities for the 110 m (15-bay) risk crossing scenario. 69

Figure 59. Main coupling pin connector forces over a range of current velocities for the 110 m (15-bay) normal crossing scenario. 70

Figure 60. Contour plots of von Mises stress in the aluminum structure over a range of current velocities for the 110 m (15-bay) no-vehicles crossing. The images on the left and right view the bridge from above and below, respectively. Flow is in the $+x$ direction. 72

Figure 61. Contour plots of von Mises stress in the aluminum structure over a range of current velocities for the 110 m (15-bay) risk crossing. The images on the left and right view the bridge from above and below, respectively. Flow is in the $+x$ direction. 73

Figure 62. Contour plots of von Mises stress in the aluminum structure over a range of current velocities for the 110 m (15-bay) normal crossing. The images on the left and right view the bridge from above and below, respectively. Flow is in the $+x$ direction. 74

Figure 63. Von Mises stress in the aluminum structure of the center bay for the 110 m (15-bay) 'no vehicles', $v = 11$ ft/s scenario. 75

Figure 64. Von Mises stress in the aluminum structure of the center bay for the 110 m (15-bay) risk crossing, $v = 9$ ft/s scenario. 76

Figure 65. Von Mises stress in the aluminum structure of the center bay for the 110 m (15-bay) normal crossing, $v = 9$ ft/s scenario. 76

Figure 66. (a) Isometric view with transparency and (b) isometric view from below showing von Mises stress in the most highly stressed main coupling (downstream connection 7) for the 110 m (15-bay) 'no vehicles', $v = 11$ ft/s scenario. 77

Figure 67. (a) Isometric view with transparency and (b) isometric view from below showing von Mises stress in the most highly stressed main coupling (downstream connection 7) for the 110 m (15-bay) risk crossing, $v = 9$ ft/s scenario. 78

Figure 68. (a) Isometric view with transparency and (b) isometric view from below showing von Mises stress in the most highly stressed main coupling (downstream connection 7) for the 110 m (15-bay) normal crossing, v = 9 ft/s scenario. 79

Figure 69. Contour plots for the three vehicular loading cases showing draft (*y*-displacement) of the 30-bay (210 m) IRB. Deformation scale = 5x. 81

Figure 70. Draft (*y*-displacement) of the 30-bay (210 m) IRB for the three vehicular loading cases (no-vehicles, risk-crossing, and normal-crossing) 81

Figure 71. Drag force distribution along the 210 m (30-bay) IRB over a range of current velocities for the no-vehicles scenario. 83

Figure 72. Drag force distribution along the 210 m (30-bay) IRB over a range of current velocities for the risk-crossing scenario. 83

Figure 73. Drag force distribution along the 210 m (30-bay) IRB over a range of current velocities for the normal-crossing scenario. 84

Figure 74. Total drag force on the 210 meter (30 bay) IRB as a function of current velocity for the three vehicular loading cases 85

Figure 75. Representative transverse displacement, δx, contour plots for the 210 m (30-bay) IRB for the three vehicular loading cases. Flow is in the +x direction. For each vehicular loading case shown, v =9 ft/s and the deformation scale is 5x 86

Figure 76. Transverse displacement, δx, due to a range of flow velocities along the length of the 30-bay IRB for the three vehicular loading cases. 87

Figure 77. Maximum transverse displacement, $\delta x.\,max$, as a function of flow velocity for the 30-bay IRB. 88

Figure 78. Main coupling pin connector forces over a range of current velocities for the 210 m (30-bay) crossing with no vehicles on the IRB. 90

Figure 79. Main coupling pin connector forces over a range of current velocities for the 210 m (30-bay) risk crossing, with one 72-ton vehicle on the center of the IRB. 91

Figure 80. Main coupling pin connector forces over a range of current velocities for the 210 m (30-bay) normal crossing with five 72-ton vehicles on the IRB. 92

Figure 81. Contour plots of von Mises stress in the aluminum structure over a range of current velocities for the 210 m (30-bay) no-vehicles crossing. The images on the left and right view the bridge from above and below, respectively. Flow is in the $+x$ direction. 94

Figure 82. Contour plots of von Mises stress in the aluminum structure over a range of current velocities for the 210 m (30-bay) risk crossing. The images on the left and right view the bridge from above and below, respectively. Flow is in the $+x$ direction. 95

Figure 83. Contour plots of von Mises stress in the aluminum structure over a range of current velocities for the 210 m (30-bay) normal crossing. The images on the left and right view the bridge from above and below, respectively. Flow is in the $+x$ direction. 96

Figure 84. Von Mises stress in the aluminum structure of the most highly stressed bay (bay 16) for the 210 m (30-bay) no-vehicles, $v = 7$ ft/s scenario. 97

Figure 85. Von Mises stress in the aluminum structure of the most highly stressed bay (bay 16) for the 210 m (30-bay) risk crossing, v = 7 ft/s scenario. 98
Figure 86. Von Mises stress in the aluminum structure of the most highly stressed bay (bay 16) for the 210 m (30-bay) normal crossing, v = 5 ft/s scenario. 98
Figure 87. (a) Isometric view with transparency and (b) isometric view from below showing von Mises stress in the most highly stressed main coupling (downstream connection 15) for the 210 m (30-bay) no-vehicles, v = 11 ft/s scenario. 99
Figure 88. (a) Isometric view with transparency and (b) isometric view from below showing von Mises stress in the most highly stressed main coupling (downstream connection 15) for the 210 m (30-bay) risk-crossing, v = 9 ft/s scenario. 100
Figure 89. (a) Isometric view with transparency and (b) isometric view from below showing von Mises stress in the most highly stressed main coupling (downstream connection 15) for the 210 m (30 bay) normal-crossing, v = 9 ft/s scenario. 101

Tables

Table 1. Material properties for the IRB finite element model. 11
Table 2. IRB single-bay FEM properties. 16
Table 3. One-bay stress values converted from empirical strain data. 24
Table 4. Two-bay stress values converted from empirical strain data. 25
Table 5. Correlation summary for single-bay structural response tests. 32
Table 6. Correlation summary for dual-bay structural response tests. 38
Table 7. Correlation summary: average deviations for the entire structural response test series. 40
Table 8. Six-bay IRB raft push test series overview. 44
Table 9. Six-bay IRB raft simulations. 47
Table 10. Simulation matrix for the 110 m (15-bay) IRB crossings. 58
Table 11. Limit states for the 110 m (15-bay) IRB crossing types. 71
Table 12. Simulation matrix for the 210 m (30-bay) IRB crossings. 80
Table 13. Limit states for the 210 m (30-bay) IRB crossing types. 93
Table 14. Summary of IRB structural M&S analyses. 102
Table 15. Maximum water current speeds for no-vehicle, risk-crossing, and normal-crossing conditions. 102

Preface

This study was conducted for Product Manager, Bridging (PdM Bridging), MIPR 11326139, Project 464569.

This work was performed by the Structural Engineering Branch (GSS) of the Geosciences and Structures Division (GSD), US Army Engineer Research and Development Center, Geotechnical and Structures Laboratory (ERDC-GSL). At the time of publication of this report, Mrs. Mariely Mejias-Santiago was Chief, GSS; Mr. James L. Davis was Chief, GSD; and Mr. Nicholas Boone was the Technical Director for Force Projection and Maneuver Support. The Deputy Director of ERDC-GSL was Mr. Charles W. Ertle, II, and the Director was Mr. Bartley P. Durst.

COL Teresa A. Schlosser was the Commander of ERDC, and the Director was Dr. David W. Pittman.

1 Introduction

1.1 Background

The Improved Ribbon Bridge (IRB) is a modular, transportable, floating bridge system designed to give ground forces the capability to transport heavy military equipment over wet gaps, such as streams or rivers. A complete ribbon bridge crossing consists of a ramp bay at each bank and the required number of connected interior bays spanning between them. Each IRB interior bay is made up of two inner pontons that form a 14 ft 9 in. wide roadway and two outer pontons that provide 4 ft wide walkways on both sides of the roadway. The outer pontons also function like a ship bow, having a curved outer hull to reduce fluid drag.

The four pontons that make up an IRB bay are joined by hinges and pins along their adjacent edges that allow the bay to fold and unfold. Each IRB bay is transported, launched, and retrieved in a folded condition on a Common Bridge Transporter (CBT). Once launched, each bay unfolds automatically by the force of gravity and buoyancy generated as the bay is released and begins to float. The IRB bays are connected to each other by manually engaging integral lock-pins located at the end of each inner ponton. The lock-pins allow limited rotation between consecutively joined bays and provide for transfer of shear and force couples across connected bays.

The hydrodynamic forces, specifically current drag, acting on an IRB crossing, are typically resisted by use of Bridge Erection Boats (BEBs) or by cable anchorage systems. Current guidance on the use of BEBs and anchorage systems is conservative, and the underlying engineering requirements are not known. Also, the hydrodynamic and structural characteristics of the IRB are not well understood. To close this knowledge gap, the US Army Engineer Research and Development Center (ERDC) was tasked by US Army Product Manager Bridging to conduct an analytical study of IRB crossings for various flow rates and vehicular loading conditions.

1.2 Objective

This report documents the structural analysis of an IRB subjected to hydrodynamic and vehicular loading. The objective of this study was to establish engineering-based limit states for 110 m and 210 m IRB crossings based on hydrodynamic drag and vehicular loading.[1]

1.3 Approach

Measurements of as-built IRB bays were used to construct a three-dimensional, computer-aided design (CAD) model. The CAD model was then used to create a computational finite element model (FEM) that was validated through correlations of simulation results and empirical data. Finally, the validated FEM was used to establish limit states (i.e., maximum current and vehicular loading conditions for 110 and 210 m IRB crossings).

The two crossing spans (110 and 210 m) were chosen for analysis on the basis that each Army multirole bridge company (MRBC) is authorized 30 IRB interior bays, providing up to 210 m of bridging (Department of the Army 2009). This is the significance of the 210 m crossing. To better understand how the crossing span influences IRB loading, a 15-bay (110 m) bridge crossing was chosen as a second analysis case.

This report documents the structural modeling and simulation (M&S) of an IRB subjected to hydrodynamic drag and vehicular loading performed by ERDC. Chapter 2 discusses the computational modeling methodology. Chapter 3 describes the procedure used to validate the computational model. Chapter 4 presents the final M&S results and limit states for the 110 m and 210 m IRB crossings subjected to combined forces generated by hydrodynamic and vehicular loadings. Finally, Chapter 5 summarizes and concludes the work.

1 For a full list of the spelled-out forms of the units of measure used in this document, please refer to US Government Publishing Office Style Manual, 31st ed. (Washington, DC: US Government Publishing Office, 2016), 248-52, https://www.govinfo.gov/content/pkg/GPO-STYLEMANUAL-2016/pdf/GPO-STYLEMANUAL-2016.pdf.

2 Computational Modeling Methodology

This chapter describes the approach used to develop the IRB structural model. Section 2.1 details the computer-aided design (CAD) modeling procedure. Section 2.2 focuses on the finite element model development process.

2.1 Structural Improved Ribbon Bridge (IRB) computer-aided design (CAD) model development

The IRB was designed and is manufactured by General Dynamics European Land Systems. Due to the proprietary nature of the IRB, no drawings or models were available from which a CAD model could be created. Therefore, physical measurements of several as-built IRB interior bays were used along with IRB technical manuals (Department of the Army 2003a,b) to construct a computer model of an IRB bay.

On 29 March 2017, ERDC received three IRB interior bays from Red River Army Depot (RRAD). Figure 1 is a photograph of one of the bays being unloaded at ERDC. One of the bays was subsequently unfolded, and initial measurements were taken to provide exterior geometry for scaled physical models. Figure 2 shows the unfolded bay being modeled at ERDC.

Figure 1. Unloading IRB bays at ERDC.

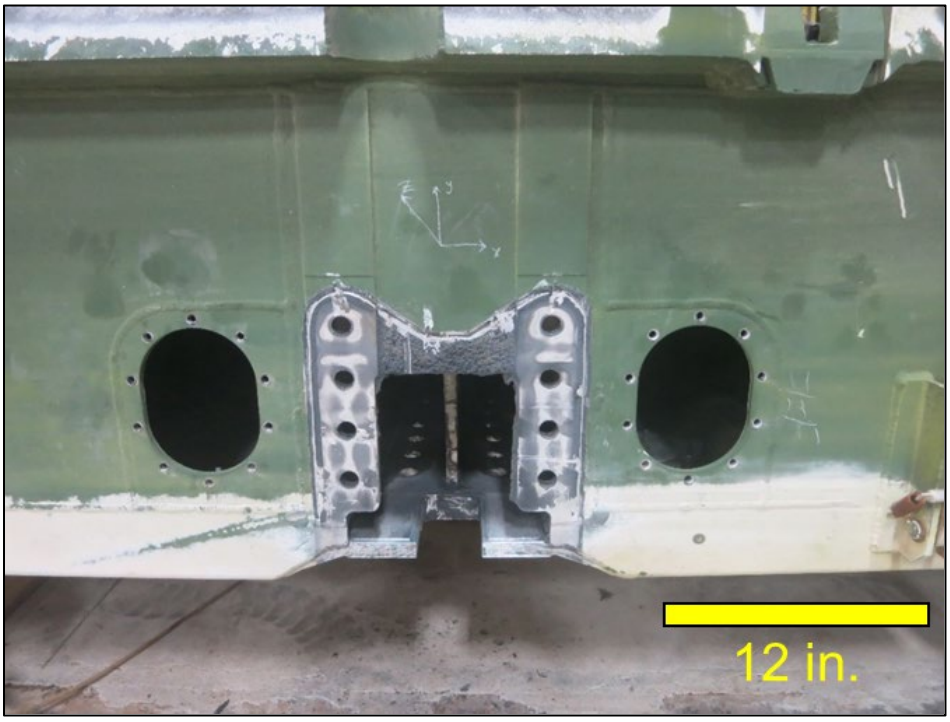


Figure 2. CAD modeling of an IRB interior bay at ERDC.



Minor dissection was also conducted at ERDC. Several parts that could be easily unbolted (e.g., the access hatches and lower main couplings) were disassembled from the bay for further study. Figure 3 shows the interior IRB bay with access panels and lower main coupling removed.

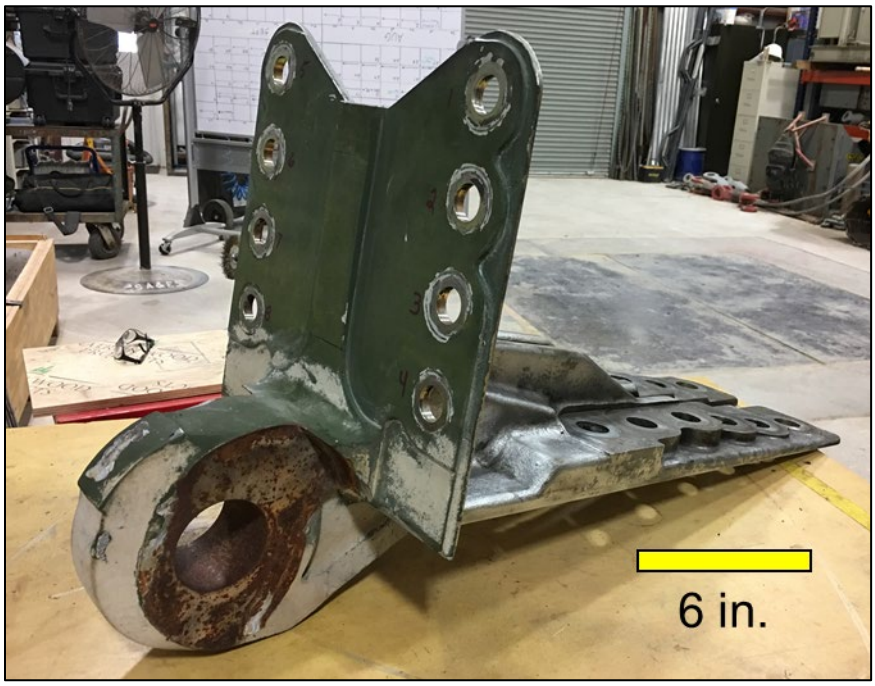
Figure 3. Interior IRB bay with access panels and lower main coupling removed.



The IRB main coupling that was removed for detailed modeling is shown in Figure 4. The main coupling is a steel casting and is bolted to the IRB with eight M24 bolts/nuts on the vertical flange and twelve M30

bolts/nuts on the bottom flange. Department of the Army (2003a) specifies installation torques of 443 lb-ft and 996 lb-ft for the M24 and M30 bolts, respectively. All of the hardware is grade 10.9 steel that has a minimum yield strength of 136 ksi. Hardness tests were performed on the main coupling to estimate the strength of the steel alloy.

Figure 4. IRB main coupling.



Removal of the access hatches and main coupling allowed limited inspection of the interior IRB structure. However, access to the interior structure was needed to facilitate measurements and provide confirmation of otherwise inaccessible geometry. To access the interior IRB structure, skin-plate removal was required. Since ERDC personnel had no previous experience in removal of the aluminum IRB skin, they reached out to the IRB maintenance facility at RRAD. Personnel at RRAD were helpful and accommodating, and a trip was arranged for ERDC personnel to travel to RRAD in April 2017. RRAD had several IRB bays on hand that were in need of repair and agreed to help ERDC dissect one of the bays.

Personnel at RRAD provided access to the internal structure of the inner and outer pontons by removing skin-plate sections (see Figure 5 and Figure 6). Through these *windows*, ERDC personnel could study and measure the interior details (see Figure 7 and Figure 8). RRAD personnel also cut into the deck of an inner ponton to reveal the inner structure of

the deck extrusions. As shown in Figure 9, the IRB deck is comprised of an extruded 6061-T6 aluminum profile with V-shaped stiffeners that run the length of the bay.

Figure 5. IRB inner ponton with skin-plate cutouts.



Figure 6. Outer ponton with skin-plate cutouts.



Figure 7. Interior of IRB bay at main coupling connection.

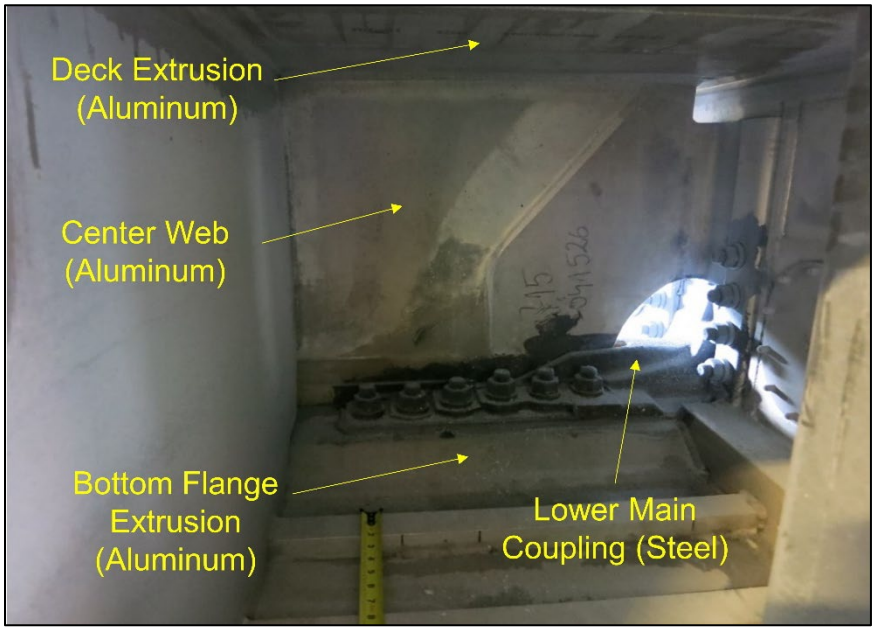
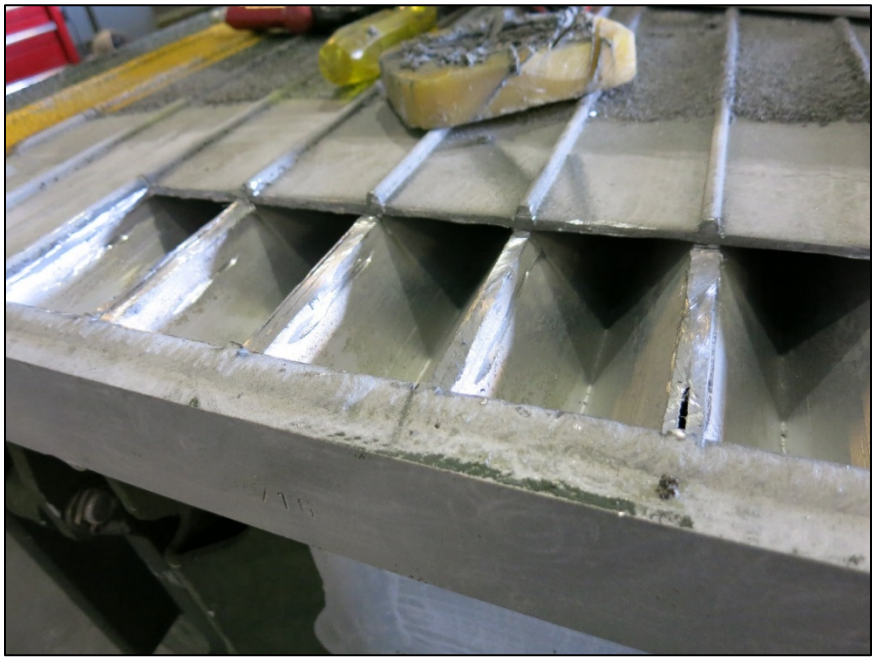


Figure 8. Ultrasonic thickness measurement of an interior stiffener.



Figure 9. Deck of interior ponton with top deck plate removed.



Once all of the primary structural elements of the IRB interior bay were measured and documented, the construction of the CAD model was addressed. Solidworks design software (Dassault Systémes 2016) was used to develop a three-dimensional (3D) CAD model of the IRB bay. Not every feature of the IRB bay was modeled in CAD. Every detail related to the pin and latch mechanisms that allow the bay to fold and unfold was not included; however, all of the structurally relevant parts were modeled appropriately. Figure 10 and Figure 11 show the completed IRB bay CAD model.

Figure 10. IRB interior bay CAD model showing interior details.

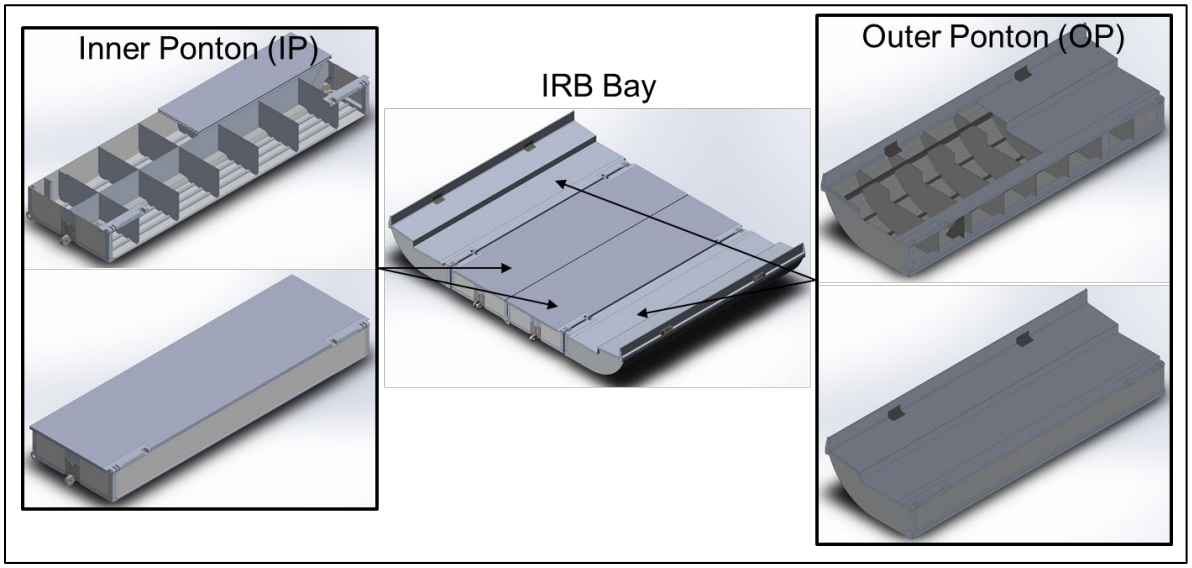
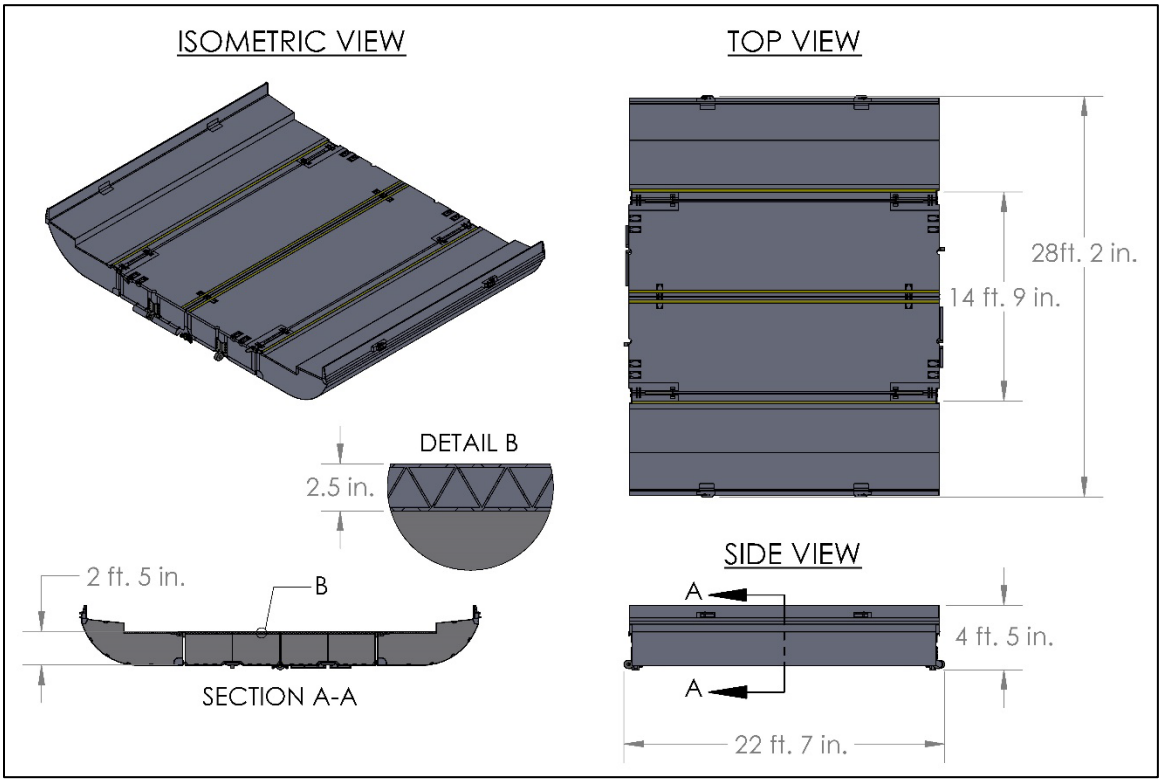


Figure 11. IRB interior bay CAD model overview with dimensions.



All the parts of the IRB are aluminum with the exception of a few of the main connections that are steel. All of the aluminum parts are joined by welded connections. The steel parts are connected to the aluminum structure by bolted connections. Structurally, the inner pontons are built somewhat like I-beams. The deck, which is a 2.5 in. thick aluminum

extrusion with integral V-shaped stiffeners, is analogous to one of the I-beam flanges. The bottom flange in the I-beam analogy is represented by another aluminum extrusion that runs the entire length of the bay and bolts to the main couplings on each end. Unlike the deck extrusions, the bottom flange is solid aluminum with a nominal thickness of 1.83 in. The center web has a nominal thickness of 3/8 in. with 3/4 in. thick reinforcements on each end where the steel lower main couplings are bolted. This connection was shown in Figure 7.

2.2 Structural IRB finite element model development

With the CAD model of the IRB bay complete, the next step was to import the CAD geometry into a finite element preprocessing software to build a mesh. Abaqus/CAE finite element modeling software (Dassult Systémes 2017) was used for this purpose. Since the IRB structure is primarily a weldment comprising relatively thin aluminum sheets, shell elements (type S4 and S3) were used throughout the majority of the model.

However, not all of the pieces could be modeled using shell elements because of their thicknesses. For the more complicated parts that did not conform to shell element theory, fully integrated quadratic, 10-node tetrahedral continuum elements (type C3D10) were used. Fully integrated quadratic 20-node hexahedral continuum elements (type C3D20) were also used on the parts with geometries simple enough to be meshed with bricks yet too thick to be modeled with shell elements.

First, a finite element mesh of the inner ponton was created, as shown in Figure 12. All but three components were meshed using shell elements, which were fully connected (i.e., nodes at joints were shared by adjacent elements). The upper hinge block, lower clevis, and main coupling were meshed with C3D10 elements. The bumper plate was meshed with C3D20 elements. All of the parts with the exception of the lower main coupling were assigned aluminum properties. The linear-elastic properties for steel and aluminum that were used in the analysis are given in Table 1.

Next, a finite element mesh for the outer ponton was created, as shown in Figure 13. The outer ponton is completely aluminum. The upper hinge blocks, where the outer ponton is connected to the inner ponton, and the bumper plate were the only parts requiring a continuum mesh. C3D10 elements were used to mesh the hinge blocks, and C3D20 elements were

used to mesh the bumper plate. The remaining structure comprises fully connected shell elements that share nodes along joints.

Table 1. Material properties for the IRB finite element model.

	Elastic Modulus, E (psi)	Poisson's Ratio, ν	Density, ρ (lb_m/in^3)
Aluminum	10,000,000	0.33	0.10
Steel	29,000,000	0.30	0.29

Figure 12. Inner ponton finite element mesh: (a) isometric view and (b) isometric view with deck removed to show interior structure.

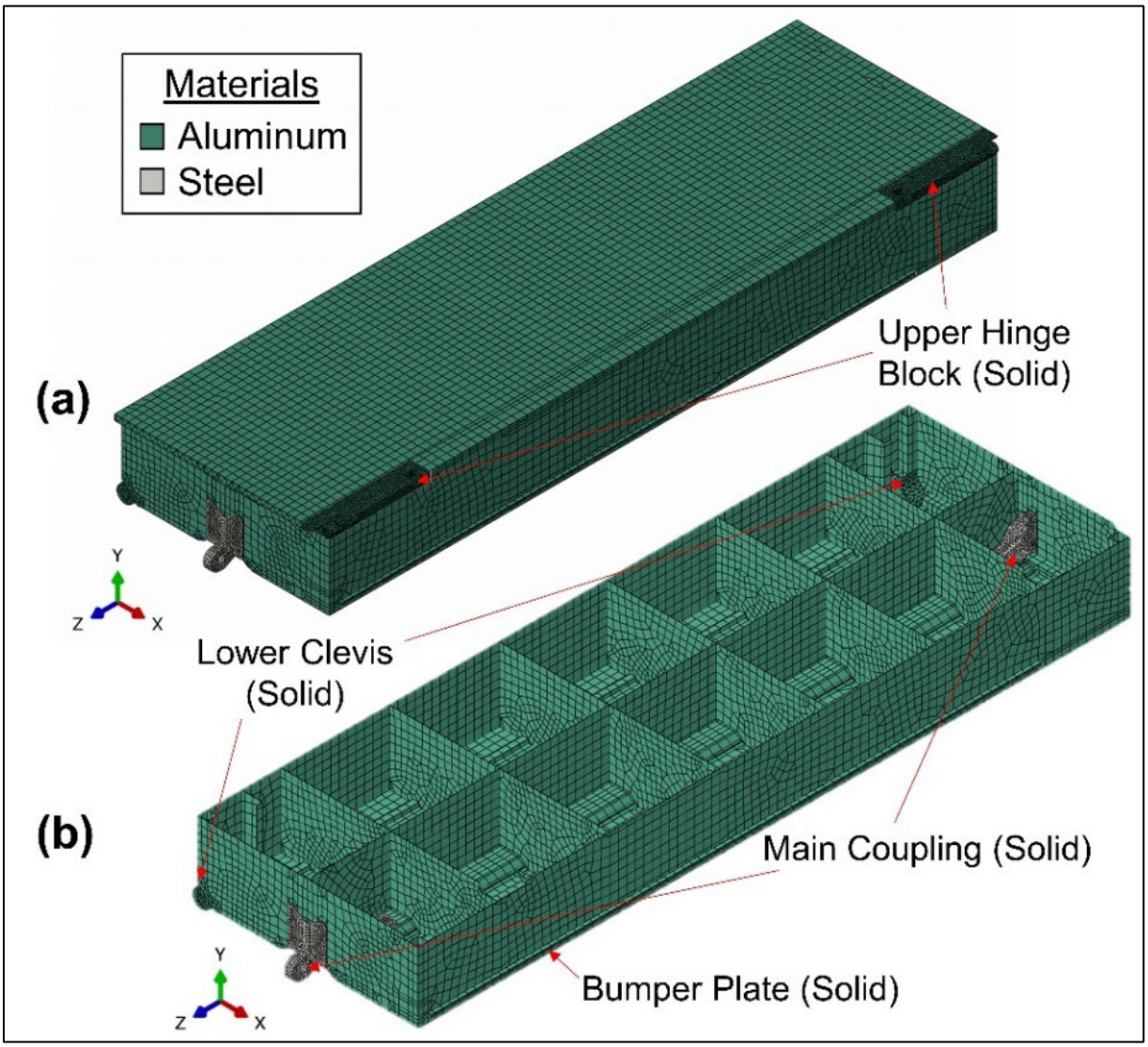
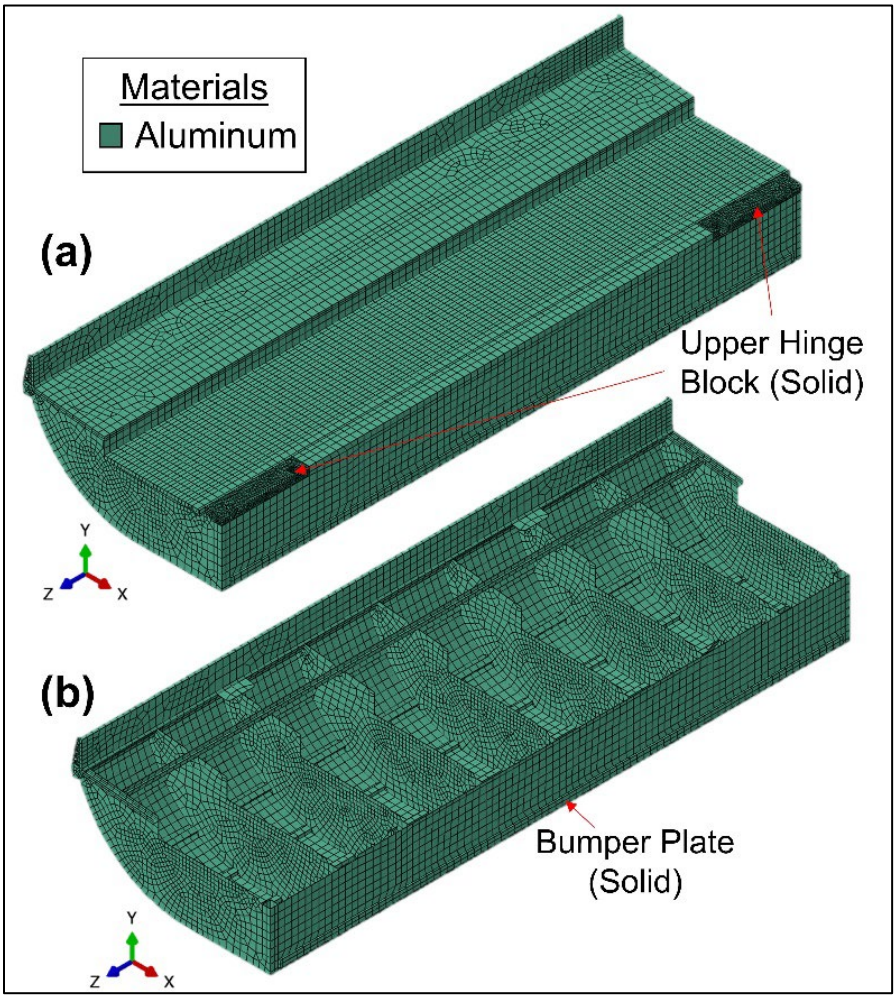
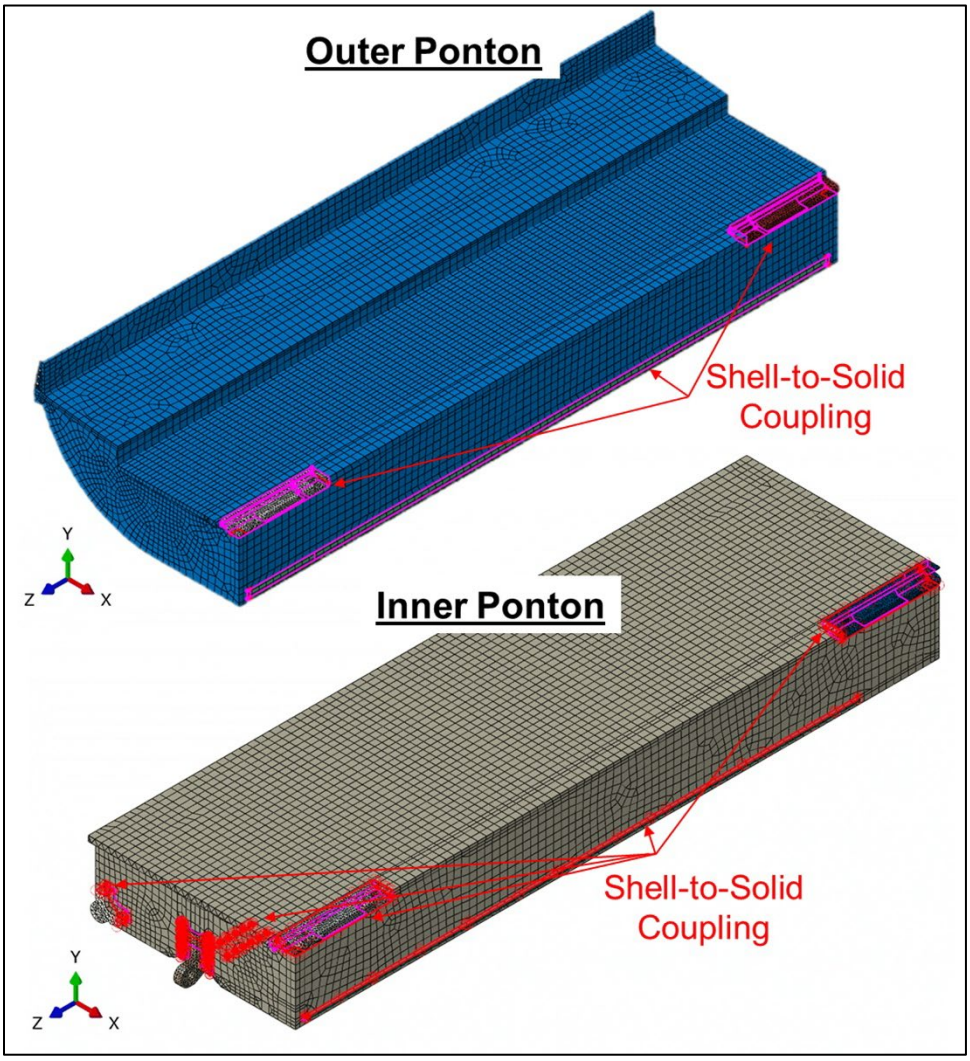


Figure 13. Outer ponton finite element mesh: (a) isometric view and (b) isometric view with deck removed to show interior structure.



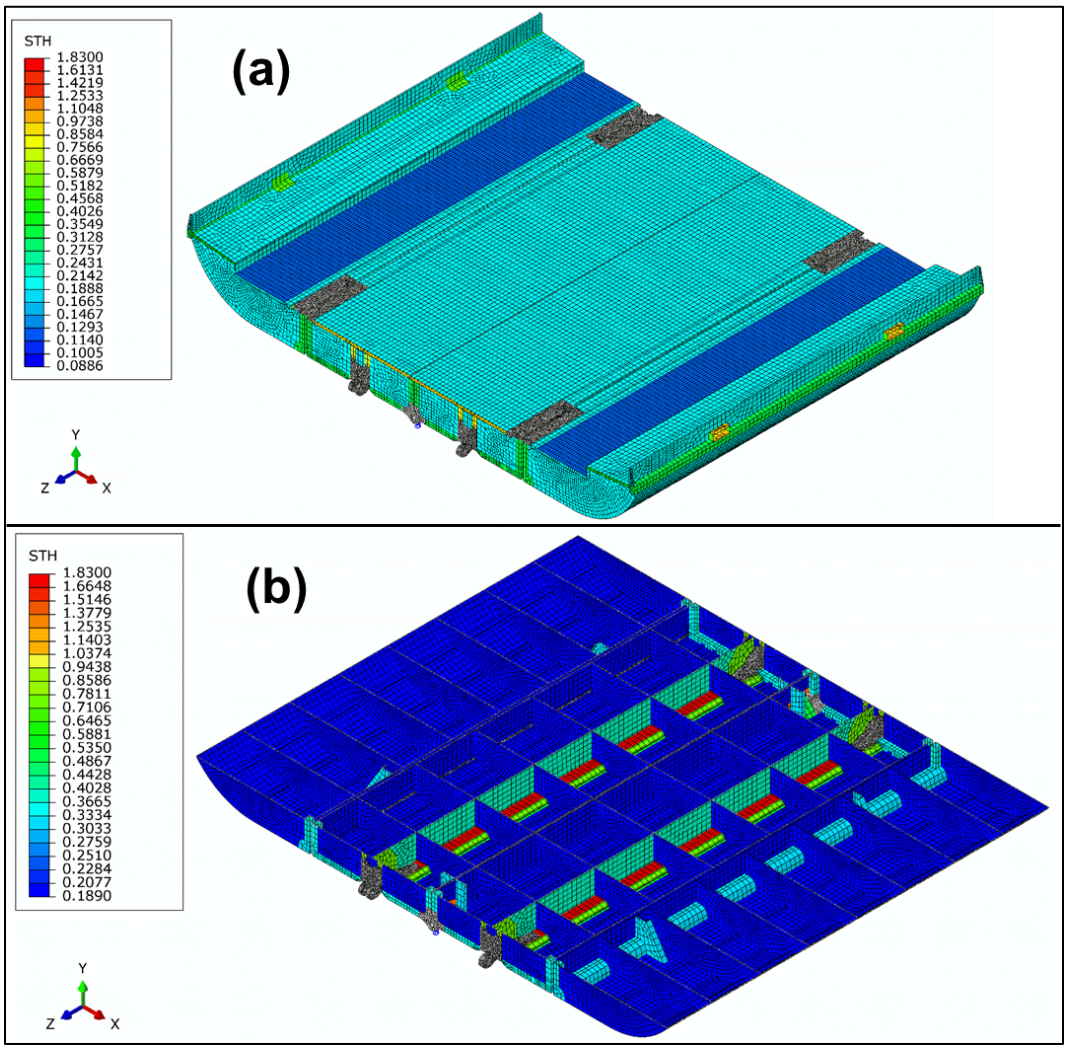
The parts meshed with solid continuum elements were connected to the rest of the shell structure by shell-to-solid couplings, as shown in Figure 14. In Abaqus, a shell-to-solid coupling uses a set of internally defined distributing coupling constraints to couple the motion of a *line* of nodes along the edge of a shell model to the motion of a set of nodes on a solid surface. At this point, the inner and outer ponton mesh subassemblies were fully connected.

Figure 14. Shell-to-solid couplings on the outer and inner ponton mesh subassemblies.



Two inner and two outer ponton mesh subassemblies were then joined to form a complete IRB mesh assembly. Figure 15 shows the complete IRB bay finite element mesh. Overlaid on the mesh is a contour plot showing shell element section thicknesses.

Figure 15. IRB single bay finite element mesh showing shell element section thicknesses: (a) isometric view and (b) isometric section view below the deck, showing interior structure. Units are inches.



The pins and hinges that connect the pontons were modeled using multi-point constraints (MPCs) (i.e., spider elements and special hinge connector elements (type CONN3D2) that allow rotation about a single axis). Figure 16 shows the spider element locations on the inner and outer ponton finite element models (FEMs). Figure 17 shows all of the connectors used to join the inner and outer pontons. MPC beam connectors were used to model the upper and lower locks that are engaged after the bay has been deployed. The inset in Figure 17 shows a close-up view of the hinge connection where the two inner pontons are joined. There are two of these hinge connections per bay. Once fully connected, the single bay IRB FEM was complete. The details of the single bay model are summarized in Table 2.

Figure 16. Multipoint constraint (spider element) locations on the inner and outer ponton FEMs.

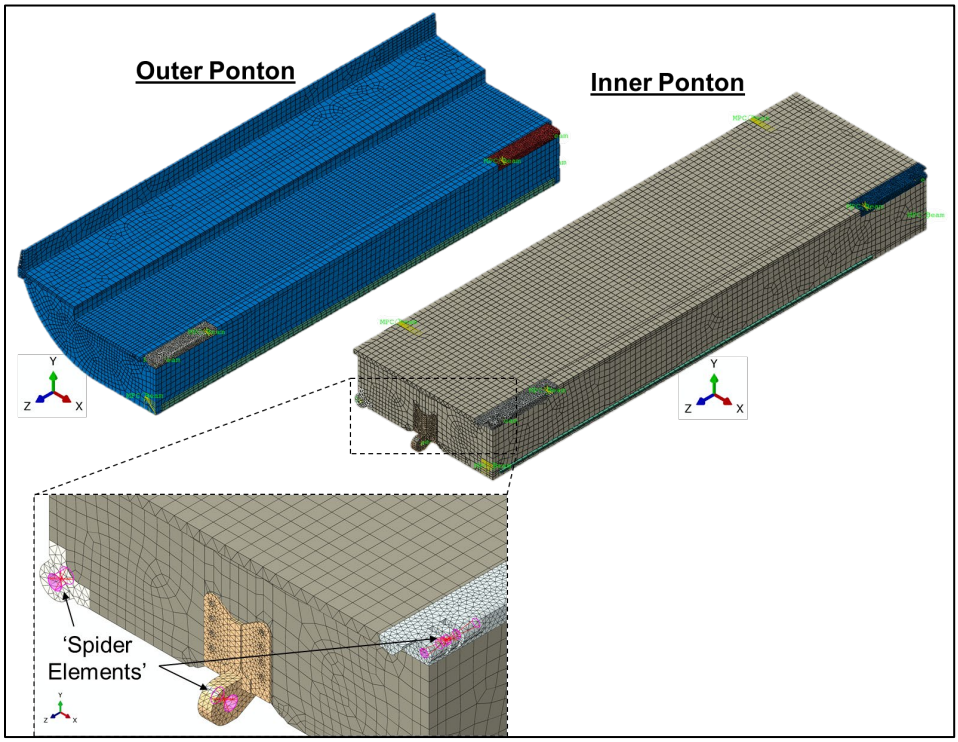


Figure 17. Inner ponton (IP) to outer ponton (OP) connectors.

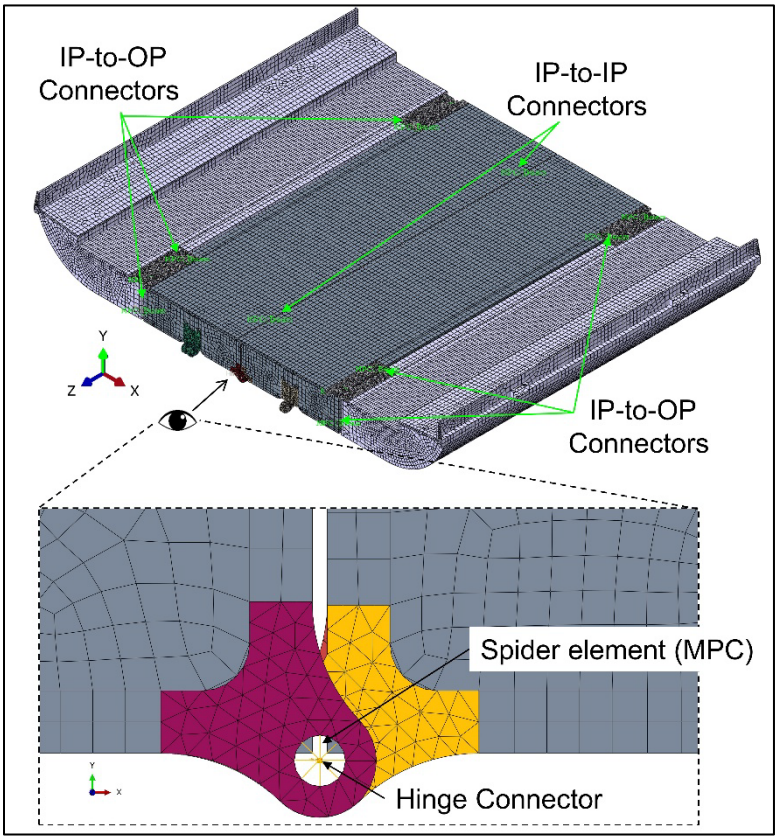


Table 2. IRB single-bay FEM properties.

No. of Elements	
Quadratic Tetrahedral Elements (Type: C3D10)	86,184
Quadratic Hexahedral Elements (Type: C3D20)	632
Linear Quadrilateral Elements (Type: S4)	95,356
Linear Triangular Elements (Type: S3)	1,938
Total No. of Elements	**184,110**
No. of Nodes	240,352
Characteristic Element Length (in.)	2.20
Total FEM Mass (lb_m)	14,002

The next step was to create multiple instances of the single-bay IRB assembly. Each IRB bay was connected at the main couplings using the same type of hinge connector elements that were previously used to connect the inner pontons. Contact surfaces were also defined at the end of each deck between adjacent bays. Figure 18 shows the interactions (contact surfaces and hinge connections) between adjacent IRB bays. When vehicular loads are placed on the bridge, the bays are free to rotate about the main coupling hinges. The decks of adjacent bays come into contact and compress against one another. This mechanism allows for vehicular loads to be distributed among multiple bays. A single IRB bay provides approximately 44 tons of buoyancy; however, when multiple bays are connected, their buoyancies are additive. This is due to the way the bays reinforce one another via deck contact between adjacent bays.

The method of copying and linking single IRB mesh assemblies could be used to create an IRB bridge of any desired length. Figure 19 illustrates this procedure. The 110 and 210 m crossings spans were of particular interest, which required 15 and 30 IRB bays, respectively.

Loads and boundary conditions for specific vehicle loads and fluid drag scenarios could then be applied to the now-complete IRB bridge meshes. The structural analysis of the 110 m and 210 m IRB bridges subjected to fluid drag and vehicular loading is presented in Chapter 4. However, to build confidence in the structural predictions from the IRB FEM, it must be first validated that the model gives accurate responses. Validation of the IRB FEM is the focus of Chapter 3.

Figure 18. Interactions between adjacent IRB bays.

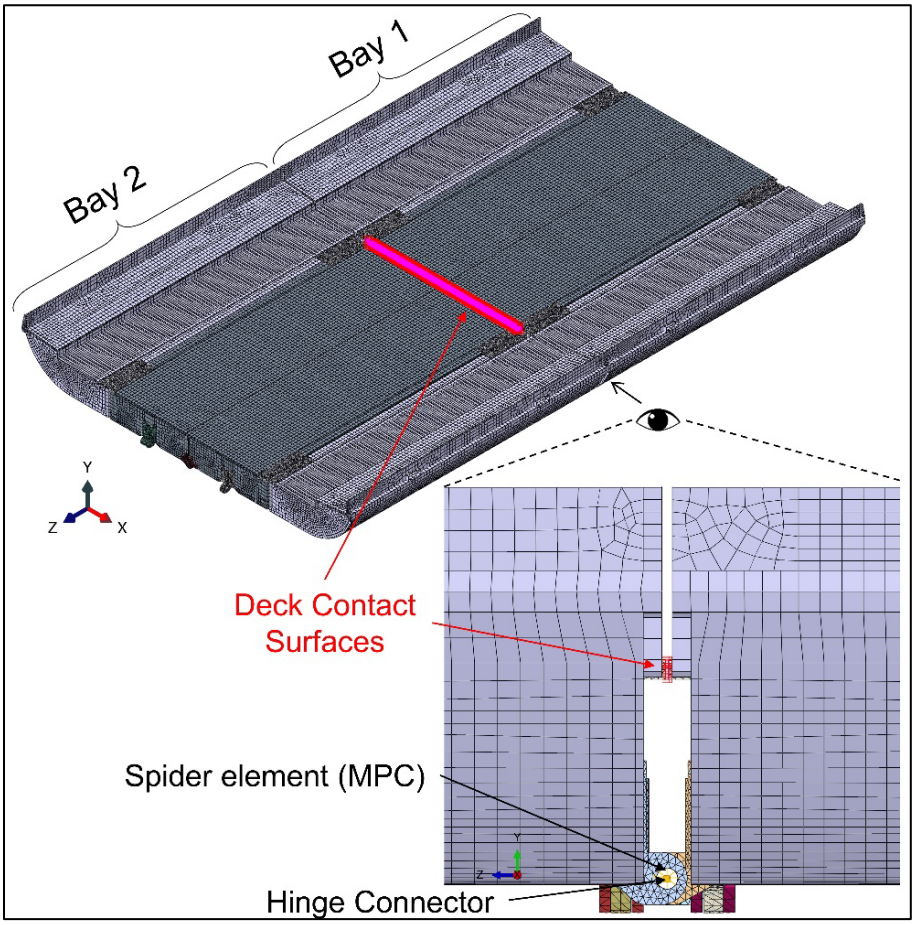
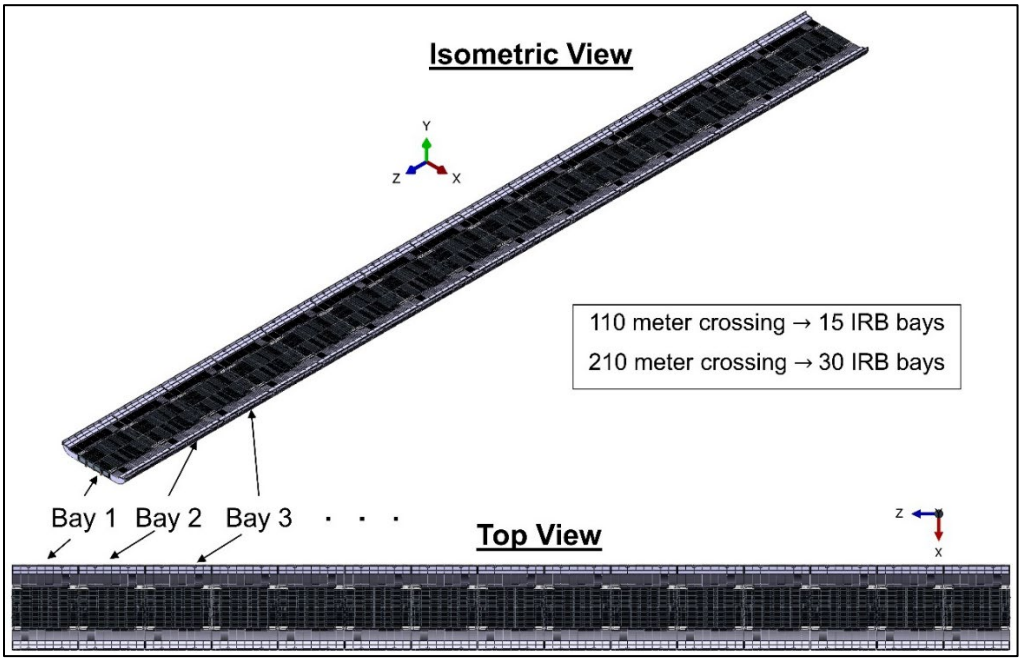


Figure 19. Complete IRB bridge mesh.



3 Structural IRB Finite Element Model (FEM) Validation

The FEM developed in Chapter 2 used physical measurements from as-built IRB bays because no previous models existed. As such, the model could have potentially undiagnosed issues. Before the IRB FEM could be used to make structural predictions, the model needed to be validated by comparing numerical solutions to experimental data.

Validation of the structural IRB finite element model was divided into two categories (i.e., structural response and fluid loading). Structural response validation was needed to ensure the computational model provides accurate structural responses (e.g., the FEM has the correct stiffness, mass distribution, connection properties). Also, the approach used to model the fluid loading required validation. The structural response and fluid loading validation studies are presented in Sections 3.1 and 3.2, respectively.

3.1 Structural response validation

To validate the accuracy of the structural response predictions of the IRB FEM, a test series was devised to generate empirical data that could be used to correlate against experimental data. The structural response validation methodology is provided in Section 3.1.1. Comparisons among experimental and simulated results for the structural response tests are presented Section 3.1.2. The structural response validation study results are summarized in Section 3.1.3.

3.1.1 Structural response validation methodology

A series of *floor* tests was conducted to generate experimental data that could be used to validate the linear elastic response of the IRB structural FEM. The full details of those tests are documented in Trim and Bennett (2018). A synopsis of the structural response physical testing is presented in Section 3.1.1.1. The methodology used to simulate the structural response tests is described in Section 3.1.1.2.

3.1.1.1 Structural response physical testing methodology

The structural response test series utilized two test configurations. In the first configuration, a single IRB bay (with outer pontons removed) was

supported at each end, and lead weights were placed on the deck, thereby loading the structure via gravity and producing longitudinal bending in the bridge section. The single-bay test configuration focused on generating data that can be used to verify the stiffness and structural response of the single-bay IRB FEM. In the second configuration, two IRB bays were linked together, supported, and loaded in a similar fashion as in the first configuration. The two-bay tests focus on generating data that can be used to verify that the interactions between the bays are modeled correctly. When loaded, the decks of the linked bays come into contact. This compressive contact is all that resists the hinged joints from rotating. Figure 20 shows a schematic of the one-bay and two-bay test configurations.

Figure 20. One-bay and two-bay test configurations in the structural response validation test series (Trim and Bennett 2018).

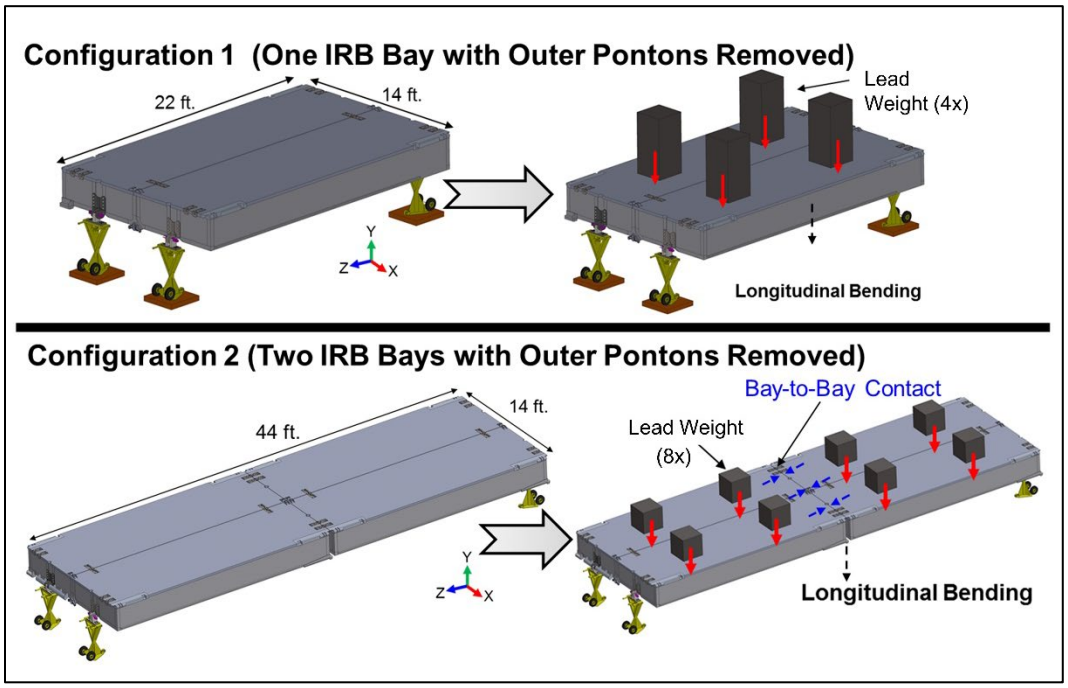


Figure 21 and Figure 22 show the actual arrangements for the one-bay and two-bay test configurations. Three individual tests were conducted on each of the two configurations by varying the amount of dead load placed on the deck. The load arrangements for the three single-bay tests (1-1, 1-2, and 1-3) are shown in Figure 23. The loading for the three dual-bay tests (2-1, 2-2, and 2-3) are presented in Figure 24.

Figure 21. Structural response validation test arrangement and instrumentation overview for the one-bay configuration (a) from above, (b) from below, and (c) from end (Trim and Bennett 2018).

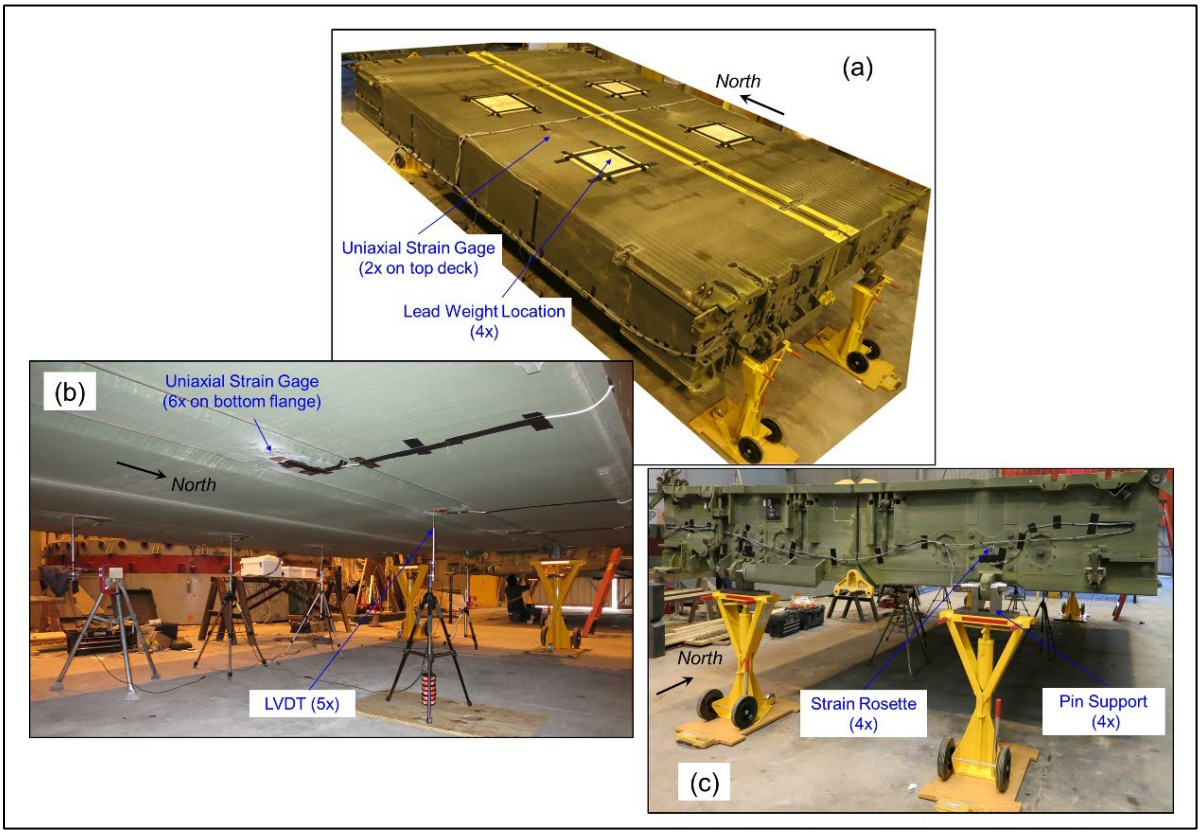


Figure 22. Structural response validation test arrangement and instrumentation overview for the two-bay configuration (a) from above, (b) from below, and (c) from end (Trim and Bennett 2018).

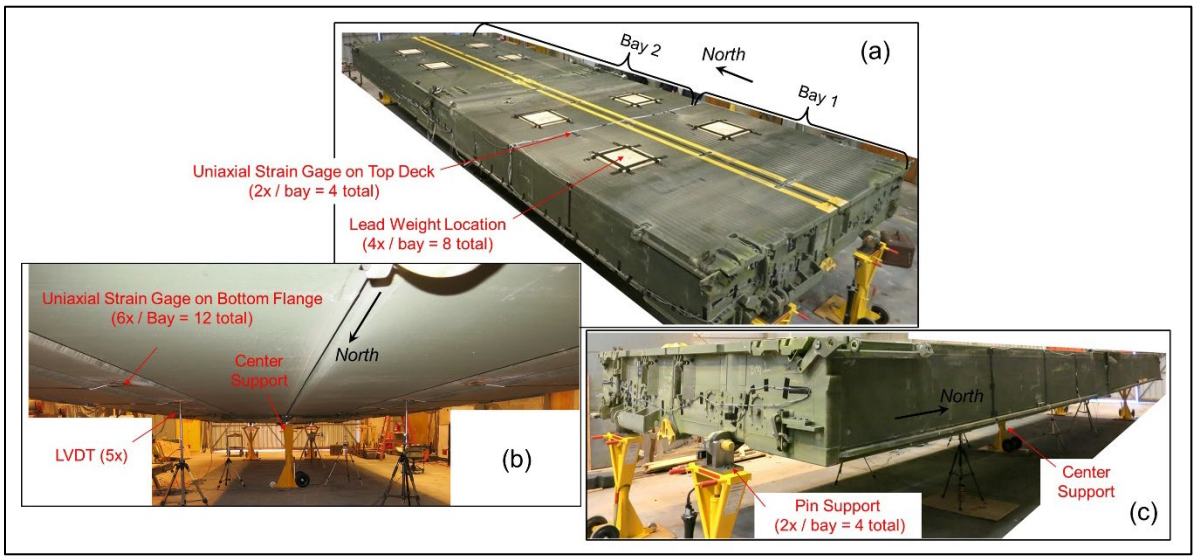


Figure 23. Load arrangements for one-bay structural response tests 1-1, 1-2, and 1-3 (Trim and Bennett (2018).

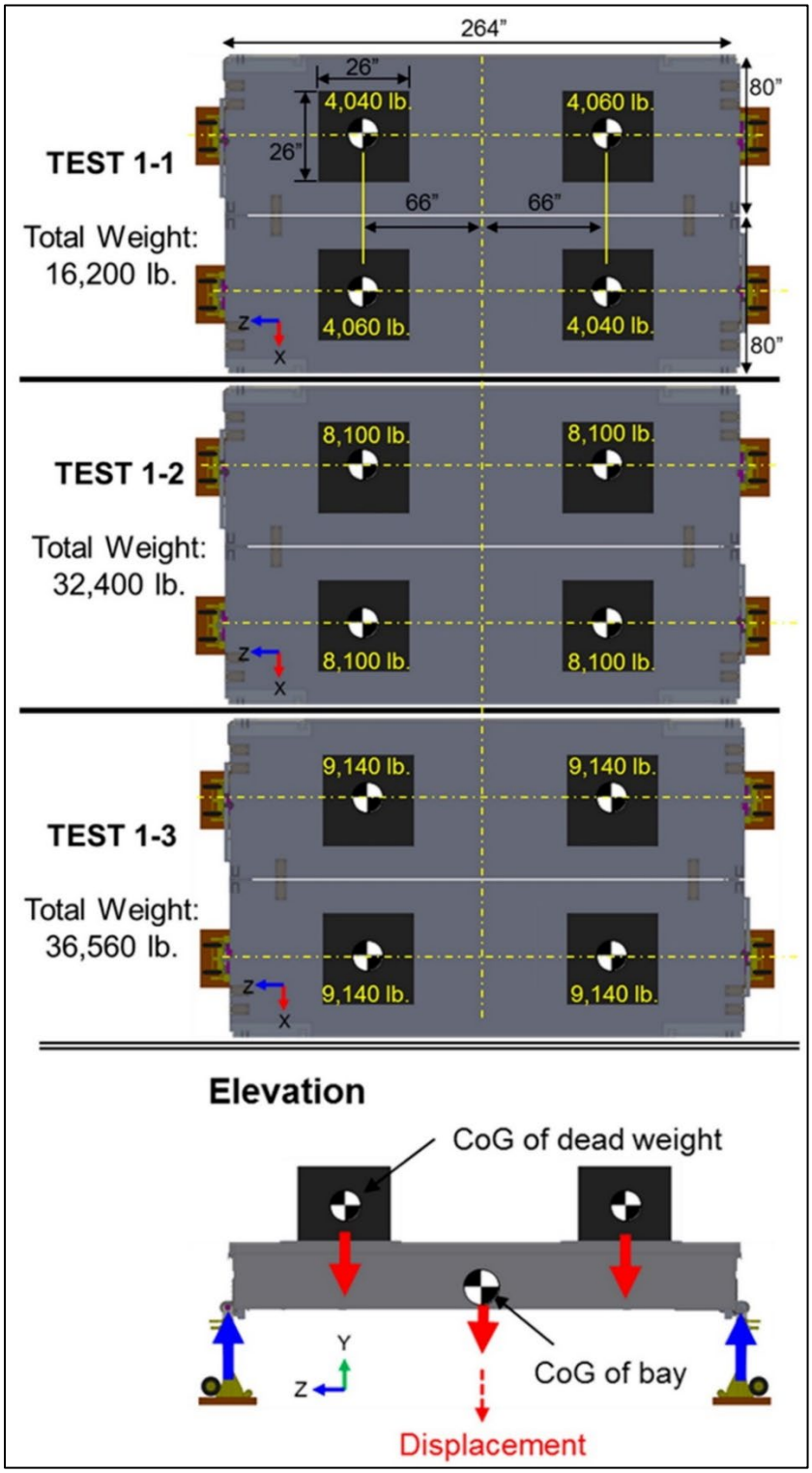
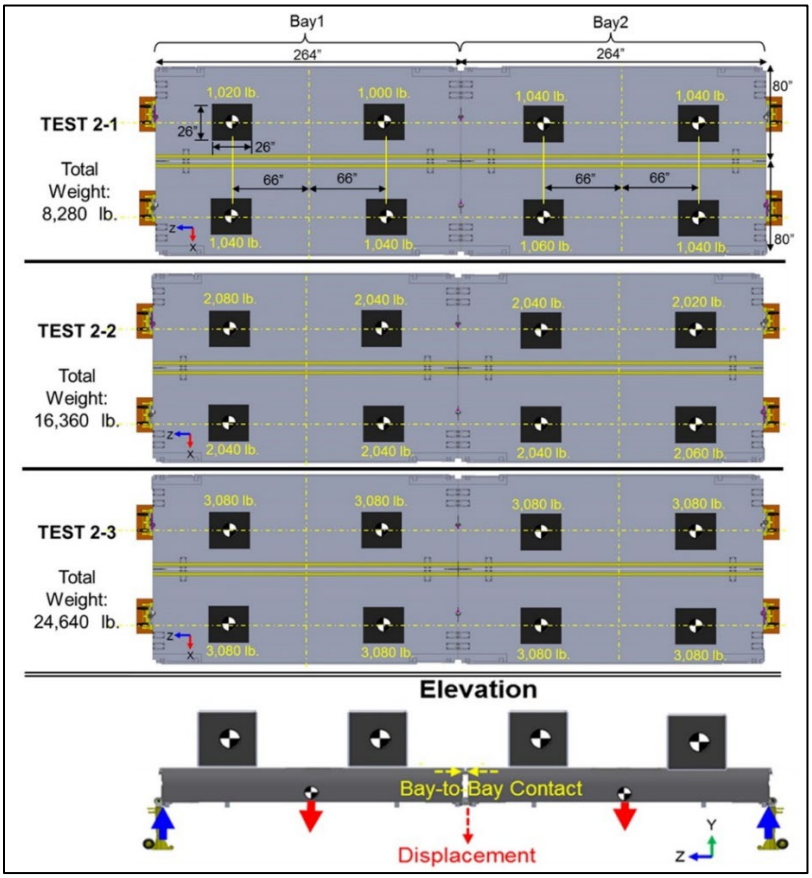


Figure 24. Load arrangements for two-bay structural response tests 2-1, 2-2, and 2-3 (Trim and Bennett 2018).



Instrumentation for the structural validation test was comprised of displacement transducers, load pins, weigh scales, uniaxial strain gauges, and strain gauge rosettes. For full instrumentation, details are in Trim and Bennett (2018). The load and displacement measurements could be directly compared to simulation output. However, to reduce the output file size for the simulations, only stress output was requested. To compare the physical strain data to simulation results, the strain measurements were converted to stress. The strain-to-stress conversion procedure is described in the following.

For the uniaxial gauges that were all placed on aluminum and oriented in the z direction, uniaxial strain (ε_{zz}) was converted to uniaxial stress (σ_{zz}) using Hooke's Law.

$$\sigma_{zz} = E_{Al}\varepsilon_{zz} \tag{1}$$

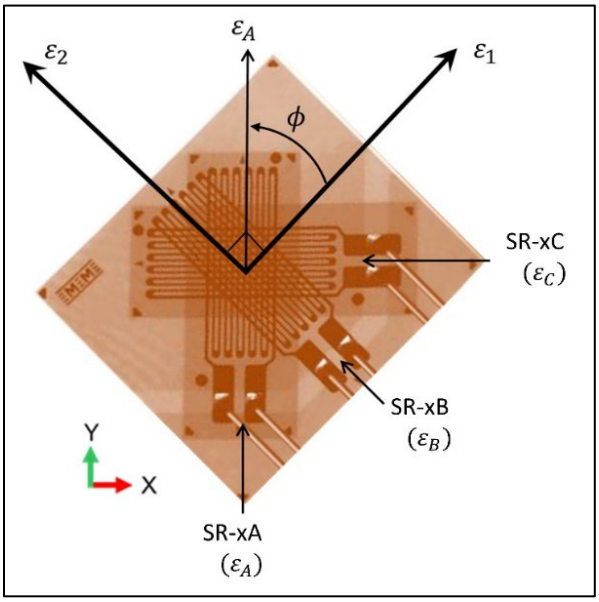
where E_{Al} = elastic modulus of aluminum, 1.0E7 psi.

Several strain gauge rosettes were also used. Each rosette was located on one of the steel IRB main couplings. A rosette comprises three independent, stacked, axial gauges positioned at 45° relative to each other. Rosettes allow calculation of the von Mises stress as follows.

The principal strains, $\varepsilon_{1,2}$, were calculated from the strains measured by the three grids of the rosette, $\varepsilon_{A,B,C}$, as shown in Figure 25, using

$$\varepsilon_{1,2} = \frac{\varepsilon_A+\varepsilon_C}{2} \pm \frac{1}{\sqrt{2}}\sqrt{(\varepsilon_A-\varepsilon_B)^2+(\varepsilon_B-\varepsilon_C)^2} \quad (2)$$

Figure 25. Schematic used for calculating principal stress/strain from rosette.



For linear elastic, homogeneous, isotropic steel, the principal stresses, $\sigma_{1,2}$, are related to the principal strains by

$$\sigma_1 = \frac{E_{St}}{(1-\nu_{St})^2}(\varepsilon_1 + \nu\varepsilon_2) \quad (3)$$

$$\sigma_2 = \frac{E_{St}}{(1-\nu_{St})^2}(\varepsilon_2 + \nu\varepsilon_1) \quad (4)$$

where

E_{St} = elastic modulus of steel, 2.9E7 psi
ν_{St} = Poisson's ratio for steel, 0.3.

Note that the mechanical property values for the steel and aluminum match those used in the IRB FEM (given in Table 2). Assuming plane stress, the von Mises stress, σ_{vm}, was calculated from the principal stresses for each rosette according to

$$\sigma_{vm} = \sqrt{{\sigma_1}^2 - \sigma_1\sigma_2 + {\sigma_2}^2} \quad (5)$$

Table 3 lists the converted stress values for the three single-bay tests, which were calculated from the measured strains from Table 3 of Trim and Bennett (2018). The converted stress values for the two-bay tests are given in Table 4, which were derived from the measured strains from Table 4 of Trim and Bennett (2018). The strain gauge locations for the gauges listed in Table 3 and 4 are identified in section 3.1.2.

Table 3. One-bay stress values converted from empirical strain data.

		Test 1-1	Test 1-2	Test 1-3
Added Weight (lb)		16,200	32,400	36,560
Gauge Type → Converted Stress	Gauge ID	Converted Stress (psi)		
Uniaxial Strain Gauges ↓ Uniaxial Stress, σ_{zz}	SAt-1 (E)	-349	-690	-791
	SAt-2 (W)	-367	-719	-828
	SAb-1 (E)	301	592	681
	SAb-2 (W)	134	252	236
	SAb-3 (S/W)	227	456	501
	SAb-4 (N/W)	251	512	565
	SAb-5 (S/E)	9	-18	-75
	SAb-6 (N/E)	161	284	260
Strain Gauge Rosettes ↓ von Mises Stress, σ_{vm}	SR-1 (S/W)	1588	-3314	3830
	SR-2 (S/E)	2305	-4686	5234
	SR-3 (N/W)	1879	-3911	4360
	SR-4 (N/E)	1574	-3331	3617

Table 4. Two-bay stress values converted from empirical strain data.

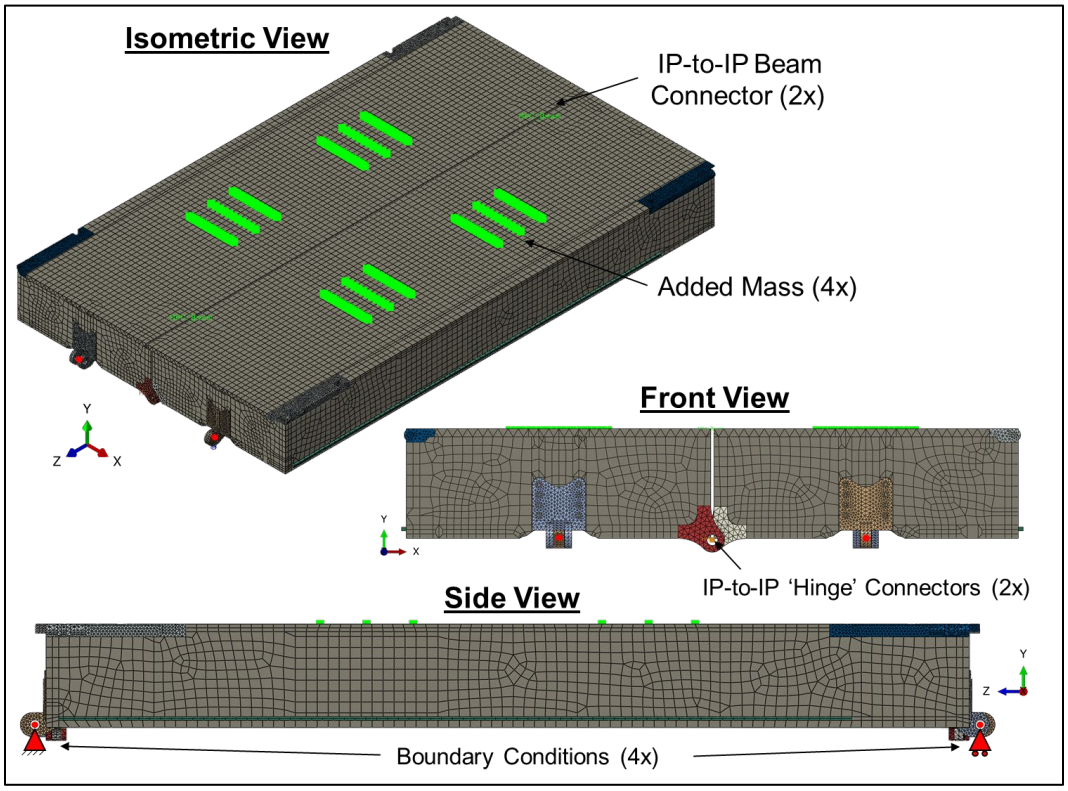
		Test 2-1	Test 2-2	Test 2-3
Added Weight (lb)		8,280	16,360	24,640
Gauge Type → Converted Stress	Gauge ID	Converted Stress (psi)		
Uniaxial Strain Gauges ↓ Uniaxial Stress, σ_{zz}	SA1t-1 (E)	-199	-396	-600
	SA1t-2 (W)	-207	-424	-637
	SA1b-1 (E)	190	387	561
	SA1b-2 (W)	158	318	464
	SA1b-3 (S/W)	145	296	423
	SA1b-4 (N/W)	236	467	681
	SA1b-5 (S/E)	89	168	245
	SA1b-6 (N/E)	198	390	568
	SA2t-1 (E)	-177	-372	-583
	SA2t-2 (W)	-171	-368	-581
	SA2b-1 (E)	145	281	427
	SA2b-2 (W)	172	333	488
	SA2b-3 (N/W)	116	223	321
	SA2b-4 (S/W)	191	364	542
	SA2b-5 (N/E)	143	283	410
	SA2b-6 (S/E)	235	475	702
Strain Gauge Rosettes ↓ von Mises Stress, σ_{vm}	SR1-1 (S/W)	786	1616	2396
	SR1-2 (S/E)	1091	2241	3354
	SR1-3 (W)	872	1791	2674
	SR1-4 (E)	802	1669	2551
	SR2-1 (N/W)	823	1613	2423
	SR2-2 (N/E)	700	1413	2111

3.1.1.2 Structural response simulation methodology

The construction of the IRB FEM was described in Section 2.2. Some minor modifications to the FEM model were necessary to condition the model such that it could be used to simulate the structural response tests. Specifically, the outer pontons and corresponding connections in the model had to be suppressed. Also, the areas on the deck where lead blocks were placed had to be defined.

The resulting single-bay structural response FEM is shown in Figure 26. Boundary conditions were applied at the four spider element reference nodes located in the center of each of the lower main couplings, thus mimicking the pin support from the floor tests. On one end, the nodes were pinned, which is necessary to constrain rigid body motion in the z direction. The prescribed boundary condition on the other end is similar to a simple roller support (i.e., only the x and y degrees of freedom were constrained). Distributed nonstructural mass was added at the locations shown in Figure 23. Three simulations were performed simulating tests 1-1, 1-2, and 1-3 by varying the magnitude of the nonstructural mass in accordance with Figure 23. For each simulation, an acceleration due to gravity, $g = 386.09$ in./s^2, was applied to the entire model in the negative y direction.

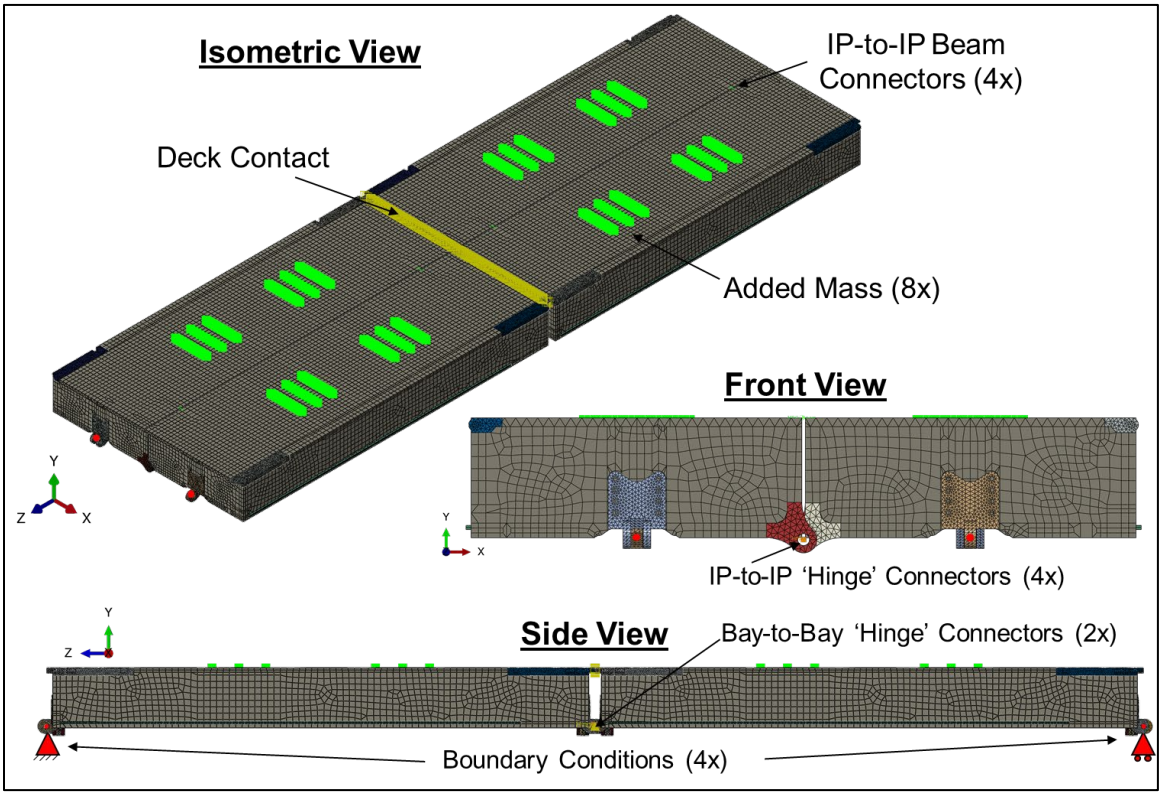
Figure 26. Single-bay structural response FEM.



To simulate the two-bay structural response tests, two IRB bay mesh assemblies were connected using interactions (as previously described in Section 2.2 and shown in Figure 18). As was done with the single-bay FEM, pin-and-roller type boundary conditions were used at the support locations, distributed nonstructural masses were added to represent the lead blocks, and gravity was applied in the negative y direction. Tests 2-1,

2-2, and 2-3 were simulated by varying the magnitude of the nonstructural masses in accordance with Figure 24. The two-bay structural response FEM is shown in Figure 27.

Figure 27. Two-bay structural response FEM.



3.1.2 Correlation between experimental and simulated test results

Comparisons among experimental measurements and simulation results for the single-bay structural response tests are presented in Section 3.1.2.1. Section 3.1.2.2 is devoted to correlation for the two-bay structural response tests. The simulation versus test correlation for the entire structural response test program is summarized in Section 3.1.3.

3.1.2.1 One-bay structural response correlation

Figure 28 is a test-versus-simulation comparison of reaction forces at the supports for the three single-bay structural response tests. For tests 1-1, 1-2, and 1-3, the reaction forces from the simulations were within 0.2% of the measured values. This indicates that the mass and mass distribution were accurately modeled.

Figure 28. Test-versus-simulation comparison of reaction forces at supports for single-bay structural response tests.

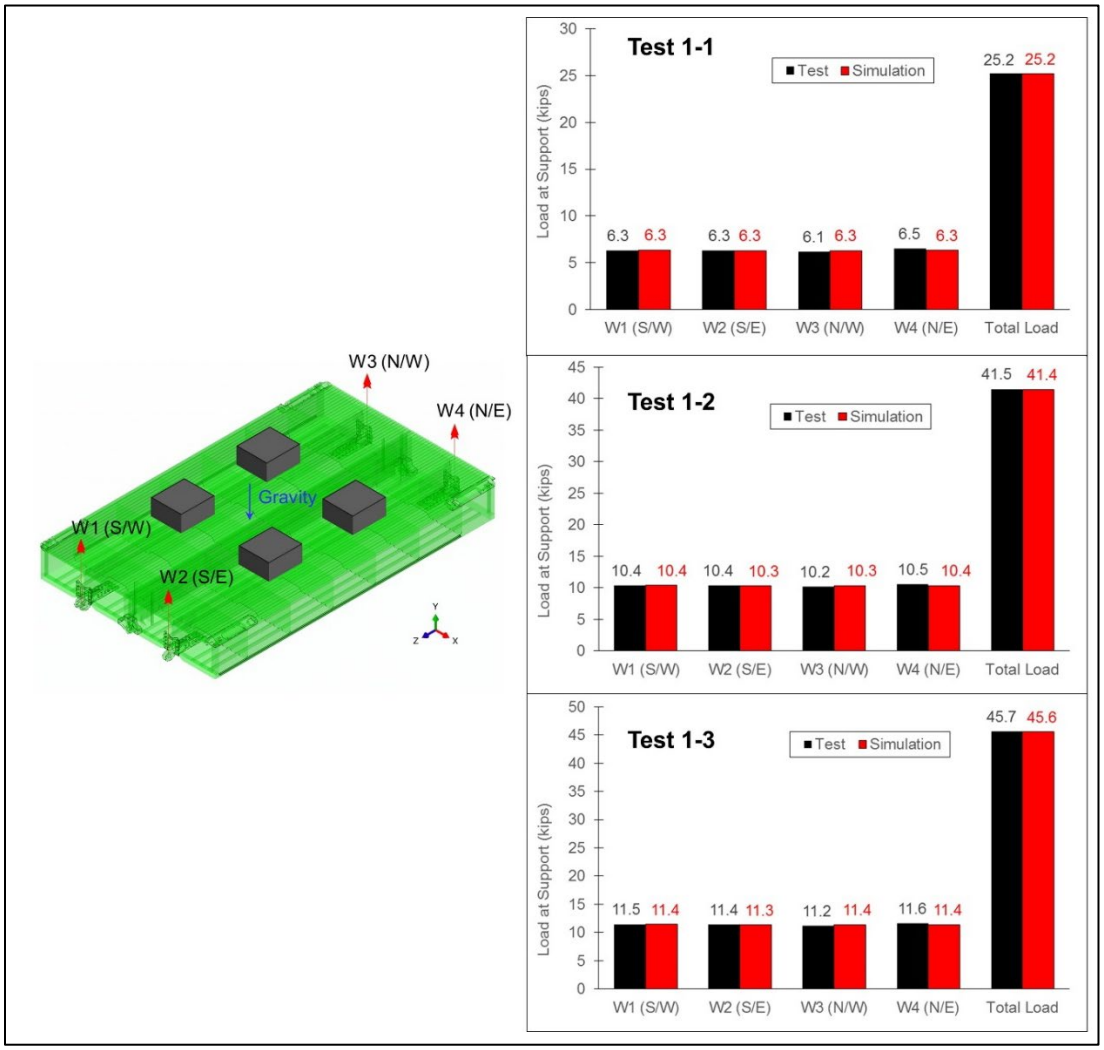


Figure 29 compares test-versus-simulation displacement measurements for the single-bay structural response tests. For test 1-1 with 16,200 lb of added mass, the deviation between test and simulation for the five displacement measurements averaged 6.7%. For test 1-2 where the added mass was doubled to 32,400 lb, the average displacement error decreased to just 1.4%. In addition, for test 1-3 (36,560 lb of added mass), the average displacement deviation between experiment and simulation was 5.7%. These results indicate that the single-bay IRB model has accurate stiffness and produces realistic linear elastic deflections under conditions representative of vehicular loading.

Figure 29. Test-versus-simulation comparison of displacement measurements for single-bay structural response tests.

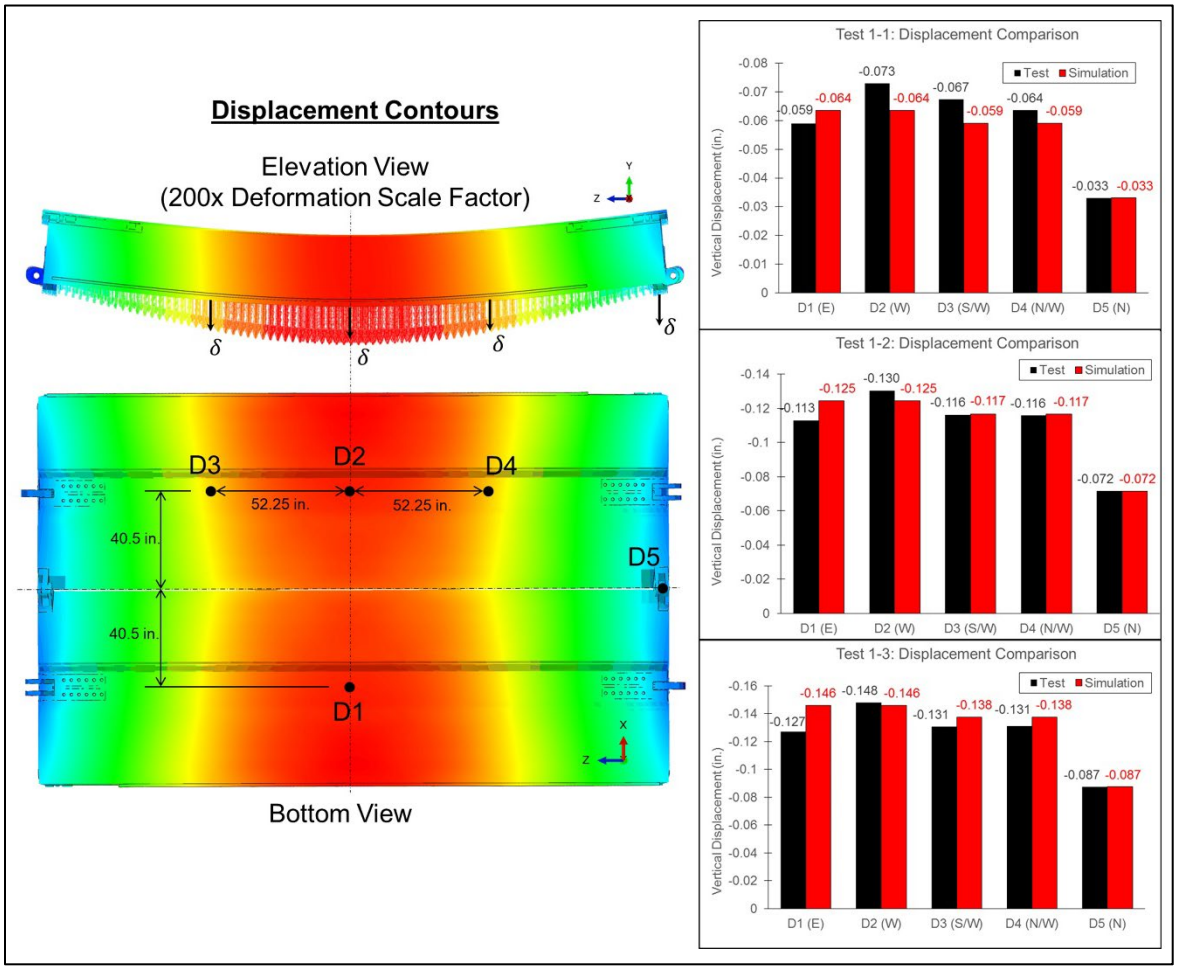
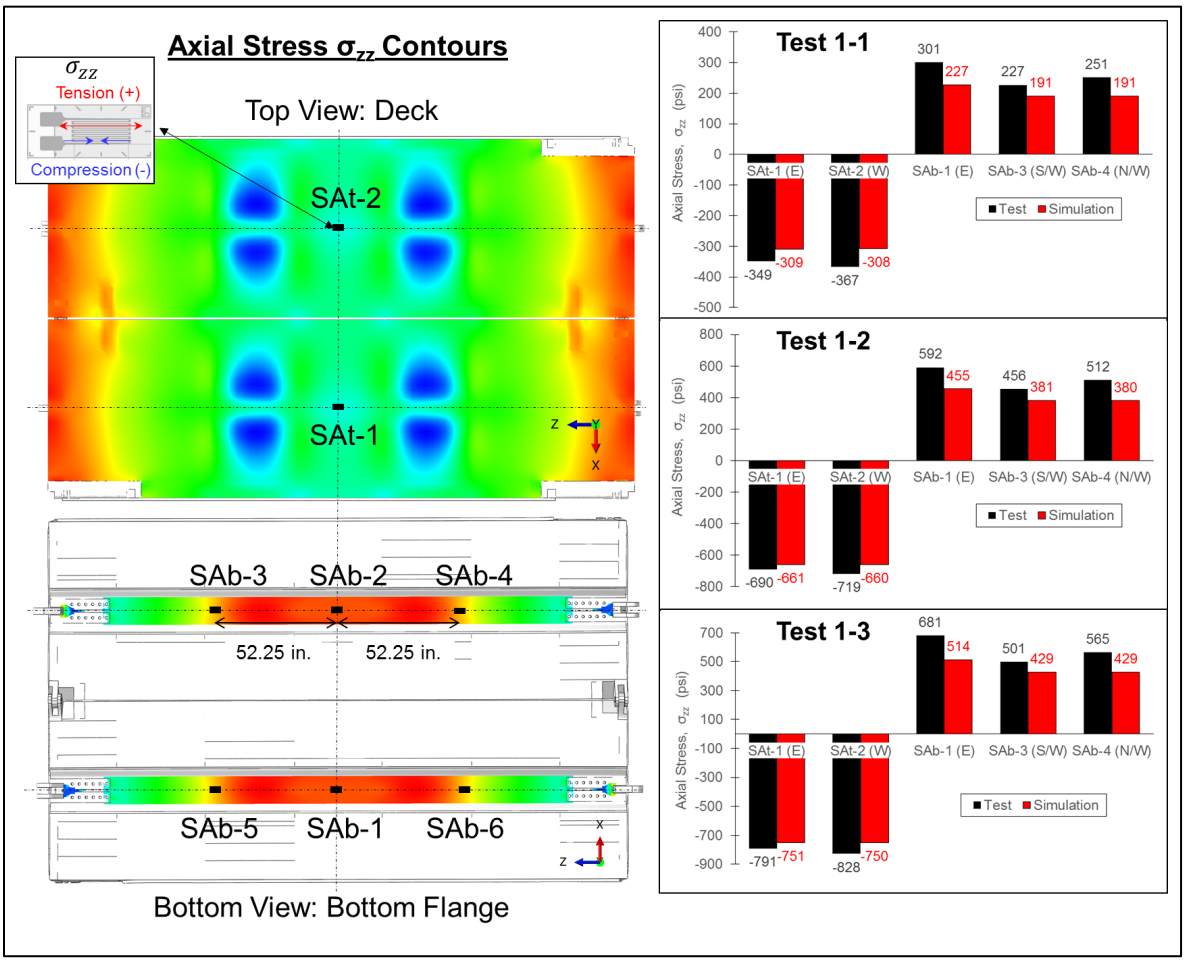


Figure 30 shows the single-bay test-versus-simulation comparison for axial stress, σ_{zz}, derived from the uniaxial strain measurements on the aluminum structure. As discussed in Trim and Bennett (2018), there were issues with the SAb-2, SAb-5, and SAb-6 strain gauges that made those measurement unreliable. Therefore, comparisons with those gauges were not made. Due to symmetry, it would be expected that SAt-1 = SAt-2, SAb-1 = SAb-2, and SAb-3 = SAb-4 = SAb-5 = SAb-6. The finite element analysis (FEA) stress predictions averaged 12% lower than the reliable measured values for all of the single-bay tests. Mesh refinement would undoubtedly reduce this error. However, the increase in computational expense for the large-scale, full-length bridge simulations would increase drastically. For the full-length bridge-length simulations (in Chapter 4), a correction factor is to be applied to ensure conservatism in the determination of limit states based on stresses in the aluminum structure.

Figure 30. Test-versus-simulation comparison of axial stress, σ_{zz}, measurements for single bay structural response tests.



The final comparison to be made for the single-bay structural validation test/simulation looks at the von Mises stress, σ_{vm}, on the flanges of the main couplings. Recall the von Mises stress was derived from the strain gauge rosette measurements. The test versus simulation σ_{vm} comparison is given in Figure 31. Due to symmetry, it is expected that the measurements at SR2 = SR3 and SR1 = SR4. The FEA stress predictions averaged 6.2% lower than the reliable measured values for all of the single-bay tests. Mesh refinement would likely reduce this error. For the full-length bridge-length simulations (in Chapter 4, a correction factor is to be applied to ensure conservatism in the determination of limit states based on stresses in the steel main couplings.

Figure 31. Test-versus-simulation comparison of von Mises stress, σ_{vm}, measurements for single-bay structural response tests.

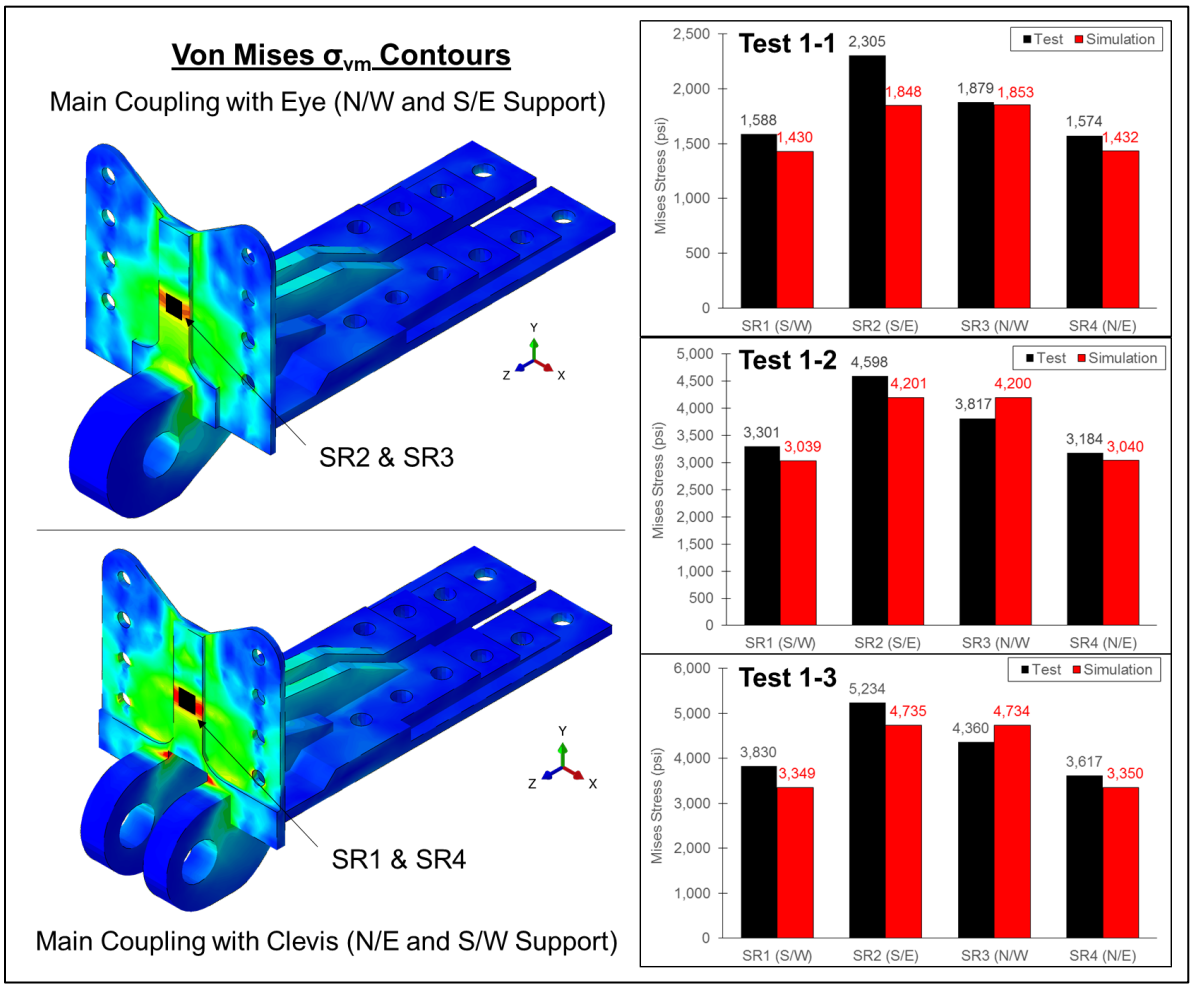


Table 5 summarizes the correlation between test and analysis for the three single-bay tests. The largest discrepancies occur in the aluminum bottom flange. For the single-bay tests, drift of varying degree was observed in some of the strain gauges at these locations. It is believed that this drift produced inflated readings at some of the gauges. These experimental inconsistencies, in combination with a relatively coarse mesh, produced maximum deviations of almost 25%. The simulations predicted lower stress magnitudes compared to the test data in each of the three single-bay tests. As noted in Trim and Bennett (2018), the faulty gauges on the aluminum were repaired prior to executing the dual bay tests, so those comparisons (in section 3.1.2.2) are perhaps more meaningful.

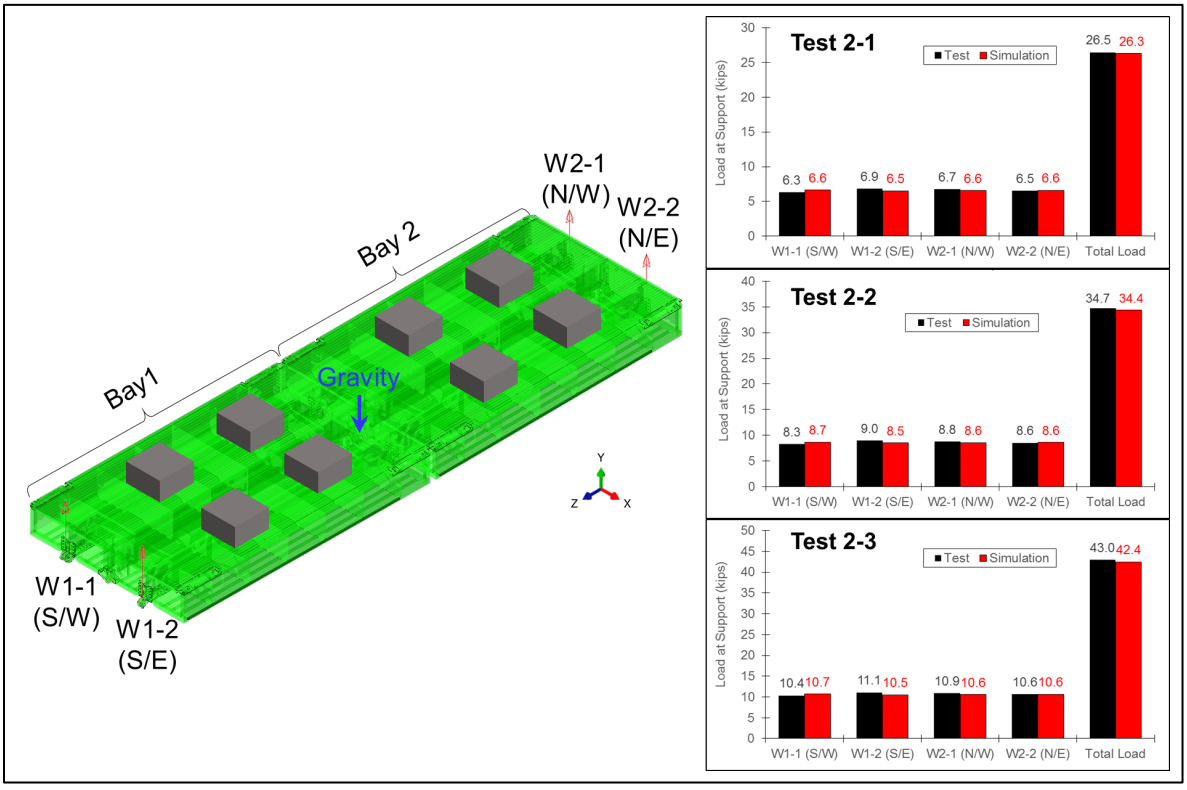
Table 5. Correlation summary for single-bay structural response tests.

Measurement Type / Comparable Location	ID	Test 1-1		Test 1-2		Test 1-3	
		Test	FEA	Test	FEA	Test	FEA
Uniaxial / Top, Center of Deck	SAt-1 (psi)	-349	-309	-690	-661	-791	-751
	SAt-2 (psi)	-367	-308	-719	-660	-828	-750
	Avg. (psi)	*-358*	*-309*	*-705*	*-661*	*-809*	*-751*
	% Dev.	**-13.8%**		**-6.3%**		**-7.3%**	
Uniaxial / Bottom, Center of Flange	SAb-1 (psi)	301	227	592	455	681	514
	% Dev.	**-24.6%**		**-23.1%**		**-24.5%**	
Uniaxial / Bottom, Qtr. Point of Flange	SAb-3 (psi)	227	191	456	381	501	429
	SAb-4 (psi)	251	191	512	380	565	429
	Avg. (psi)	*239*	*191*	*484*	*381*	*533*	*429*
	% Dev.	**-20.0%**		**-21.3%**		**-19.5%**	
Rosette / Main Coupling at Support	SR1 (psi)	1588	1430	3301	3039	3830	3349
	SR2 (psi)	2305	1848	4598	4201	5234	4735
	SR3 (psi)	1879	1853	3817	4200	4360	4734
	SR4 (psi)	1574	1432	3184	3040	3617	3350
	Avg. (psi)	*1837*	*1641*	*3725*	*3620*	*4260*	*4042*
	% Dev.	**-10.7%**		**-2.8%**		**-5.1%**	
Displacement / Bottom, Center of Flange	D1 (in.)	-0.0591	-0.0636	-0.1130	-0.1246	-0.1270	-0.1461
	D2 (in.)	-0.0729	-0.0636	-0.1305	-0.1246	-0.1478	-0.1461
	Avg. (in.)	*-0.0660*	*-0.0636*	*-0.1218*	*-0.1246*	*-0.1374*	*-0.1461*
	% Dev.	**-3.6%**		**2.3%**		**6.3%**	
Displacement / Bottom, Qtr. Point of Flange	D3 (in.)	-0.0674	-0.0591	-0.1163	-0.1167	-0.1306	-0.1376
	D4 (in.)	-0.0636	-0.0591	-0.1160	-0.1167	-0.1312	-0.1376
	Avg. (in.)	*-0.0655*	*-0.0591*	*-0.1162*	*-0.1167*	*-0.1309*	*-0.1376*
	% Dev.	**-9.8%**		**0.4%**		**5.1%**	
Reaction Force / at Support	W1 (lb_f)	6320	6331	10380	10403	11460	11449
	W2 (lb_f)	6300	6270	10380	10297	11380	11331
	W3 (lb_f)	6140	6295	10200	10340	11180	11378
	W4 (lb_f)	6480	6305	10540	10360	11640	11401
	Avg. (lb_f)	*6310*	*6300*	*10375*	*10350*	*11415*	*11390*
	% Dev.	**-0.2%**		**-0.2%**		**-0.2%**	

3.1.2.2 Two-bay structural response correlation

Figure 32 is a test-versus-simulation comparison of reaction forces at the supports for the three dual-bay structural response tests. For tests 2-1, 2-2, and 2-3, the reaction forces from the simulations were within 1% of the measured values. This indicates that the mass and mass distribution were accurately modeled.

Figure 32. Test-versus-simulation comparison of reaction forces at supports for dual-bay structural response tests.



The experimental and analytically determined connector forces in the two pins that join the IRB bays are compared in Figure 33. Based on symmetry, it is expected that P3Z and P4Z will be equal. The force measurements in the pins differed by an average of 3.2%, which gives an indication of the measurement precision. The deviations between test and simulation were approximately 5% based on the average force from the two pins.

Figure 33. Test-versus-simulation comparison of pin connector forces between bays for dual-bay structural response tests.

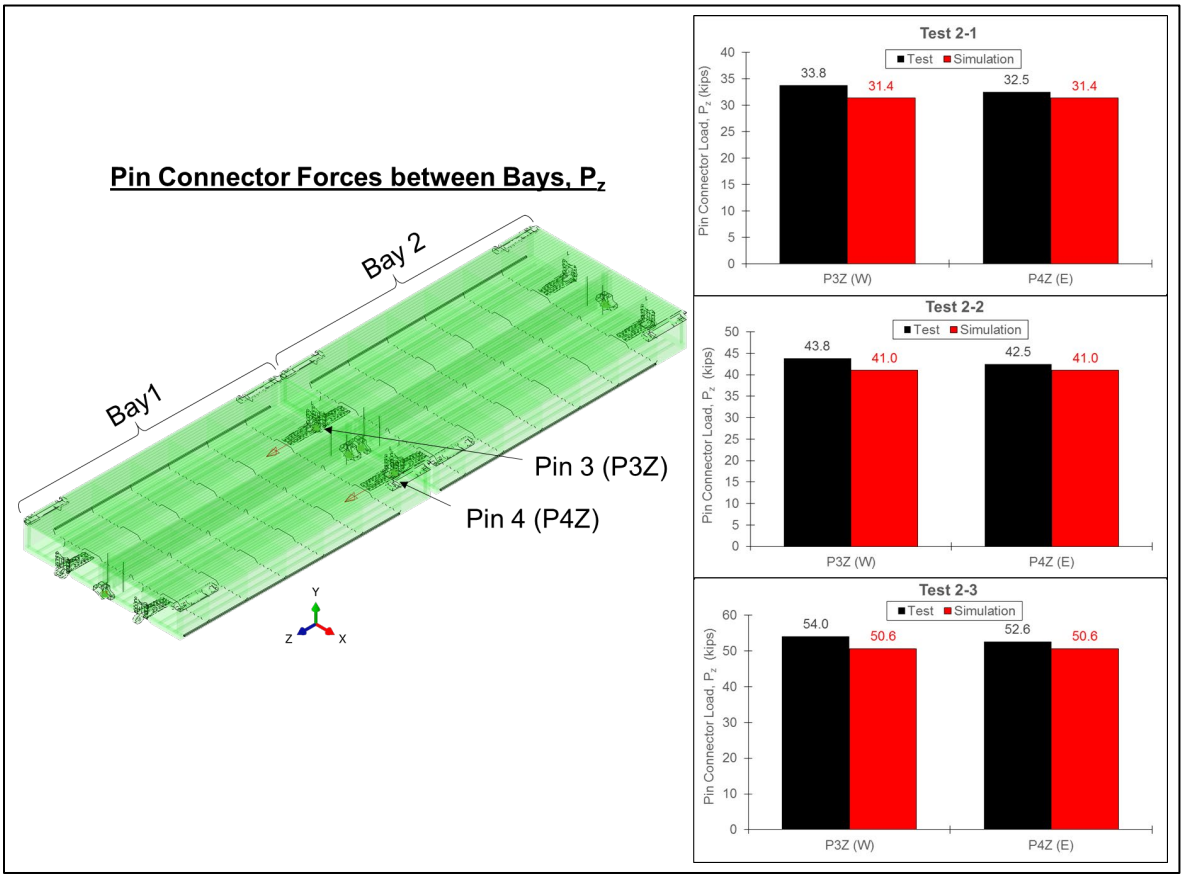


Figure 34 compares test-versus-simulation displacement measurements for the single-bay structural response tests. Due to symmetry, it is expected that D3 = D4 and D1-1 = D1-2 = D2-1. For test 2-1 with 8,280 lb of added mass, the deviation between test and simulation for the five displacement measurements averaged 3.2%. For test 2-2 where the added mass was increased to 16,360 lb, the average displacement error was 6.3%. Additionally, for test 2-3 (24,640 lb of added mass), the average displacement deviation between experiment and simulation was 8.3%. These correlations indicate that the physics of the bay-to-bay interactions are adequately captured in the IRB FEM.

Figure 34. Test-versus-simulation comparison of displacement measurements for dual-bay structural response tests.

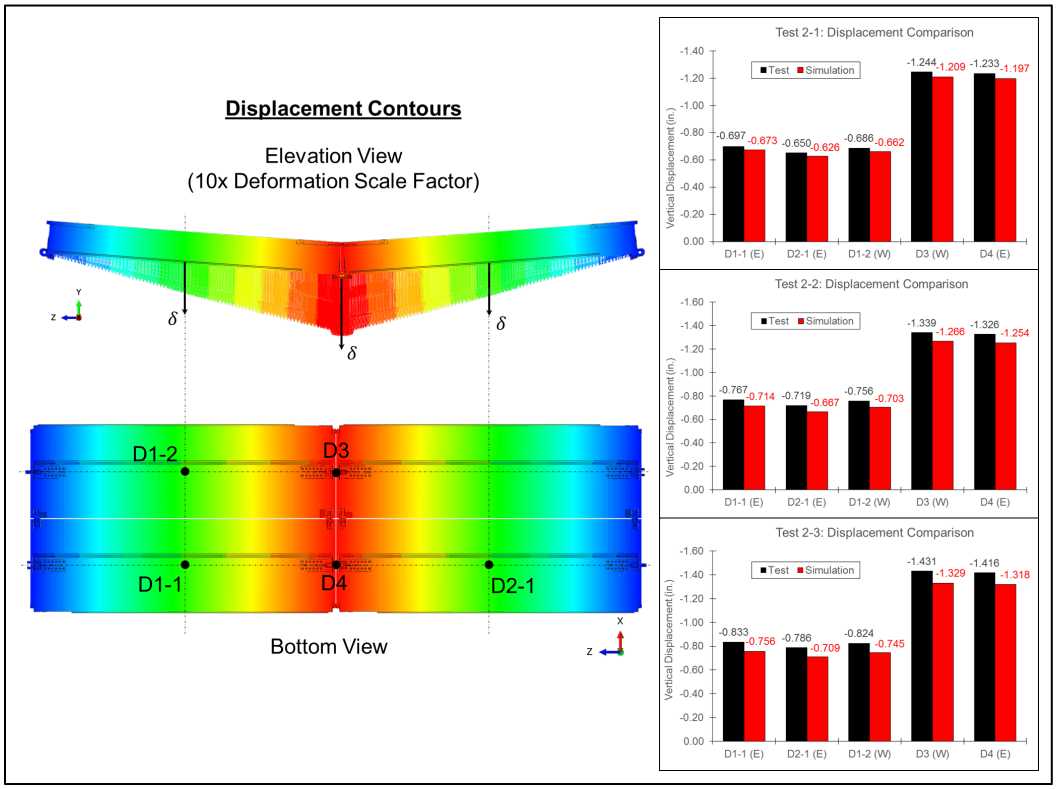
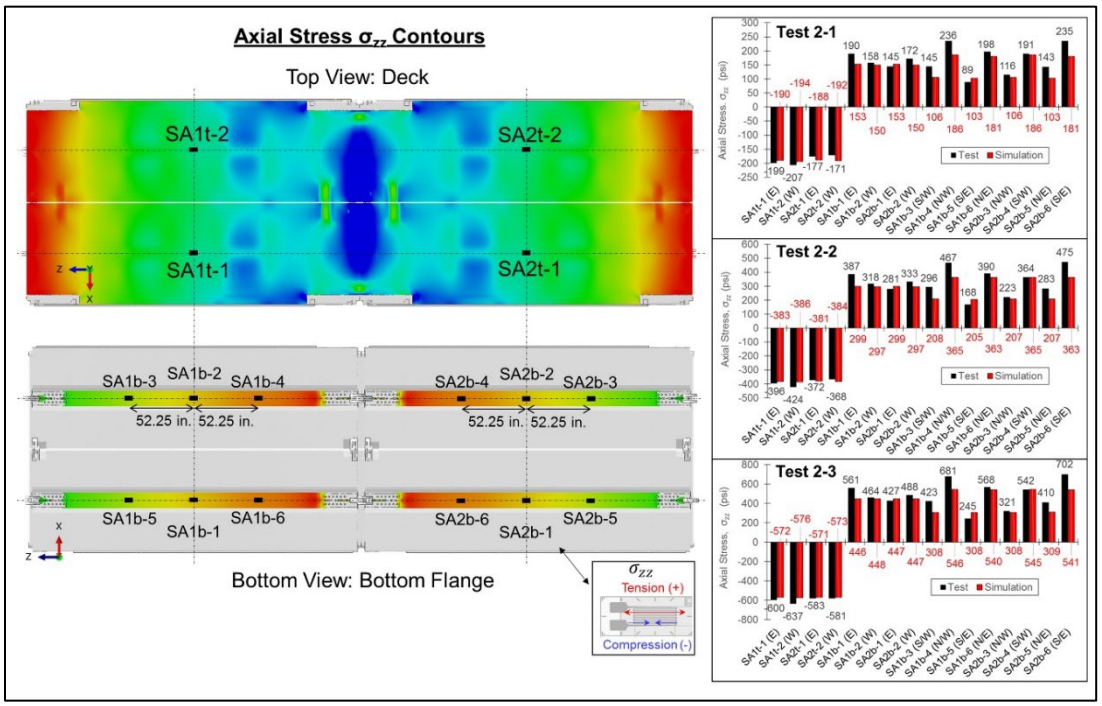


Figure 35 shows the single-bay test-versus-simulation comparison for axial stress, σ_{zz}, derived from the uniaxial strain measurements on the aluminum structure. Due to symmetry, it is expected that the gauges on the deck to be equal, i.e., SA1t-1 = SA1t-2 = SA2t-1 = SA2t-2. For test 2-1, the average stress measurement on the top deck was -188 psi. The corresponding simulation average was -191 psi. The redundant gauges on the bottom aluminum flanges are SA1b-1 = SA1b-2 = SA2b-1 = SA2b-2, SA1b-3 = SA1b-5 = SA2b-3 = SA2b-5, and SA1b-4 = SA1b-6 = SA2b-4 = SA2b-6. For the gauges centered on the bottom flange (SA1b-1, SA1b-2, SA2b-1, SA2b-2) stress measurements were between 145 psi and 190 psi for test 2-1. The corresponding FEA output at those locations was between 150 psi and 152 psi. For the bottom flange gauges near the supports (SA1b-3, SA1b-5, SA2b-3, SA2b-5), stress measurements were between 89 psi and 145 psi for test 2-1. Additionally, the corresponding simulation results were between 103 and 106 psi. For the bottom flange gauges near the joint (SA1b-4, SA1b-6, SA2b-4, SA2b-6), stress measurements ranged from 191 psi to 236 psi for test 2-1. The corresponding stress values from the simulation were between 181 and 184 psi. Similar comparisons for tests 2-2 and 2-3 reveal similar results.

Figure 35. Test-versus-simulation comparison of axial stress, σ_{zz}, measurements for dual-bay tests.



The final comparison to be made for the two-bay structural validation test/simulation looks at the von Mises stress, σ_{vm}, on the flanges of the main couplings, which was derived from the strain gauge rosette measurements. The test-versus-simulation σ_{vm} comparison is given in Figure 36. Due to symmetry, it is expected that the measurements at the couplings on opposite corners to be identical (i.e., SR1-1 = SR2-2 and SR1-2 = SR2-1). Looking at the couplings on opposite corners with clevises (SR1-1 and SR2-2), the average stress was 743 ± 43 psi for test 2-1. The simulation predicted σ_{vm} = 691 psi at that location. For the couplings on opposite corners with eye connectors (SR1-2 and SR2-1), the average stress was 957 ± 134 psi for test 2-1, where the corresponding simulation result was σ_{vm} = 741 psi. Looking at the measurements on the couplings at the bay-to-bay joint (SR1-3 and SR1-4), the average deviation between test and simulation was 13%. The simulation results were consistently lower than the corresponding empirical measurement. For the full-length bridge-length simulations (in Chapter 4), a correction factor is to be applied to ensure conservatism in the determination of limit states based on stresses in the steel main couplings.

Figure 36. Test-versus-simulation comparison of von Mises stress, σ_{vm}, measurements for dual-bay structural response tests.

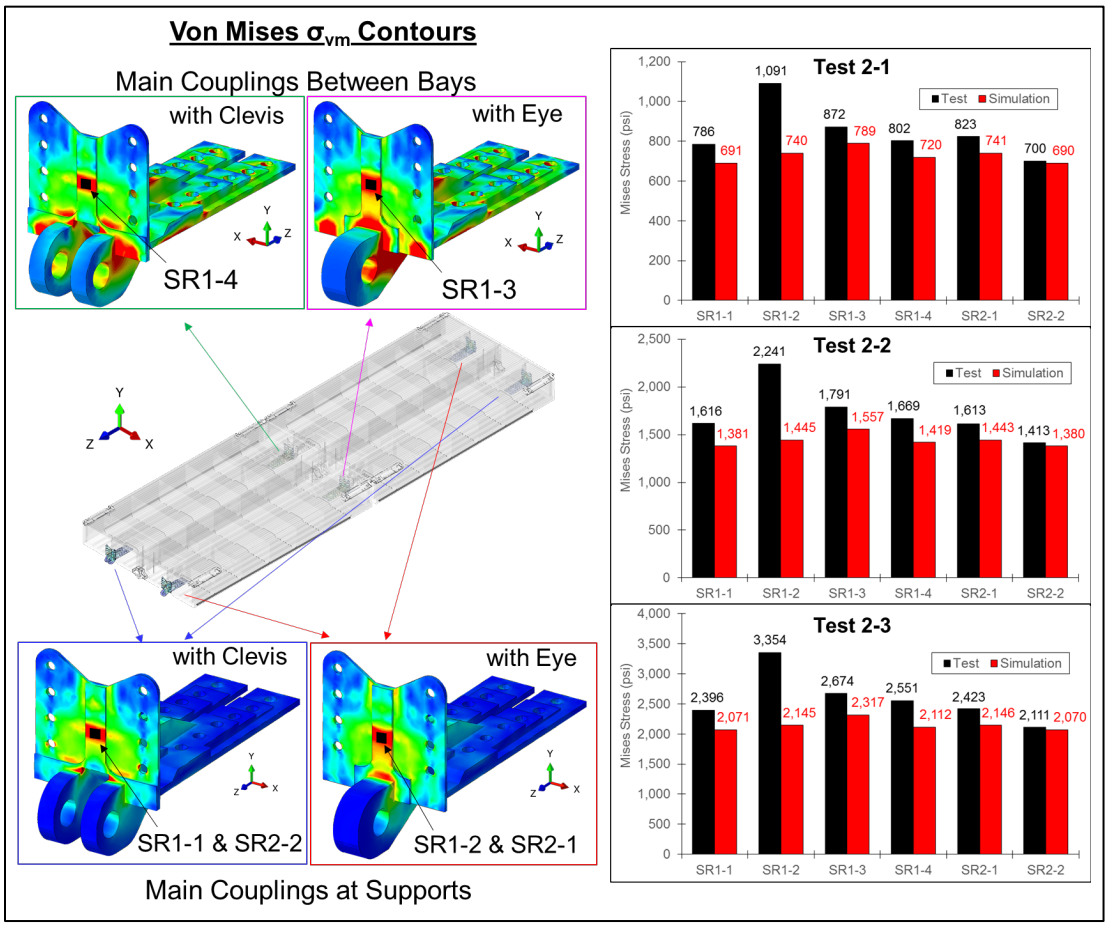


Table 6 summarizes the correlation study for two-bay structural response tests. The uniaxial stress deviations between test and simulation ranged from 1.4% to -15.2%. Recall that all of the uniaxial strain gauges were located on aluminum structure. The average deviation in the aluminum stress measurements over all three dual-bay tests was -9.5%. The von Mises stresses that were measured on the steel couplings deviated from the simulation by -9.8% to -17.9%. The average deviation over all three tests was -15.1%. These correlations could undoubtedly be improved with mesh refinement. However, the computational cost would be significantly increased. The discrepancies in measured versus simulated strain do not necessarily indicate a problem with the FEM. The strain/stress values from the FEM tend to be lower than the measurements. This could be due to the element length being longer than the strain gauge length, so the strain essentially is being smeared over a larger area in the simulation.

The reaction forces at the pin supports deviated by only 1% on average, indicating the mass closely matched in the simulations and tests. The displacement values also show good agreement. The average displacement deviation between test and simulation for the two-bay test series was -6%. The force measurements in the pins connecting the two bays showed a deviation of approximately -5% over all three tests. These results indicate that the physics of the bay-to-bay interactions were appropriately captured.

Table 6. Correlation summary for dual-bay structural response tests.

Measurement Type / Comparable Location	ID	Test 2-1		Test 2-2		Test 2-3	
		Test	FEA	Test	FEA	Test	FEA
Uniaxial Stress / Top, Center of Deck	SA1t-1 (psi)	-199	-190	-396	-383	-600	-572
	SA1t-2 (psi)	-207	-194	-424	-386	-637	-576
	SA2t-1 (psi)	-177	-188	-372	-381	-583	-571
	SA2t-2 (psi)	-171	-192	-368	-384	-581	-573
	Avg. (psi)	*-188*	*-191*	*-390*	*-384*	*-600*	*-573*
	% Dev.	**1.4%**		**-1.7%**		**-4.6%**	
Uniaxial Stress / Bottom, Center of Flange	SA1b-1 (psi)	190	153	387	299	561	446
	SA1b-2 (psi)	158	150	318	297	464	448
	SA2b-1 (psi)	145	153	281	299	427	447
	SA2b-2 (psi)	172	150	333	297	488	447
	Avg. (psi)	*166*	*152*	*330*	*298*	*485*	*447*
	% Dev.	***-9.0%***		***-9.6%***		***-7.8%***	
Uniaxial Stress / Bottom, Qtr. Point of Flange Near Support	SA1b-3 (psi)	145	106	296	208	423	308
	SA1b-5 (psi)	89	103	168	205	245	308
	SA2b-3 (psi)	116	106	223	207	321	308
	SA2b-5 (psi)	143	103	283	207	410	309
	Avg. (psi)	*123*	*105*	*243*	*207*	*350*	*308*
	% Dev.	***-15.2%***		***-14.7%***		***-11.8%***	
Uniaxial Stress / Bottom, Qtr. Point of Flange Near Joint	SA1b-4 (psi)	236	186	467	365	681	546
	SA1b-6 (psi)	198	181	390	363	568	540
	SA2b-4 (psi)	191	186	364	365	542	545
	SA2b-6 (psi)	235	181	475	363	702	541
	Avg. (psi)	*215*	*184*	*424*	*364*	*623*	*543*
	% Dev.	***-14.5%***		***-14.1%***		***-12.9%***	

Mises Stress / Main Coupling at Support	SR1-1 (psi)	786	691	1616	1381	2396	2071
	SR1-2 (psi)	1091	740	2241	1445	3354	2145
	SR2-1 (psi)	823	741	1613	1443	2423	2146
	SR2-2 (psi)	700	690	1413	1380	2111	2070
	Avg. (psi)	*850*	*715*	*1721*	*1412*	*2571*	*2108*
	% Dev.	***-15.8%***		***-17.9%***		***-18.0%***	
Mises Stress / Main Coupling at Bay-to Bay Joint	SR1-3 (psi)	872	789	1791	1557	2674	2317
	SR1-4 (psi)	802	720	1669	1419	2551	2112
	Avg. (psi)	*837*	*755*	*1730*	*1488*	*2612*	*2215*
	% Dev.	***-9.8%***		***-14.0%***		***-15.2%***	
Displacement / Bottom, Center of Flange	D1-1 (in.)	-0.6975	-0.6730	-0.7672	-0.7140	-0.8332	-0.7560
	D2-1 (in.)	-0.6498	-0.6259	-0.7192	-0.6669	-0.7863	-0.7089
	D1-2 (in.)	-0.6861	-0.6618	-0.7564	-0.7028	-0.8240	-0.7448
	Avg. (in.)	*-0.6778*	*-0.6536*	*-0.7476*	*-0.6946*	*-0.8145*	*-0.7366*
	% Dev.	***-3.6%***		***-7.1%***		***-9.6%***	
Displacement / Bay-to-Bay Joint	D3 (in.)	-1.2440	-1.2089	-1.3393	-1.2659	-1.4306	-1.3295
	D4 (in.)	-1.2330	-1.1970	-1.3261	-1.2540	-1.4159	-1.3176
	Avg. (in.)	*-1.2385*	*-1.2029*	*-1.3327*	*-1.2599*	*-1.4232*	*-1.3235*
	% Dev.	***-2.9%***		***-5.5%***		***-7.0%***	
Reaction Force / Pins Support	W1-1 (lb_f)	6320	6617.7	8340	8650.9	10360	10686
	W1-2 (lb_f)	6860	6523	8980	8526.3	11100	10532
	W2-1 (lb_f)	6740	6551.3	8820	8562.4	10880	10576
	W2-2 (lb_f)	6540	6589.4	8560	8614.7	10640	10641
	Avg. *(lb_f)*	*6615*	*6570*	*8675*	*8589*	*10745*	*10609*
	% Dev.	***-0.7%***		***-1.0%***		***-1.3%***	
Connector Force / Pins at Joint Bay-to-Bay Joint	P3Z (lb_f)	33780	31377	43816	41024	53970	50606
	P4Z (lb_f)	32519	31357	42461	41038	52572	50600
	Avg. *(lb_f)*	*33150*	*31367*	*43138*	*41031*	*53271*	*50603*
	% Dev.	***-5.4%***		***-4.9%***		***-5.0%***	

3.1.3 Structural response correlation summary

Table 7 summarizes average deviations between test and simulation for the entire structural response validation test series, comprising three single-bay tests and three dual-bay tests. The metrics for comparisons included stress, displacement, reaction forces, and connector forces. Over the entire test series, stress predictions averaged 11.6% low. Displacement predictions were 3% low on average. Reaction forces were very close, to within 1% on average. For the forces in the pins used to link adjacent bays, the analysis predictions fell short of measured values by an average of approximately 5%. Overall, the simulation results and empirical data show good agreement, indicating that the IRB FEM can accurately predict linear elastic responses and that the physics of the bay-to-bay interactions were appropriately modeled.

Table 7. Correlation summary: average deviations for the entire structural response test series.

	Avg. Stress Deviation	Avg. Displacement Deviation	Avg. Reaction Force Deviation	Avg. Connector Force Deviation
Test 1-1	-15.0%	-6.7%	-0.2%	n/a
Test 1-2	-10.0%	1.4%	-0.2%	n/a
Test 1-3	-10.9%	5.7%	-0.2%	n/a
Test 2-1	-10.6%	-3.3%	-0.7%	-5.4%
Test 2-2	-11.8%	-6.4%	-1.0%	-4.9%
Test 2-3	-11.4%	-8.5%	-1.3%	-5.0%
All Tests	*-11.6%*	*-3.0%*	*-0.6%*	*-5.1%*

3.2 Hydrodynamic loading approach and validation

For the IRB structural finite element analysis, modeling the water explicitly and performing a fluid-structure interaction analysis were not computationally feasible. A simplified approach was needed to represent loading imparted by the fluid to the IRB. The approach to modeling the fluid loads on the IRB is laid out in Section 3.2.1. To validate that the loading methodology was appropriate, a validation study was performed using test data collected during a six-bay IRB raft push test. The push test and simulation thereof is presented in Section 3.2.2. The simulated IRB raft push test results are correlated to the test data in Section 3.2.3.

3.2.1 Hydrodynamic loading approach for the IRB structural analysis

Hydrodynamic loads on the IRB can be divided into two categories: drag and buoyancy. Drag loads are induced by moving water current. Buoyancy loads oppose gravity to keep the bridge afloat. As weight (e.g., from a vehicle) is added, the IRB displaces more water, and the draft increases. An increase in draft increases the wetted surface area and therefore increases the drag force on the bay.

The hydrodynamic characteristics of the IRB were quantified via scaled flume testing in Bryant et al. (2019). In that study, an empirical relationship was developed that could be used to calculate the draft, δ_y (inches), of a single bay.

$$\delta_y = -0.000473\, W^2 + 0.378\, W \tag{6}$$

where W is the combined weight of single IRB bay plus any additional load on the bay (kips).

It was theorized that the buoyancy due to the fluid could be modeled as an elastic foundation. Essentially, each submerged node along the bottom of the IRB could be attached to a vertically oriented spring, and the stiffness of the springs could be calibrated to produce an accurate draft response.

Another empirical equation was also developed in Bryant et al. (2019) that defines drag force on a single IRB bay, $F_{\text{drag.1bay}}$ (lbf), as a function of draft and current velocity.

$$F_{\text{drag.1bay}} = \left(2.44\, \delta_y + 32.18\right) e^{\left(0.002\delta_y + 0.308\right)v} \tag{7}$$

where v is the current velocity (feet/second).

Therefore, if the draft of a bay is known, Equation 7 can be used to calculate the drag force on an IRB bay for any current velocity. That drag force could then be applied to each bay comprising an IRB bridge. In the drag loading approach, it was assumed that the drag force on each individual bay to be uniformly distributed over the wetted surface of the bay. To model the drag load, a distributed surface traction was used (Abaqus load type TRVEC) with a magnitude per unit area equal to

$F_{\text{drag.1bay}} / A_{\text{wetted.surface.1bay}}$.

In summary, the hydrodynamic loading approach involved two steps. In step 1, only gravity loading would be applied. The opposing buoyant force would be supplied by an elastic foundation with a calibrated stiffness on the bottom of each bay. The resulting vertical displacement (i.e., draft) of each bay would then be known and could be used to calculate the drag force on each bay for a given current velocity using Equation 7. In step 2, distributed surface traction vectors, oriented in the direction of flow, would be applied to the wetted surface of each bay. The methodology used to validate this hydrodynamic loading approach is presented next in Section 3.2.2.

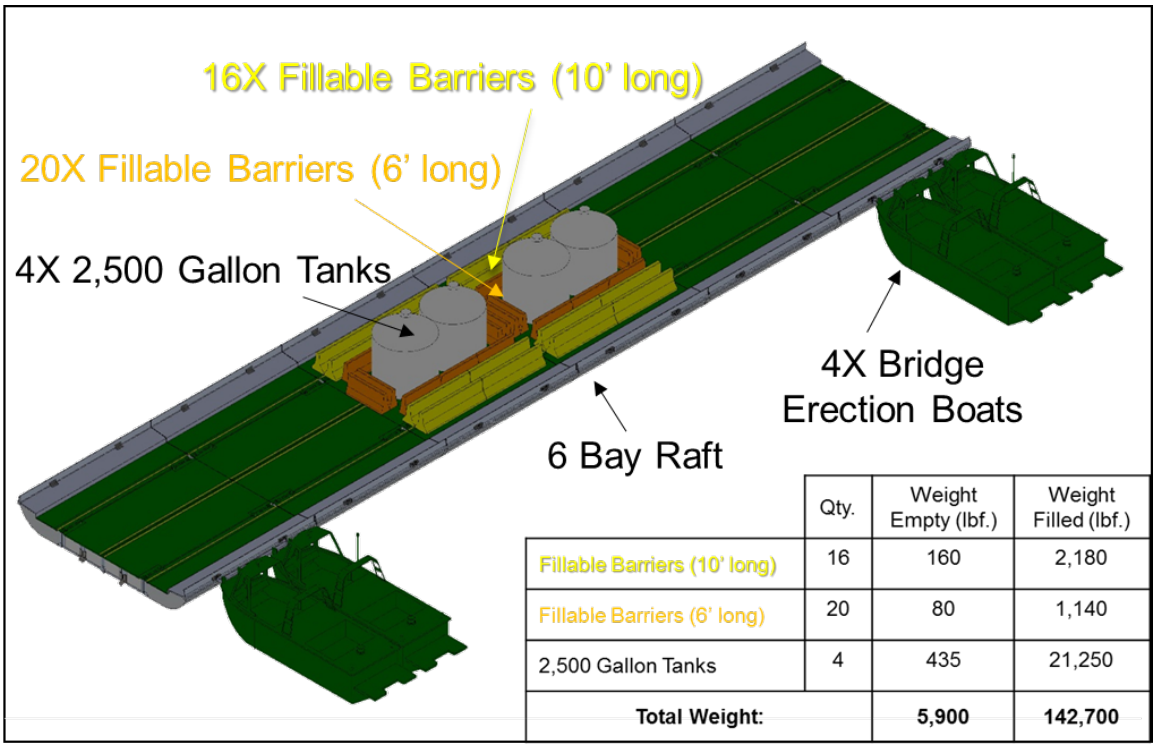
3.2.2 Hydrodynamic loading validation methodology

In October 2017, ERDC performed full-scale testing of a six-bay IRB raft on the Ohio River at Fort Knox to help understand how the IRB behaves in moving water. The full details of the Fort Knox push test can be found in a report by Waller[1].

In summary, the Fort Knox push testing involved pushing a string of six connected interior IRB bays at various speeds and loadings to measure drag under simulated current flow. Water tanks and fillable jersey barriers were used to mimic vehicular loading, and BEBs were used to push the raft down the river. A schematic of the six-bay raft push test arrangement is shown in Figure 37. Figure 38 shows a photograph of the test layout.

[1] Waller, T. In preparation. *Improved Ribbon Bridge Push Test at Fort Knox.* ERDC/CHL Technical Report. Vicksburg, MS: US Army Engineer Research and Development Center.

Figure 37. Six-bay IRB raft push test arrangement.



	Qty.	Weight Empty (lbf.)	Weight Filled (lbf.)
Fillable Barriers (10' long)	16	160	2,180
Fillable Barriers (6' long)	20	80	1,140
2,500 Gallon Tanks	4	435	21,250
Total Weight:		**5,900**	**142,700**

Figure 38. Photograph of six-bay IRB raft push test arrangement.



The test series comprised of five push-test events for which data were recorded. The push test series is summarized in Table 8. For the hydrodynamic loading validation study, the two most extreme cases (test #4 and test #5) were chosen to correlate against. In test #4, all of the barriers and tanks were completely filled with water. The total weight of all the water-filled containers was 142.7 kips. For test #5, all of the barriers and tanks were completely drained. The empty plastic containers that weighed 5.9 kips remained on the raft.

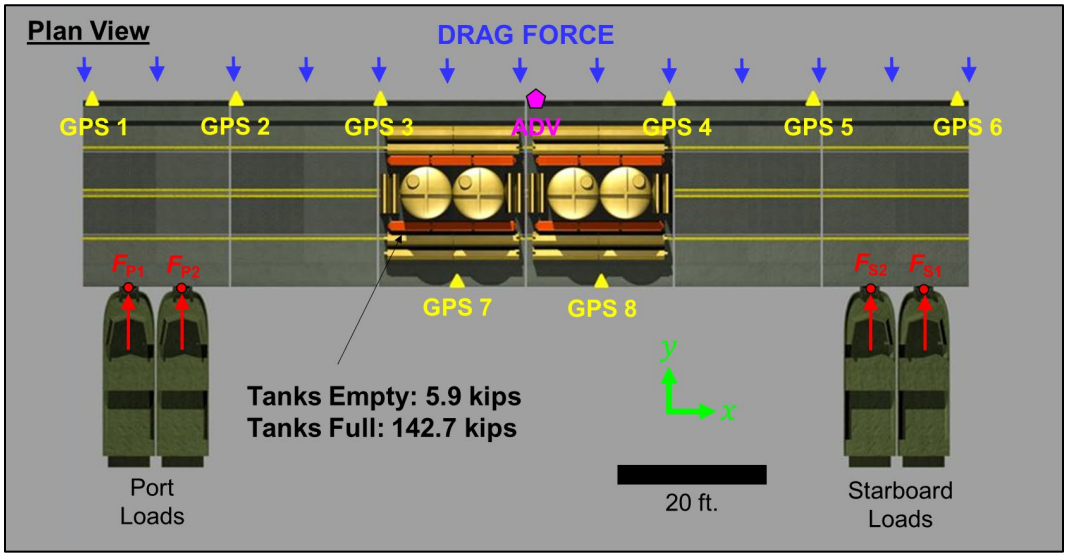
Table 8. Six-bay IRB raft push test series overview.

Push Test #	Date	Weight on Bridge (kips)	Maximum Velocity (ft./s)	Notes
0	17 Oct. 2017	5.9	10	Barriers and tanks empt ; No data collected
1	17 Oct. 2017	59.3	10	Barriers filled; tanks empty
2	17 Oct. 2017	101	10	Barriers filled; two inner tanks filled
3	17 Oct. 2017	142.7	9	Barriers and tanks filled
4*	18 Oct. 2017	142.7	9.1	Barriers and tanks fille ; repeat of test 3
5*	18 Oct. 2017	5.9	10.8	Barriers and tanks empty

* Push test #4 and #5 were chosen for the fluid loading validation study

Figure 39 from Waller et al. (2018) gives an overview of the instrumentation on the IRB raft. The propulsion force from the BEBs was measured with load cells mounted on *push beams* attached to each end bay. These load measurements were used to determine the net drag force on the raft. Position and orientation of IRB bays as a function of time were measured with Global Positioning System (GPS) units. Also, water velocity was measured with an acoustic Doppler velocimeter. For each test, the velocity was increased in approximately 1 ft/s increments. Once a desired velocity was achieved, the raft was pushed along at constant velocity for approximately 1 min while data were recorded. This process was repeated until the maximum velocity shown in Table 8 was achieved for each test.

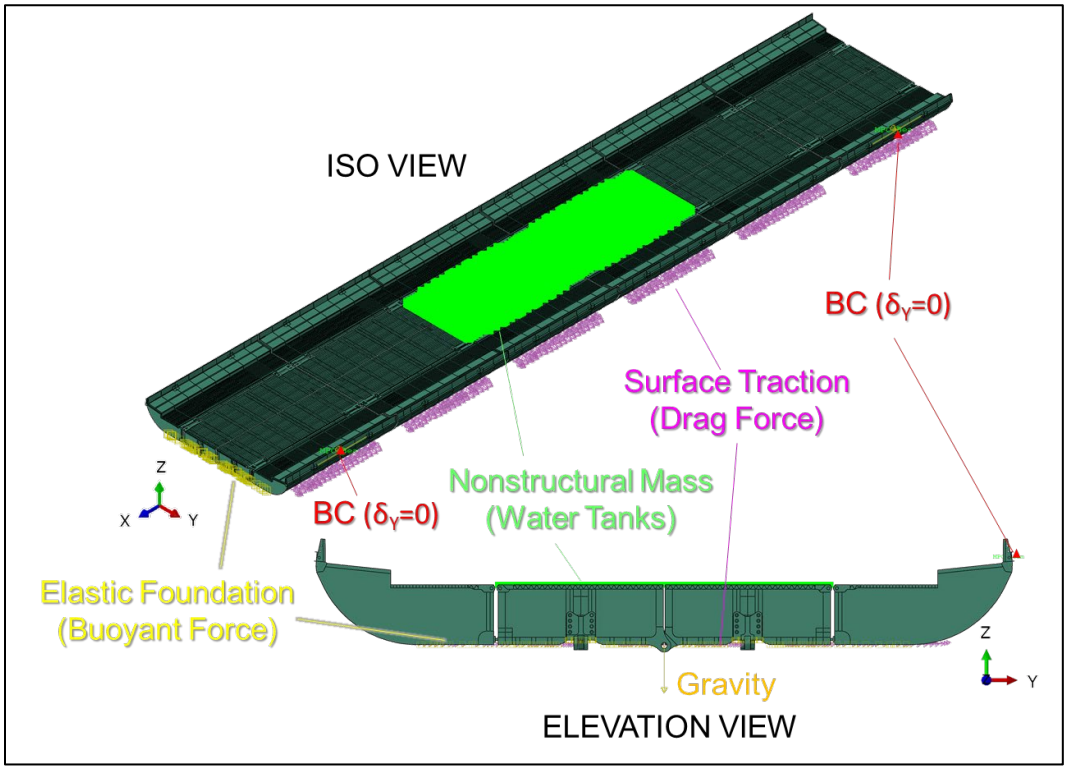
Figure 39. Six-bay raft instrumentation overview (Waller et al. 2018).



To validate the hydrodynamic loading approach, the IRB FEM (described in section 2.2) was conditioned to represent the six-bay raft push test arrangement. The completed six-bay IRB raft push test FEM is shown in Figure 40. The bays were connected and interactions were defined according to Figure 18.

An elastic foundation was defined along the bottom of each IRB bay to represent the buoyant force from the water. The appropriate spring constant per unit area for the elastic foundation was determined as follows. The weight of a single IRB interior bay was previously determined to be $W = 14$ kips. From Equation 6, the draft of a single IRB bay is then $\delta = 5.2$ in. The weight of the bay is opposed by the buoyant force, F_b, so $F_b = W$. The buoyant force that is to be supplied by the elastic foundation has a spring constant, k. Therefore, according to Hooke's Law, $k = F_b/\delta = W/\delta = 2.7$ kip/in. The elastic foundation is distributed over the bottom surface of each bay, an area of $A_b = 55{,}284$ in.^{2}. Thus, the elastic foundation stiffness per unit area was determined to be $k/A_b = 4.87\text{E-}5$ kip/in.^{3}.

Figure 40. Six-bay IRB raft push test FEM.



Nonstructural mass, uniformly distributed over the decks of the two center bays, was used to represent the mass of the fillable containers. Note this was the same method used to mimic vehicular weight in the structural response validation study conducted in section 3.1. For the *tanks-filled* (test #4 from Table 8) condition, 142,700 lb of mass was added. For the *tanks-empty* testing condition (test #5 from Table 8), added mass totaled 5,900 lb.

Next, a rigid push beam was used to join the two support brackets on each end bay using MPC beam keywords. The MPC reference node for each beam was assigned a boundary condition to prevent translations in the y direction ($\delta_y = 0$). Acceleration due to gravity was applied to the entire model using g= 386.09 in./s^2. The structure was then allowed to respond (i.e., draft in the z direction) under the influence of gravity.

Once the drafts (z-displacements) of each bay were calculated, distributed surface traction vectors oriented in the y direction were applied to the wetted surface of each bay. The magnitude of the drag force on each bay was calculated by substituting the average draft of each bay and the velocities attained during testing into Equation 7. The velocity cases that

were simulated are tabulated in Table 9. For the tanks-empty condition, six velocities were used over the range of 1.2 ft/s - 10.8 ft/s. For the tanks-full condition, five velocity conditions were simulated ranging from 1.2 ft/s to 9.1 ft/s.

Table 9. Six-bay IRB raft simulations.

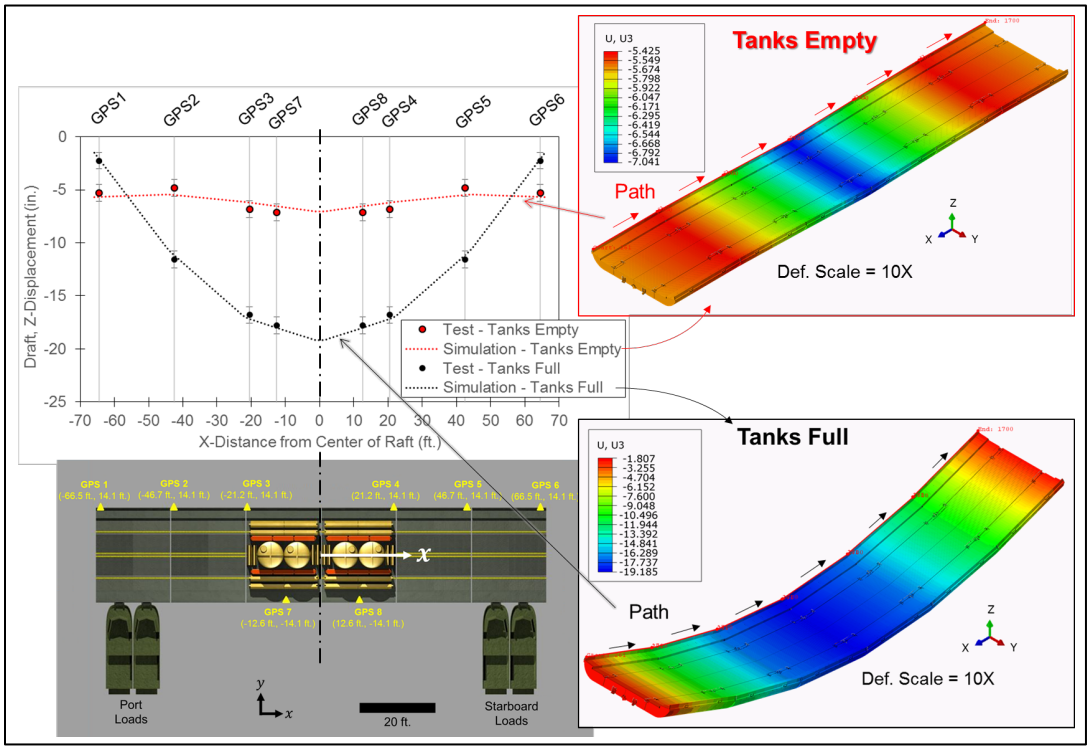
Simulation ID	Nonstructural Mass (lb)	Velocity (ft./s)
6bay - Empty - 1.2 ft./s	5,900	1.2
6bay - Empty - 2.9 ft./s		2.9
6bay - Empty - 4.9 ft./s		4.9
6bay - Empty - 6.8 ft./s		6.8
6bay - Empty - 8.6 ft./s		8.6
6bay - Empty - 10.8 ft./s		10.8
6bay - Full - 1.2 ft./s	142,700	1.2
6bay - Full - 2.4 ft./s		2.4
6bay - Full - 4.3 ft./s		4.3
6bay - Full - 6.9 ft./s		6.9
6bay - Full - 9.1 ft./s		9.1

3.2.3 Six-bay raft push test/simulation correlation

To validate the approach of using an elastic foundation to model buoyancy, the displacements in the *z* direction from the simulations to the GPS data obtained during testing were compared. Figure 41 compares the test-versus-simulation draft (*z*-displacement) response of the six-bay raft for the tanks-empty and tanks-full conditions. The error bars for each empirical data point correspond to the resolution of GPS units used in the tests (±2 cm). The simulation results and test data demonstrate strong correlation for both load conditions. Therefore, using an elastic foundation to model buoyancy is a valid approach.

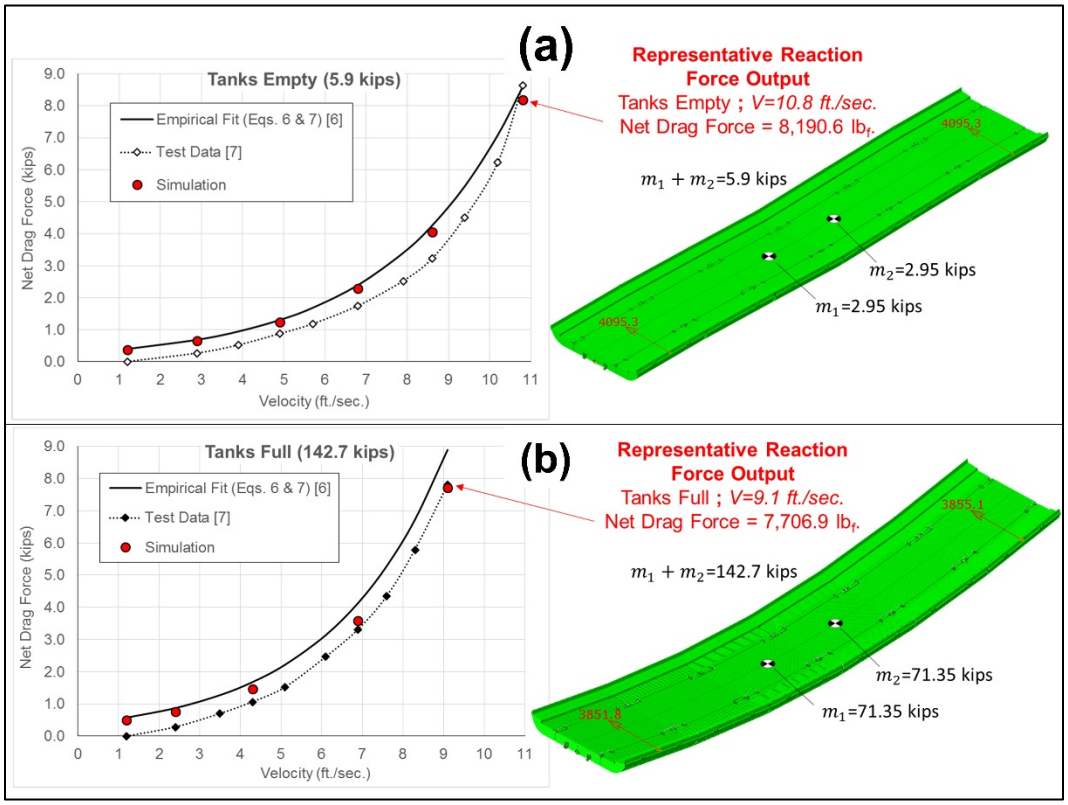
Convinced that the model was drafting correctly, the average draft value of each bay was plugged into Equation 7, and the drag force on each bay was calculated for each velocity listed in Table 9. The resulting drag forces were applied as distributed surface tractions as described in Section 3.2.1. Simulations were run for the various velocities listed in Table 9.

Figure 41. Draft (*z*-displacement) test-versus-simulation comparison of the six-bay raft for tanks-empty and tanks-full conditions.



The net reaction forces obtained from summing the two reaction forces at each boundary condition are compared to the test data (dotted line) and the empirical curve generated using Equation 7 (solid line) in Figure 42. The empirical fits in Figure 42 were generated as follows. For the six-bay raft, four of the bays had no added weight, but the two center bays did have additional weight. For the four empty bays, W = 14 kips was substituted into Equation 6, which resulted in a draft of δ = 5.2 in. For the two center bays, $W_{TanksEmpty}$ = 14 kips + 2.95 kips = 16.95 kips was used for the tanks-empty case, and $W_{TanksFull}$ = 14 kips + 71.35 kips = 85.35 kips was used for the tanks-full case. The resulting drafts for the two center bays were $\delta_{TanksEmpty}$= 6.2 in. and $\delta_{TanksFull}$= 28.6 in. These draft values were then substituted into Equation 7 to determine the drag force on the two loaded, center bays and the four outer bays. The net reaction force was obtained by summing the drag forces on all six bays.

Figure 42. Drag force on six bay IRB raft: test-versus-simulation comparison for (a) tanks-empty condition and (b) tanks-full condition.



Note that the use of Equation 6 does an excellent job when used to calculate single bay drafts; however, it breaks down when used to calculate drafts for multiple bays with a distributed load. Using Equation 6 for the tanks-full case, $\delta_{TanksFull.Eq6}$= 28.6 in. was calculated. From Figure 41, the average draft of the two center bays was actually $\delta_{TanksFull.Simulation}$= 18.2 in. Equation 6 does not account for additional buoyancy provided by adjacent bays. The simulation accounts for the additional buoyancy, as well as the additional stiffness that occurs when adjacent bays come into contact, and produces a multi-bay draft response that closely matches test data.

The net reaction forces from the simulations show excellent correlation when compared against the test data and the empirical curve, as shown in Figure 42. This validates that the modeling approach using distributed traction vectors to represent fluid drag produces accurate loadings. Overall, the combined hydrodynamic loading approach using an elastic foundation to provide buoyancy and distributed surface tractions to model drag demonstrated strong correlation to test data, as evidenced by the comparisons in Figure 41 and Figure 42.

4 Structural Analysis of the IRB Subjected to Hydrodynamic and Vehicular Loading

The computational modeling methodology used to generate the IRB FEM was covered in Chapter 2, and the FEM validation procedure was documented in Chapter 3. This chapter presents the structural analysis of the 110 m and 210 m IRB crossings subject to hydrodynamic and vehicular loading. The analysis methodology is provided in Section 4.1. The results of the 15-bay (110 m) and 30-bay (210 m) IRB crossing analyses are presented in Sections 4.2 and 4.3, respectively. Section 4.4 provides a final summary and lists conclusions.

4.1 Structural analysis methodology

This section describes the structural analysis methodology for the 110 m and 210 m IRB crossings based on hydrodynamic drag and vehicular loading. The analysis makes use of the validated modeling procedures previously described in Chapters 2 and 3. Section 4.1.1 outlines the analysis cases considered. Section 4.1.2 describes the IRB FEM conditioning procedure, and section 4.1.3 discusses how the allowable limits were determined.

4.1.1 Analysis cases

The finite element analysis cases used to determine the limit states of the IRB under hydrodynamic and vehicular loading are listed below.

- IRB crossing spans
  - 110 m crossing (15 IRB interior bays)
  - 210 m crossing (30 IRB interior bays)
- IRB crossing types
  - No vehicles on bridge
  - Risk crossing (only one 72-ton vehicle on bridge at a time)
  - Normal crossing (multiple 72-ton vehicles on bridge, spaced ~100 ft apart)
- Water current speeds
  - 0 ft/s
  - 1 ft/s
  - 3 ft/s
  - 5 ft/s
  - 7 ft/s
  - 9 ft/s
  - 11 ft/s
  - 15* ft/s
  - 18* ft/s

* 15 ft/s and 18 ft/s cases will be analyzed if a limit state is not reached at a lower velocity.

The two crossing spans were chosen on the basis that each Army MRBC is authorized 30 IRB interior bays, providing up to 210 m of bridging (Department of the Army 2009). This is the significance of the 210 m crossing. To better understand how the crossing span influences IRB loading, a 15-bay (110 m) bridge crossing was chosen as a second analysis case.

The IRB Operator Manual (Department of the Army 2003a) defines three crossing types for heavy equipment (i.e., normal, caution, and risk). The type of crossing dictates the minimum spacing between vehicles traversing the IRB. For a normal crossing, the minimum spacing is 100 ft. For a caution crossing, the minimum spacing is set at 170 ft. For a risk crossing, only one vehicle is allowed on the bridge at a time. The water flow velocity at the bridge site dictates which crossing type is to be used.

The two extreme cases (normal and risk) were selected for analysis. An M1 tank with a nominal weight of 72 tons was chosen as a representative heavy vehicle for the normal and risk crossings. An analysis case with no vehicles on the bridge was also of interest in consideration of a scenario where a bridge had been constructed and a brief increase in flow was expected, perhaps due to weather conditions. It would be useful to know whether or not the bridge could sustain the increased fluid loading to inform a decision of whether or not the bridge should be disassembled or provided with additional support.

Up to nine water current speeds were chosen for analysis to encompass the entire range of interest up to 18 ft/s. The IRB Operator Manual (Department of the Army 2003a) specifies 11 ft/s as the maximum allowed water current speed for IRB bridging; however, no rationale for this limit is provided. How this limit was established was indeterminable from available resources.

4.1.2 IRB FEM conditioning procedure

The IRB FEM described in Chapter 2 was conditioned to simulate the desired analysis cases. The required modifications to the IRB FEM are summarized below. Schematic overviews of the 15-bay (110 m) and 30-bay (210 m) IRB FEM models are shown in Figure 43 and Figure 44, respectively.

- The appropriate number of bays (either 15 or 30) were linked via hinge connectors, and contact surfaces were assigned between each bay, as shown in Figure 18.
- Non-structural mass was added to represent vehicular loads in the same manner as shown in Figure 40.
    - For no vehicle crossings: no mass added.
    - For risk crossings: 72 tons of added mass was distributed over a 22 ft × 12 ft deck area, centered on the bridge (representative of a M1 tank at the mid-span of the bridge).
    - For normal crossings: Multiple instances of the same distributed mass used for risk crossings were applied. One mass was centered on the mid-span of the bridge. The other masses were evenly spaced every five bays along the length of the bridge (representative of multiple M1 tanks spaced ~100 ft apart).
- An elastic foundation was added to the bottom surface of each IRB bay to model buoyancy provided by the water. The foundation stiffness per unit area was set as 4.87E-5 kip/in.^{3}. This value was validated to produce the correct draft response (see Section 3.2).
- A surface traction in the $+x$ direction was defined for the bottom surface of each IRB bay to model the drag force produced by moving water. The magnitude of the drag force on each bay was calculated as a function of draft and velocity using Equation 7.
- Boundary conditions were applied to the reference nodes associated with the two main couplings on each end of the bridge. These are the couplings that would be connected to ramp bays in the field. The four main coupling reference nodes were prescribed by the boundary condition $\delta_x = 0$ (i.e., zero displacement in the x [transverse] direction). One of the reference nodes was assigned an additional boundary condition, $\delta_z = 0$, to constrain rigid-body motion in the z (longitudinal) direction.
- Acceleration due to gravity, g= 386.09 in./s^2, was applied to the entire model in the negative y (vertical) direction.

Figure 43. Overview of 15-bay (110 m) IRB bridge FEMs illustrating the three vehicular loading cases (no vehicles, risk crossing, and normal crossing), boundary conditions, and applied drag loading.

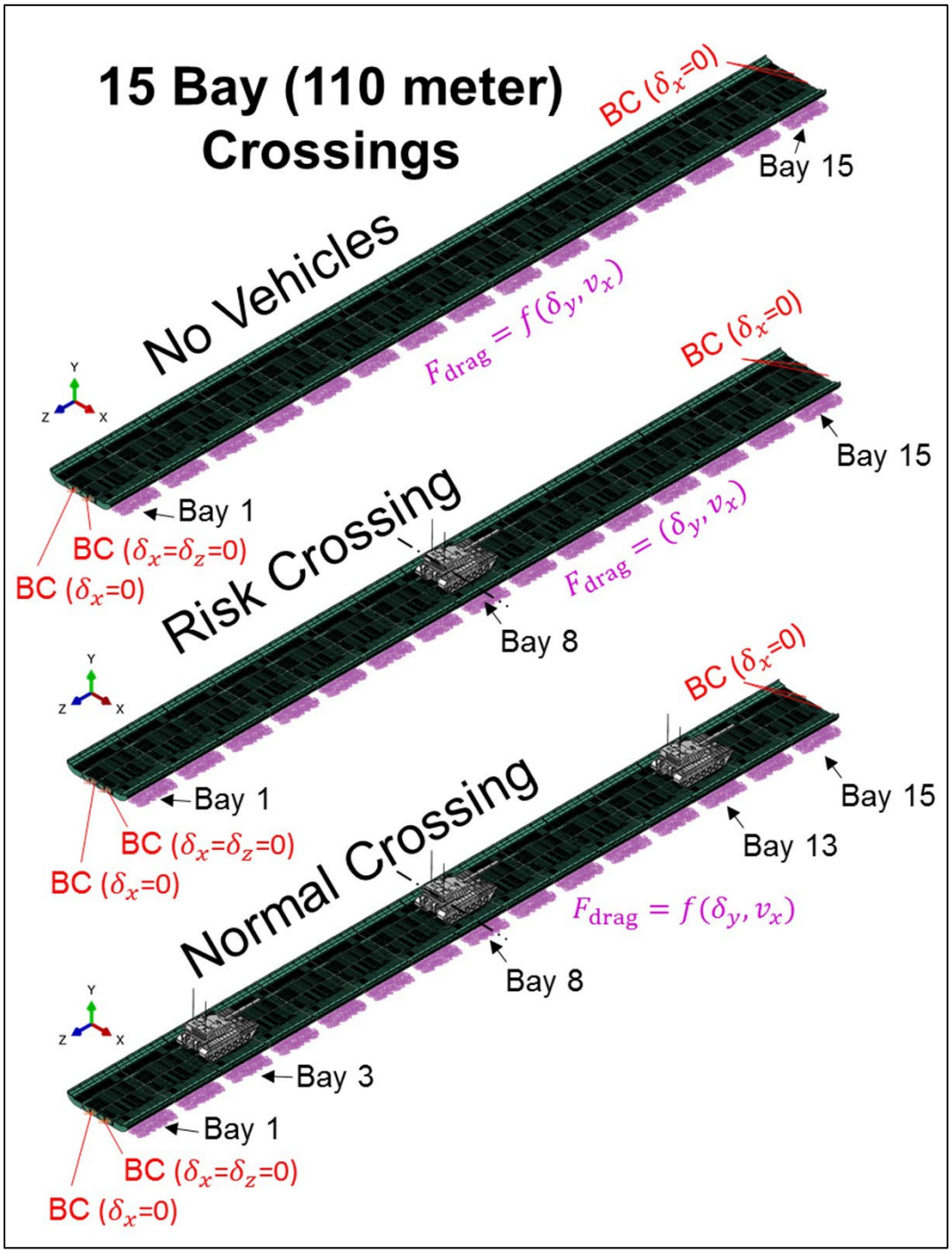
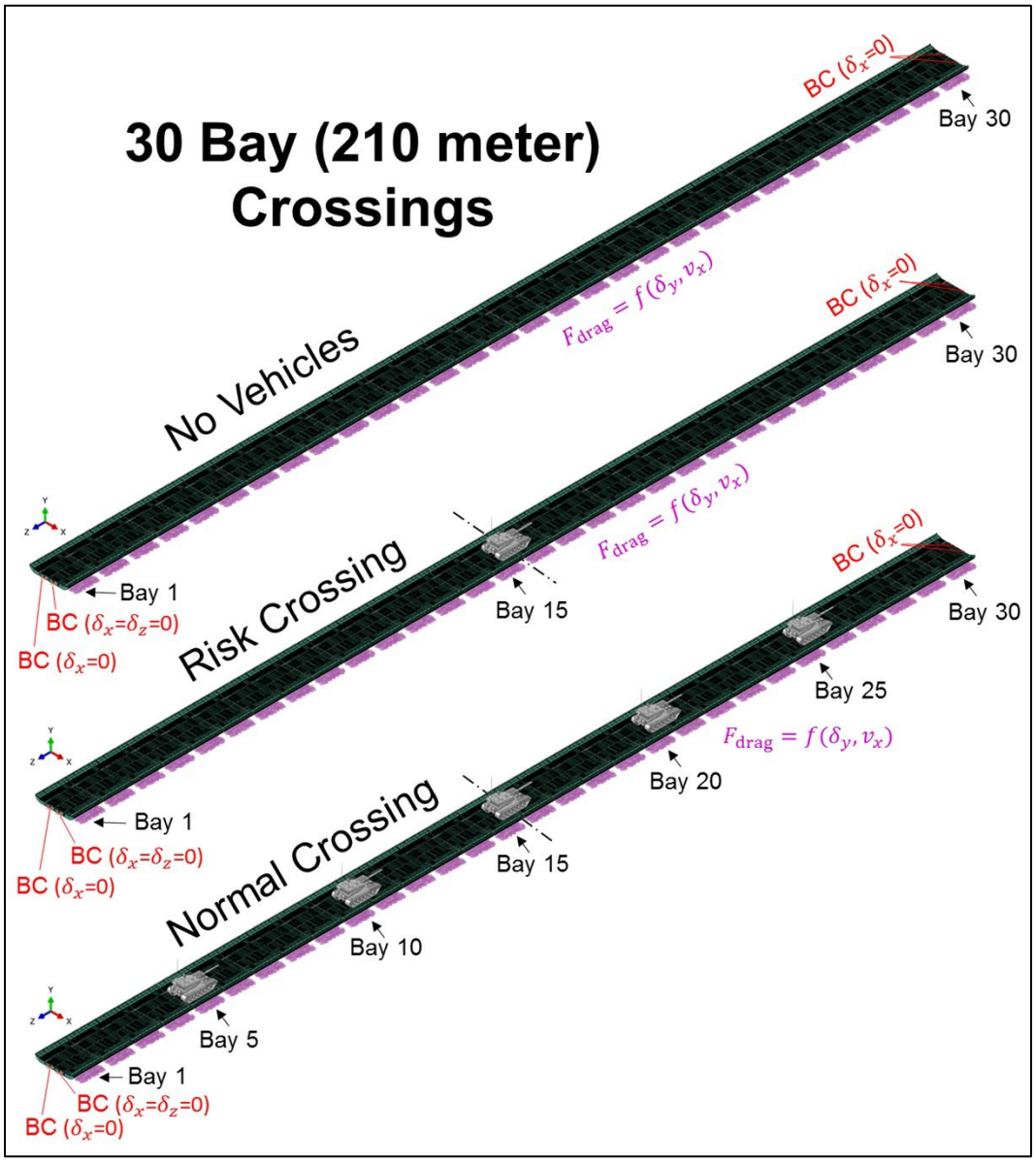


Figure 44. Overview of 30-bay (210 m) IRB bridge FEMs illustrating the three vehicular loading cases (no vehicles, risk crossing, and normal crossing), boundary conditions, and applied drag loading.



4.1.3 Determination of allowable limits

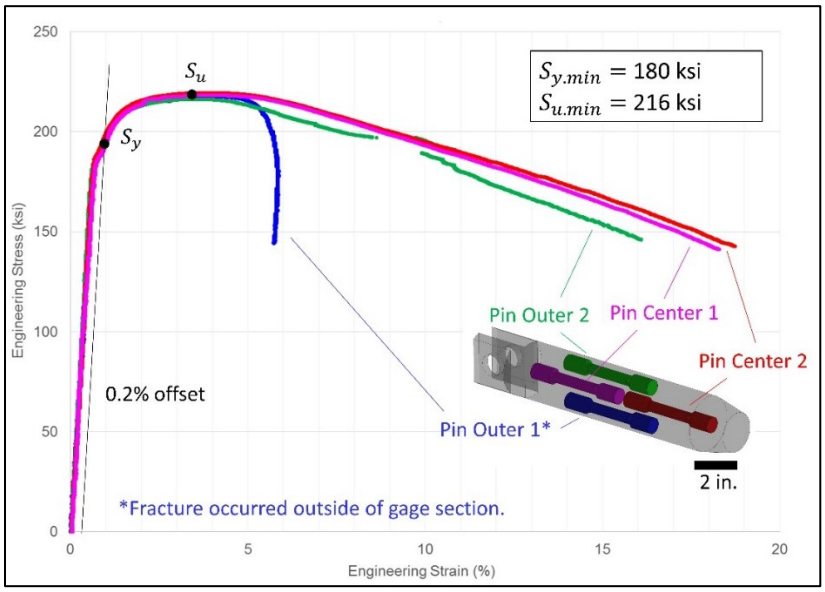
In this section, there is a description of the procedure used to determine the allowable load and stress limits for the IRB. These limits will be used as the pass/fail criteria during post-processing of the M&S results.

To evaluate the strength of the steel pins used to connect the IRB bays, tensile testing was performed in accordance with standard ASTM-E8 (ASTM International 2011). Four round specimens with 2 in. gauge

lengths and 0.5 in. gauge diameters were harvested from a single IRB main coupling pin. It was unknown if the pins were case hardened, so two of the specimens were harvested from the center of the pin, and two specimens were harvested from the periphery of the pin.

The tensile test results used to determine the strength of the pin are shown in Figure 45. All four specimens produced similar responses with the exception of one specimen. The *pin outer 1* specimen exhibited much lower elongation compared to the other samples. This was due to the specimen fracturing outside of the gauge length, so the localized plastic strain associated with necking was not captured. The yield and ultimate strengths were within a ±2 ksi range for all four specimens, with the minimum 0.2% offset yield strength and ultimate strength being 180 ksi and 216 ksi, respectively. To ensure conservatism, these minimum strength values were used to define the allowable limits for the pins.

Figure 45. Tensile test results for the four ASTM-E8 specimens harvested from main coupling pin.

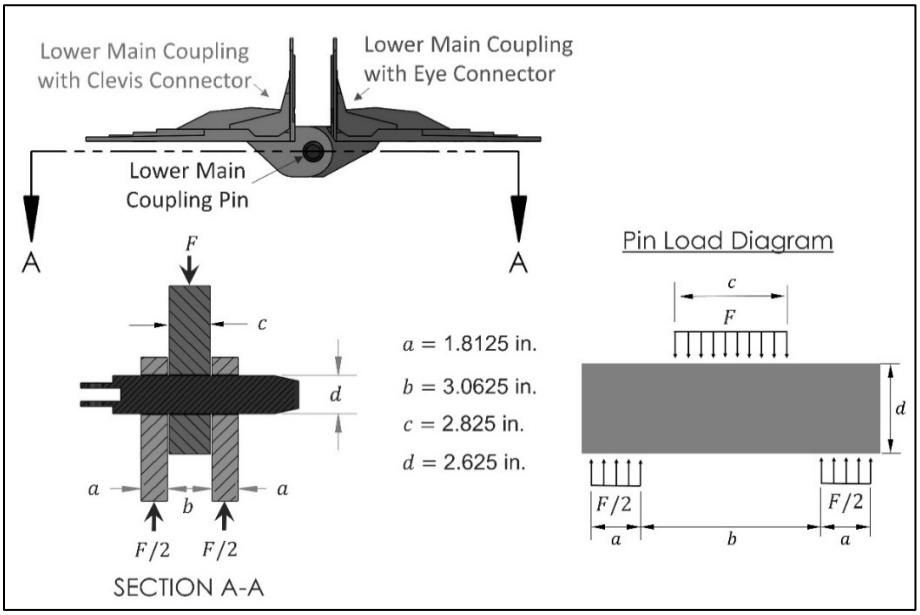


For ductile materials, the Trilateral Design and Test Code for Military Bridging and Gap-Crossing Equipment (US Army Tank-Automotive & Armaments Command 1996) specifies that the maximum allowable von Mises stress, σ_α, for a material with yield strength, S_y, is

$$\sigma_\alpha = \frac{0.9\,S_y}{1.33} \approx 0.677\,S_y \tag{8}$$

The lower pin limit states are developed from an idealized stress analysis of the bending, shear, and bearing stresses in the pin. The limit state is defined by the allowable stress defined by Equation 8 (US Army Tank-Automotive & Armaments Command 1996). For the analysis of bending and shear stresses, the pin is treated as a beam loaded with the total force F applied by the single-eye-hinge butt coupling and the corresponding opposing force applied by the double-eye-hinge butt coupling as shown in Figure 46.

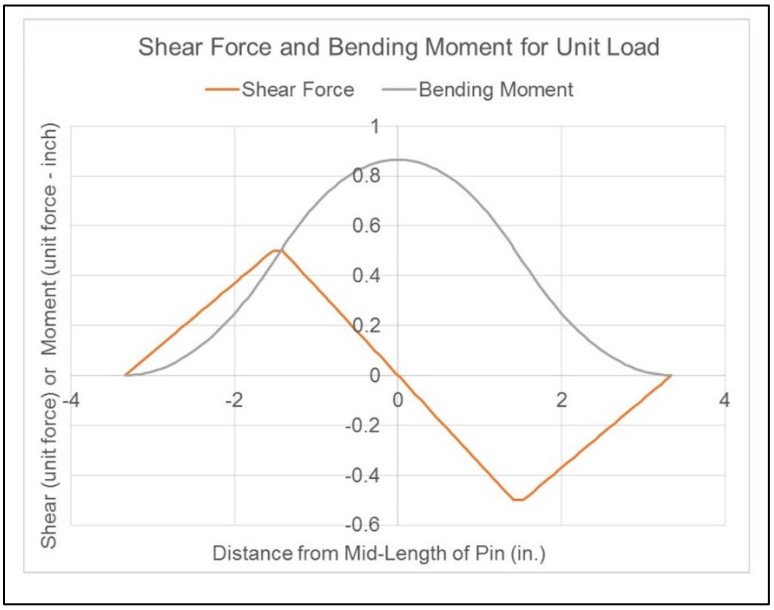
Figure 46. Lower main coupling pin connection schematic and load diagram.



The shear force and bending moment diagrams for a unit load (F =1) are shown in Figure 47. The points of interest are the maximum shear and the maximum moment. However, the minimum allowable pin force is controlled by the extreme fiber bending stress at the location of maximum moment. (The von Mises stress at other locations are less than the maximum flexural stress.) The bending stress at the extreme fiber of the pin from a 1 kip load (F =1 kip) at the location of maximum moment is given by

$$\sigma_{unit\ force\ bending} = \frac{M\,(d/2)}{I} = \frac{32M}{\pi\, d^3} = 0.4875\,\frac{ksi}{kip} \tag{9}$$

Figure 47. Shear force and bending moment for unit load applied to pin.



From US Army Tank-Automotive & Armaments Command (1996), the allowable stress for bending and/or tension is the smaller of 75% of the yield stress or 67% of the ultimate strength. For the pins (based on tensile tests), the yield stress controls and results in an allowable stress of 135 ksi (180 ksi * 0.75). For combined (normal and shear) stresses, the von Mises yield criteria is used, and the limit state is defined such that the von Mises stress may not be greater than 90% of the allowable normal stress. This corresponds to an allowable von Mises stress of 121.5 ksi (from Equation 8 with S_y = 180 ksi) for combined normal and shear stress.

The maximum bending moment in the pin occurs at a mid-length of the pin where the shear force is zero. However, there is shear force at an infinitesimal distance from the mid-length and corresponding shear stress an infinitesimal distance from the extreme fiber of the pin where the bending stress is maximum. Because of the proximity of shear stresses to the maximum bending stress combined with the fact that the pins are non-redundant members, the limit state is based on the von Mises criteria with the shear stress equal to zero. The maximum allowable load for the pin considering the max bending stress at the location of maximum moment is given by

$$F_{\alpha.pin} = \frac{\sigma_{\alpha.Stl}}{\sigma_{unit\ force\ bending}} = \frac{121.5}{0.4875}\ \text{kips} \approx 250\ \text{kips} \qquad (10)$$

Stress analysis per Maddux et al. (1969) showed the pin is the weakest element. This makes for good design since the IRB will remain watertight in the event that the pin fails.

All of the aluminum IRB components are composed of 6061-T6 aluminum alloy. The properties of 6061-T6 are highly controlled and well understood; thus, mechanical property testing of that material was not performed. A yield strength of $S_{y.Al}$ = 35 ksi for the aluminum was assumed, which is conservative given the minimum yield strength of 6061-T6 aluminum is typically 40 ksi. By substituting $S_{y.Al}$ = 35 ksi into Equation 8, the allowable von Mises stress for the IRB aluminum components was found to be $\sigma_{\alpha.Al}$=24 ksi.

4.2 Structural analysis of the 15-bay (110 m) IRB

Table 10 shows the simulation matrix for the 110 m (15-bay) IRB crossings. A total of 24 simulations were executed using the 15-bay IRB FEM. Note the 18 ft/s current speed was not analyzed. It will be shown later in Section 4.2.4 that limit states were reached prior to achieving the threshold speed of 18 ft/s, so simulations for velocities greater than 15 ft/s were unnecessary.

Table 10. Simulation matrix for the 110 m (15-bay) IRB crossings.

Crossing Type	Current Speeds (ft/s)
No Vehicles	0, 1, 3, 5, 7, 9, 11, 15
Risk Crossing (1x 72 ton vehicle)	0, 1, 3, 5, 7, 9, 11, 15
Normal Crossing (3x 72 ton vehicles)	0, 1, 3, 5, 7, 9, 11, 15

Section 4.2.1 presents the draft (vertical displacement) results for the 15-bay IRB simulations, where no drag load was applied (v = 0 ft/s). These draft results were used to calculate the fluid drag loading using Equation 7. The fluid drag results for the 15-bay IRB are given in Section 4.2.2. The drag induced displacement results are provided in Section 4.2.3. Finally, the load and stress M&S results are presented and compared to the previously determined allowable limits in Section 4.2.4.

4.2.1 Draft (vertical displacement) of the 15-bay IRB

The first step in performing the structural analysis of the 110 m (15-bay) IRB was to apply the nonstructural mass (representing the vehicular loads) and gravity loading only to the 15-bay IRB FEM. This allowed determination of the draft (vertical displacement) of each IRB bay. These drafts could subsequently be substituted into Equation 7 to calculate the drag load on each bay. Figure 48 shows the draft response of the 15-bay bridge for the three vehicular loading cases analyzed (i.e., no vehicles, risk crossing, and normal crossing). Figure 49 plots the average draft of each bay over the length of the bridge.

Recall an elastic foundation was used to model buoyancy from the water. With no vehicles on the bridge, the entire bridge displaces in the *y* direction by 5.2 in. due to self-weight. For the risk crossing, the mass of one 72-ton vehicle was placed on the center of the bridge on bay 8. This results in a maximum draft of ~21 in. at bay 8 in the middle of the bridge. The weight gets distributed over five bays (bays 6, 7, 8, 9, and 10). The draft of the remaining bays is ~5.2 in., the same as in the no-vehicles case. For the normal crossing, three 72-ton masses were placed on the bridge at the locations shown in Figure 48. Similar to the risk crossing, a maximum draft of ~21 in. was observed at each vehicle location.

Figure 48. Contour plots for the three vehicular loading cases showing draft (*y* displacement) of the 15-bay (110 m) IRB. Deformation scale = 5x.

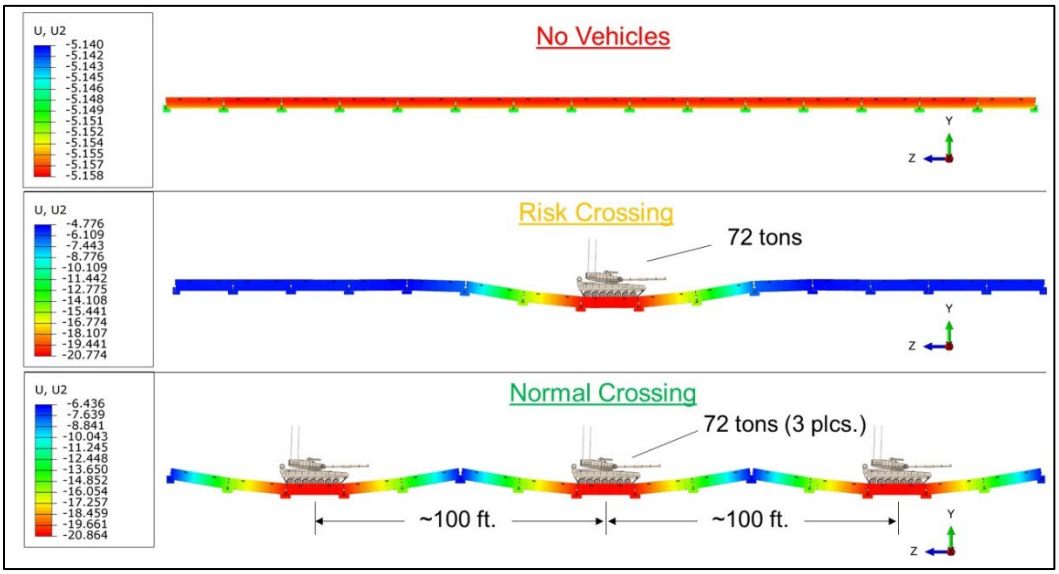
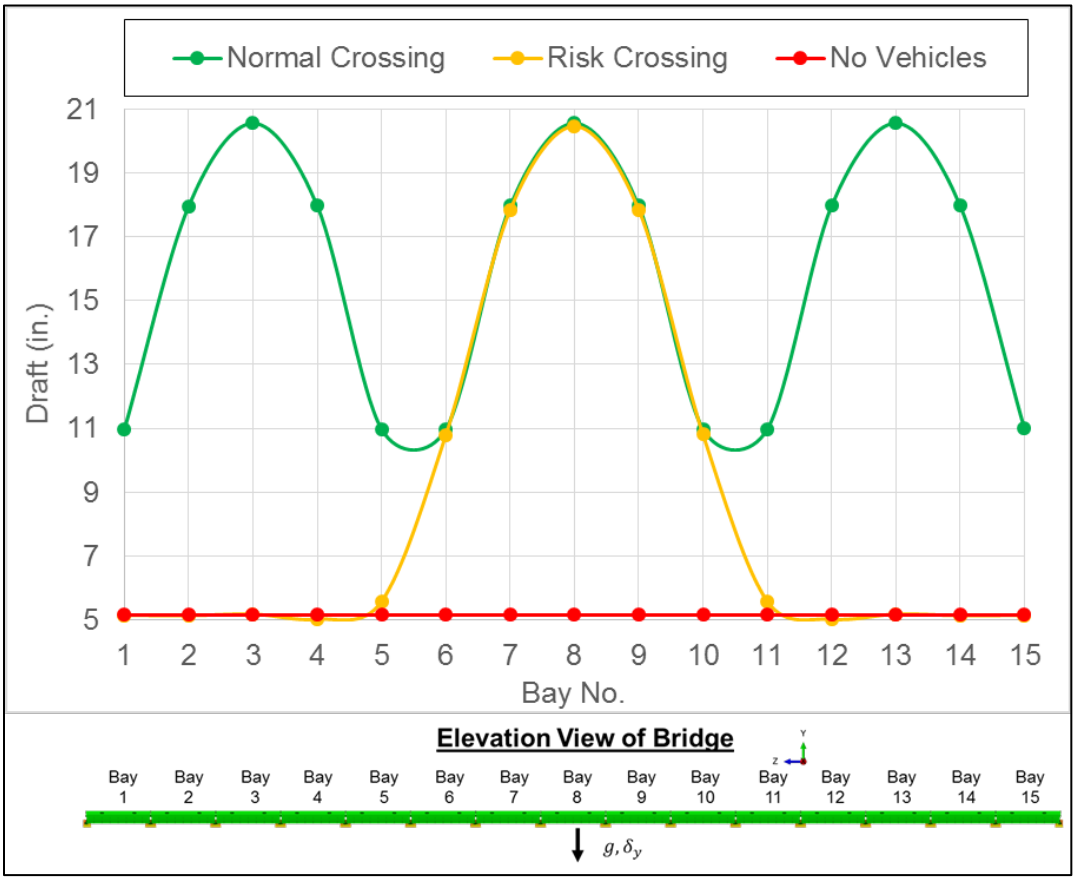


Figure 49. Draft (y-displacement) of the 15-bay (110 m) IRB for the three vehicular loading cases (i.e., no vehicles, risk crossing, and normal crossing.)



4.2.2 Drag loading on the 15 bay IRB

The draft of each bay (from Figure 49) was then substituted into Equation 7, and the drag force on each bay could be calculated over the range of current velocities of interest. The resulting drag force distribution along the length of the 15-bay IRB for the no-vehicles scenario is plotted in Figure 50. With no vehicular loading, the draft of the bridge is constant; therefore, the drag force on each bay is also constant for a given current velocity.

Figure 50. Drag force distribution along the 110 m (15-bay) IRB over a range of current velocities for the no-vehicles scenario.

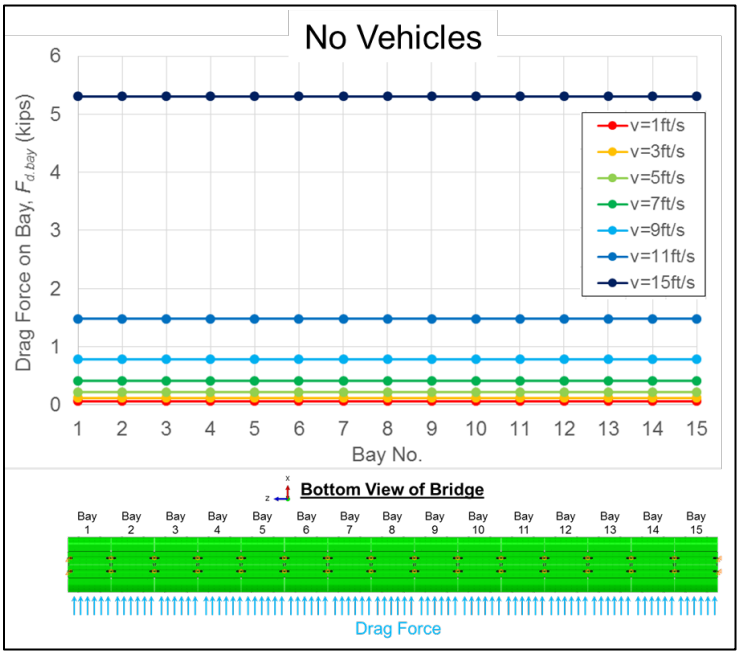


Figure 51 shows the drag force distribution for the risk crossing scenario with one 72-ton vehicle on the center of the 15-bay IRB. Similarly, the drag force on each bay for the normal crossing with three 72-ton vehicles spaced ~100 ft apart on the 15-bay IRB is plotted in Figure 52.

Figure 51. Drag force distribution along the 110 m (15-bay) IRB over a range of current velocities for the risk-crossing scenario.

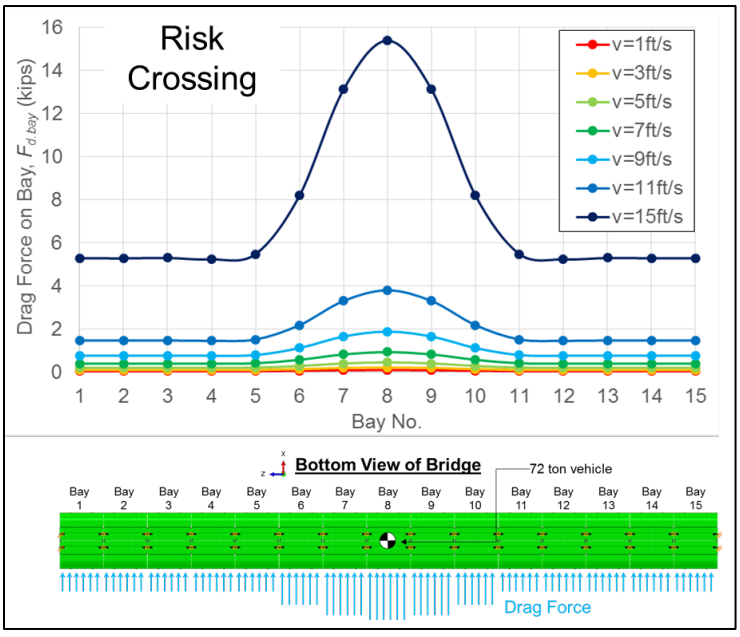
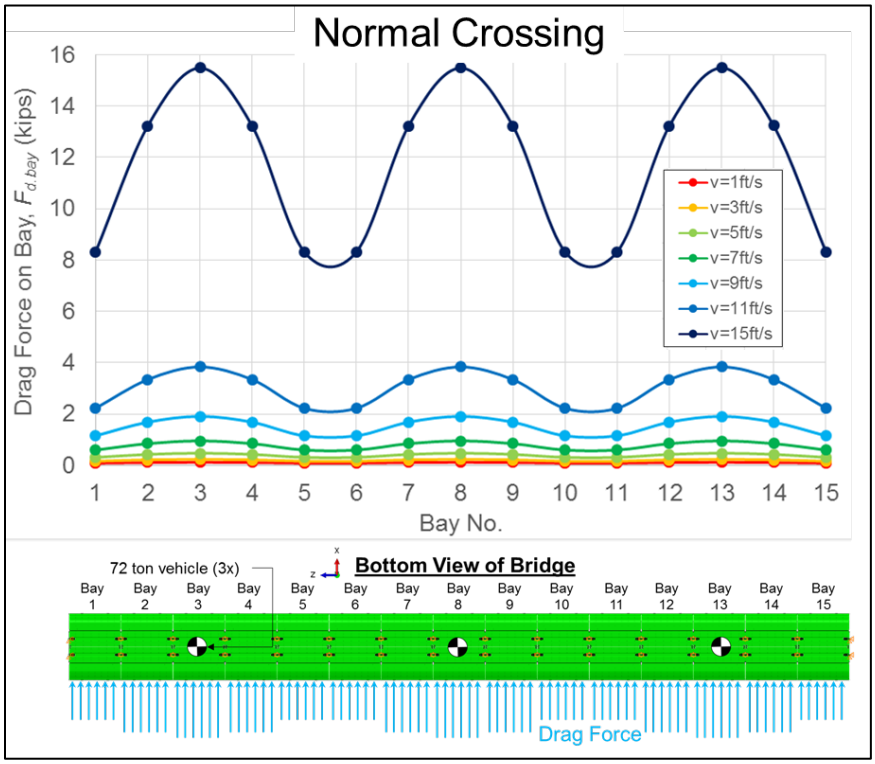


Figure 52. Drag force distribution along the 110 m (15-bay) IRB over a range of current velocities for the normal-crossing scenario.



The drag force on each bay was applied to the bottom, wetted surface of each bay via a distributed traction vector (i.e., a drag per unit area was applied to the bottom of each bay). The surface area of each bay over which the drag force was distributed measured 42,108 in.^{2}. For example, for the no-vehicles scenario and a current velocity of 15 ft/s, the drag force on each bay is 5.3 kips (from Figure 50). Therefore, a drag per unit area of 5.3 kips/42,108 in.^{2} = 0.126 kip/in.^{2} was applied to the bottom surface of each bay in that simulation. The other simulations for the various velocities and vehicular load cases were conducted the same way.

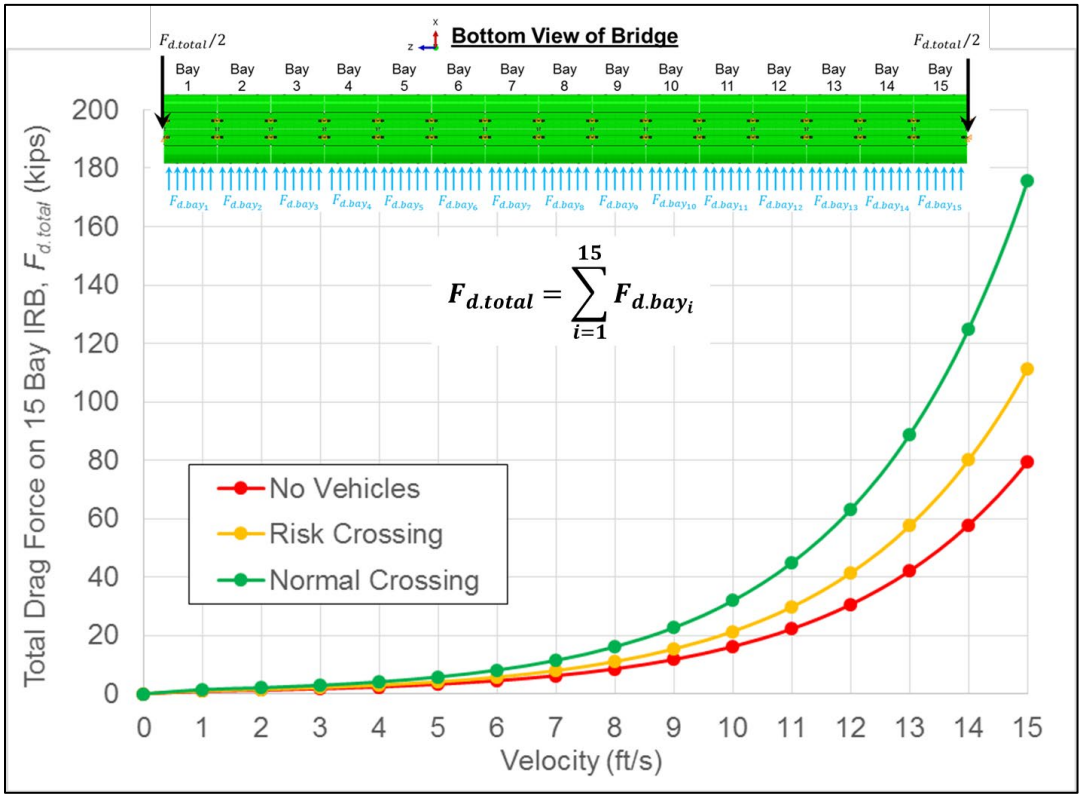
Figure 53 gives the total drag force on the 15-bay IRB as a function of current velocity for the three different vehicular loading cases. The total drag force on the entire bridge is the summation of the drag forces on the individual bays:

$$F_{d.total} = \sum_{i=1}^{n_{bays}} F_{d.bay_i} \quad (11)$$

with $n_{bays} = 15$.

Knowledge of the total drag force on the bridge is useful, as it can be used to evaluate anchorage requirements if the bridge is anchored only at each end. The load that an anchor on either end of the bridge must resist is $F_{d.total}/2$, where $F_{d.total}$ is obtained from the plot in Figure 53.

Figure 53. Total drag force on the 15-bay (110 m) IRB as a function of current velocity for the three vehicular loading cases.



4.2.3 Drag-induced displacement for the 15-bay IRB

In this section, the transverse displacements resulting from the drag forces on the 15-bay IRB are presented. Figure 54 shows representative contour plots of transverse displacement, δ_x, for the no-vehicles, risk crossing, and normal crossing. For the sake of comparison, the same velocity (v =11 ft/s) was used for all three cases.

Figure 54. Representative transverse displacement, δ_x, contour plots for the 15-bay (110 m) IRB for the three vehicular loading cases. Flow is in the $+x$ direction. For each vehicular loading case shown, v =11 ft/s, and the deformation scale is 5x.

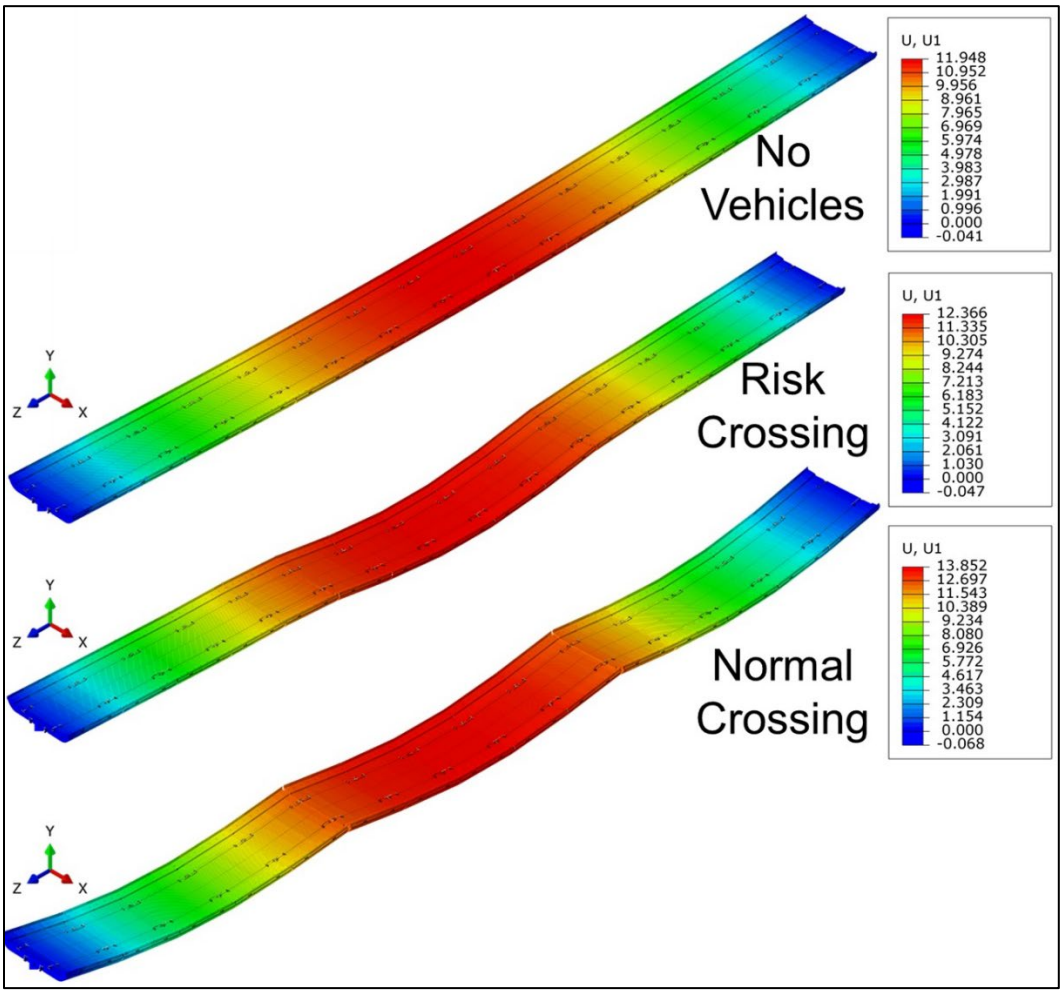


Figure 55 plots δ_x over the length of the 15-bay IRB for all of the simulations where $v > 0$ ft/s. A drastic increase in displacement is observed when $v > 11$ ft/s. This is due to the exponential increase in drag at higher velocities. For $v \leq 11$ ft/s, the effect of increased velocity seems to produce greater displacement compared to increased vehicular loading. This effect is more apparent in Figure 56, which shows plots of maximum transverse displacement, $\delta_{x.max}$, as a function of flow velocity for the three vehicular loading conditions. For $v \leq 11$ ft/s, the three curves lie more or less on top of each other; however, above 11 ft/s, the curves begin to deviate significantly.

Figure 55. Transverse displacement, δ_x, due to a range of flow velocities along the length of the 15-bay IRB for the three vehicular loading cases.

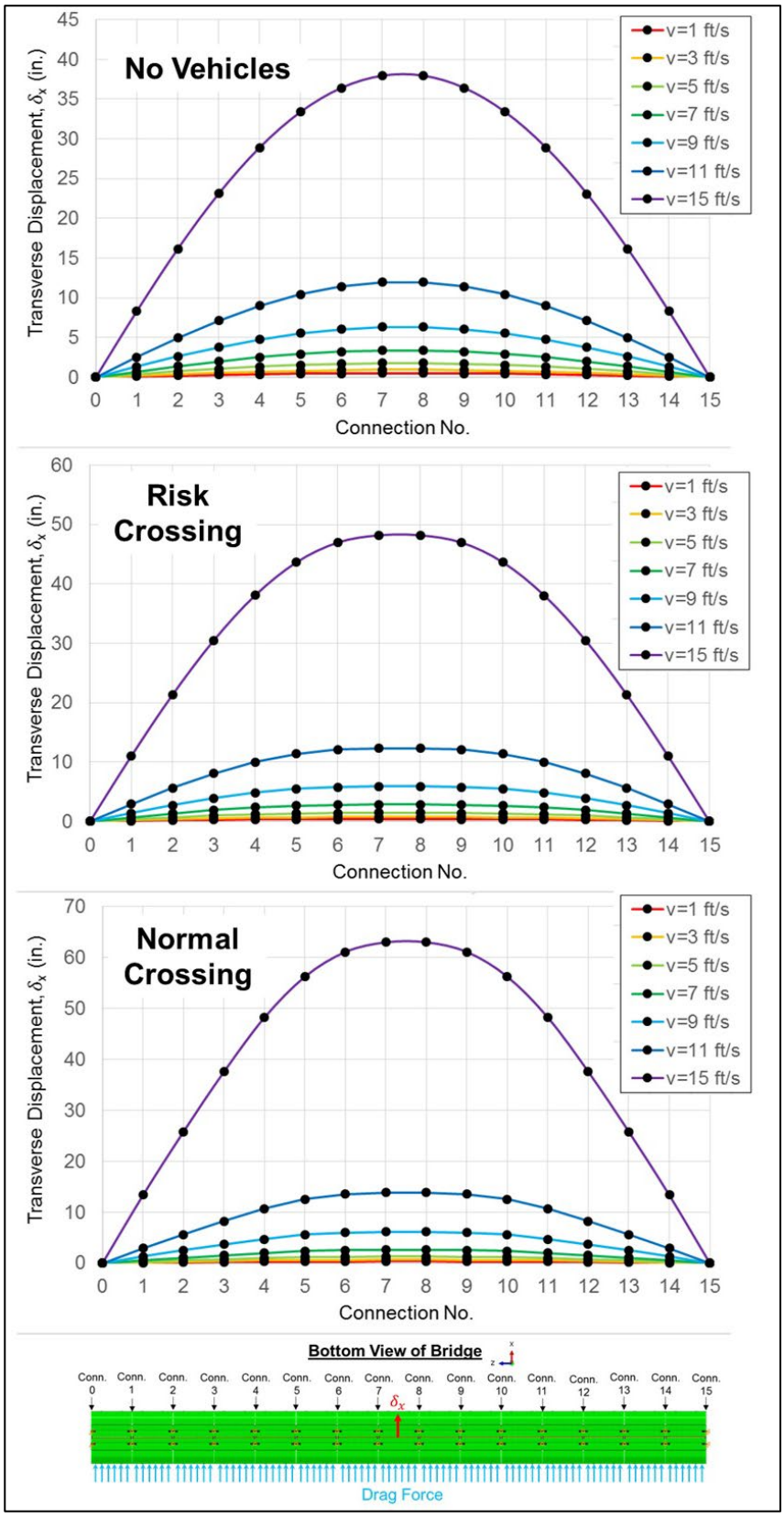
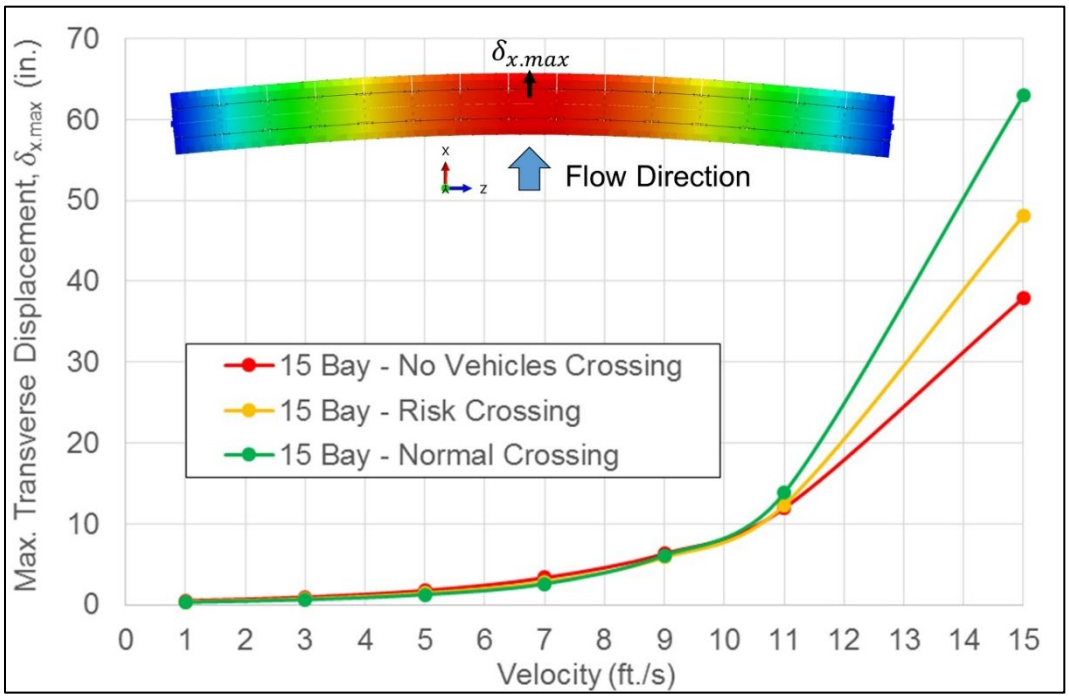


Figure 56. Maximum transverse displacement, $\delta_{x.max}$, as a function of flow velocity for the 15 bay IRB.



4.2.4 Limit states for the 15-bay IRB

4.2.4.1 Main coupling pins load analysis

In Section 4.1.3, the allowable force in the main coupling pin was determined to be $F_{\alpha.pin} = 250$ kips. In this section, there is an evaluation to determine under what circumstances the M&S pin connector forces exceed the allowable limit. To facilitate this evaluation, connector force output (Abaqus output variable "CTF") was requested for all of the main coupling connectors used to join IRB bays. Adjacent IRB bays are joined by two main couplings. To differentiate between the two connectors comprising each bay-to-bay joint, they are referred to as either *upstream* or *downstream*, depending on their location with respect to flow direction. Therefore, for a bridge composed of 15 bays, there will be 14 bay-to-bay joints, and at each joint there is an upstream connector and a downstream connector. There are also upstream and a downstream connectors on each end of the bridge, where a ramp bay would typically be connected. Therefore, there are 16 total upstream couplings and 16 total downstream couplings that were assigned a number starting with zero on one end of the bridge and ending with 15 on the opposite end.

Figure 57 shows the main coupling pin connector force output over a range of current velocities for the 110 m (15 bay) no-vehicles scenario. There are two plots (i.e., the plot on top shows the downstream connector force) and the bottom plot shows the upstream connector force along the length of the bridge. For reference, the allowable pin connector force, $F_{\alpha.pin} = 250$ kips, is also shown on each plot. A schematic is provided just below the plots identifying connector positions. The main coupling pin connector forces for the risk crossing and normal crossing are presented in a similar fashion in Figure 58 and Figure 59, respectively.

For each of the three vehicular loading scenarios, the largest forces are exerted on the downstream connectors; therefore, the limit states based on the main coupling pin are dictated by the downstream connectors. For the no-vehicles case (Figure 57), the connector forces remain below the 250-kip allowable until the current speed reaches 15 ft/s. At 15 ft/s, the downstream connectors numbered 3 – 12 exceed the allowable limit. Thus, the limit state for 110 m no-vehicles crossing is 11 ft/s.

For the risk crossing (Figure 58), where one 72-ton vehicle is assumed to be on the center of the bridge, the pin allowable was barely exceeded in downstream connectors 7 and 8 when the current velocity is 11 ft/s. For v = 11 ft/s, the pin force in downstream connectors 7 and 8 is 250.3 kips, just above the 250 kip allowable limit. Therefore, the maximum safe current speed for a risk crossing is 9 ft/s.

For the normal crossing (Figure 59) where three 72-ton vehicles are spaced approximately 100 ft apart on the bridge, the connector forces remain below the allowable for current velocities below 11 ft/s. Therefore, the maximum safe current speed for a normal crossing is also 9 ft/s, the same as the risk crossing scenario. For a normal crossing, more of the pins experience heavy loading compared to the risk crossing. However, due to the 100 ft spacing between vehicles, the loads are adequately distributed in such a way that the pins effectively experience load from only one of the vehicles at any given time.

Figure 57. Main coupling pin connector forces over a range of current velocities for the 110 m (15-bay) no-vehicles scenario.

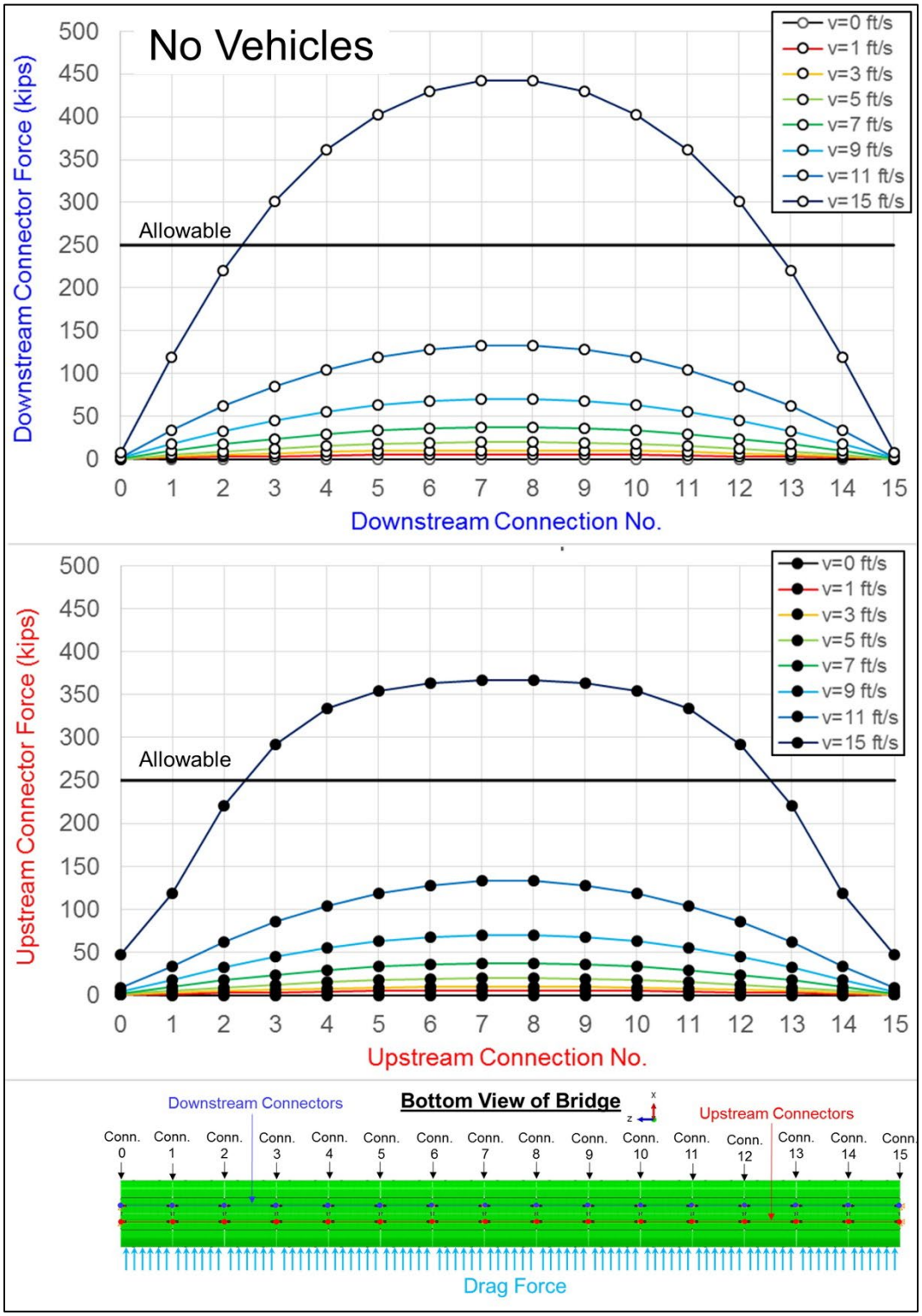


Figure 58. Main coupling pin connector forces over a range of current velocities for the 110 m (15-bay) risk-crossing scenario.

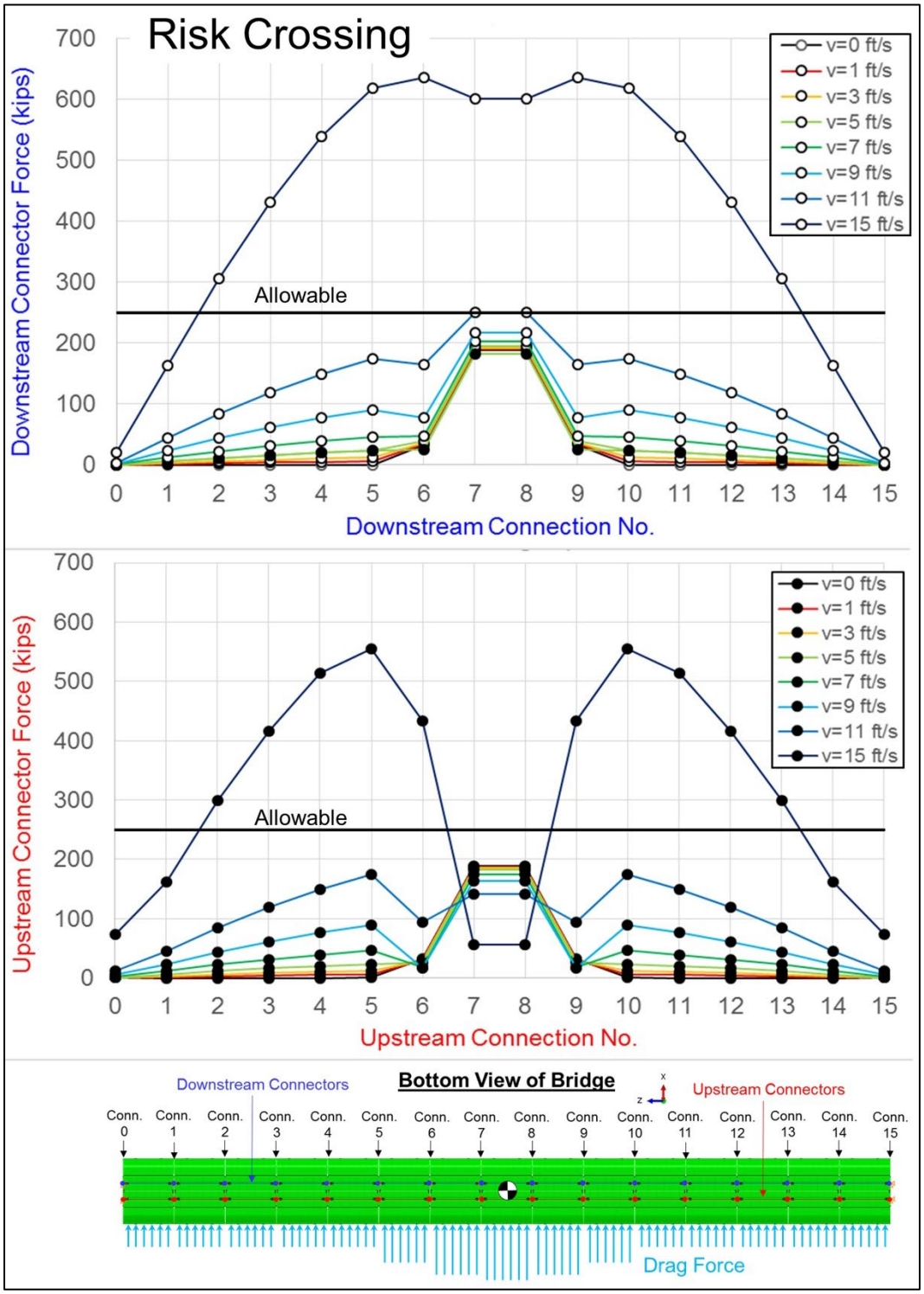
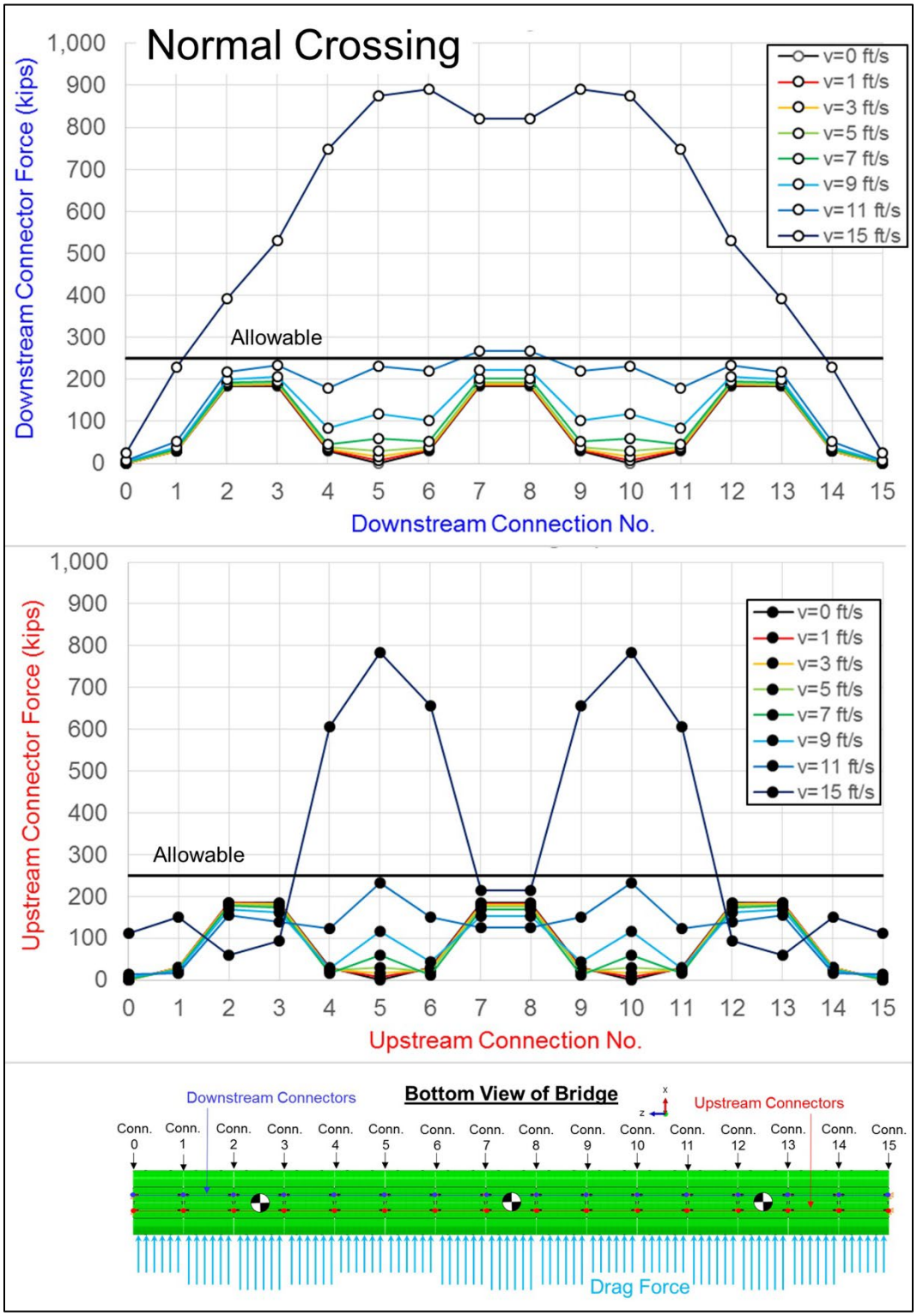


Figure 59. Main coupling pin connector forces over a range of current velocities for the 110 m (15-bay) normal-crossing scenario.



The limit states of the 110 m (15-bay) IRB are summarized in Table 11. These are the maximum current speeds that a 15-bay bridge can withstand before potential yielding occurs in the main coupling pins.

Table 11. Limit states for the 110 m (15-bay) IRB crossing types.

Crossing Type	Max. Current Speed
No Vehicles	11 ft/s
Risk Crossing (1x 72 ton vehicle)	9 ft/s
Normal Crossing (3x 72 ton vehicles)	9 ft/s

4.2.4.2 Aluminum IRB structure stress analysis

As discussed in Section 4.1.3, the allowable von Mises stress for the IRB aluminum components was found to be $\sigma_{\alpha.Al}$=24 ksi. In this section, there is verification that the von Mises stress in the aluminum does not exceed this allowable for the limit states given in Table 11.

Figure 60 shows contour plots of von Mises stress in the aluminum structure of the 15 bay IRB for the eight velocities simulated. In the image sequence, the velocity is increasing from top to bottom. Two views of the 15-bay bridge are provided for each velocity case. The sequence of images on the left show the bridge from above while the images on the right give a view of the underside of the bridge. Figure 61 and Figure 62 show similar image sequences for the risk crossing and normal crossing, respectively.

Figure 60. Contour plots of von Mises stress in the aluminum structure over a range of current velocities for the 110 m (15-bay) no vehicles crossing. The images on the left and right view the bridge from above and below, respectively. Flow is in the $+x$ direction.

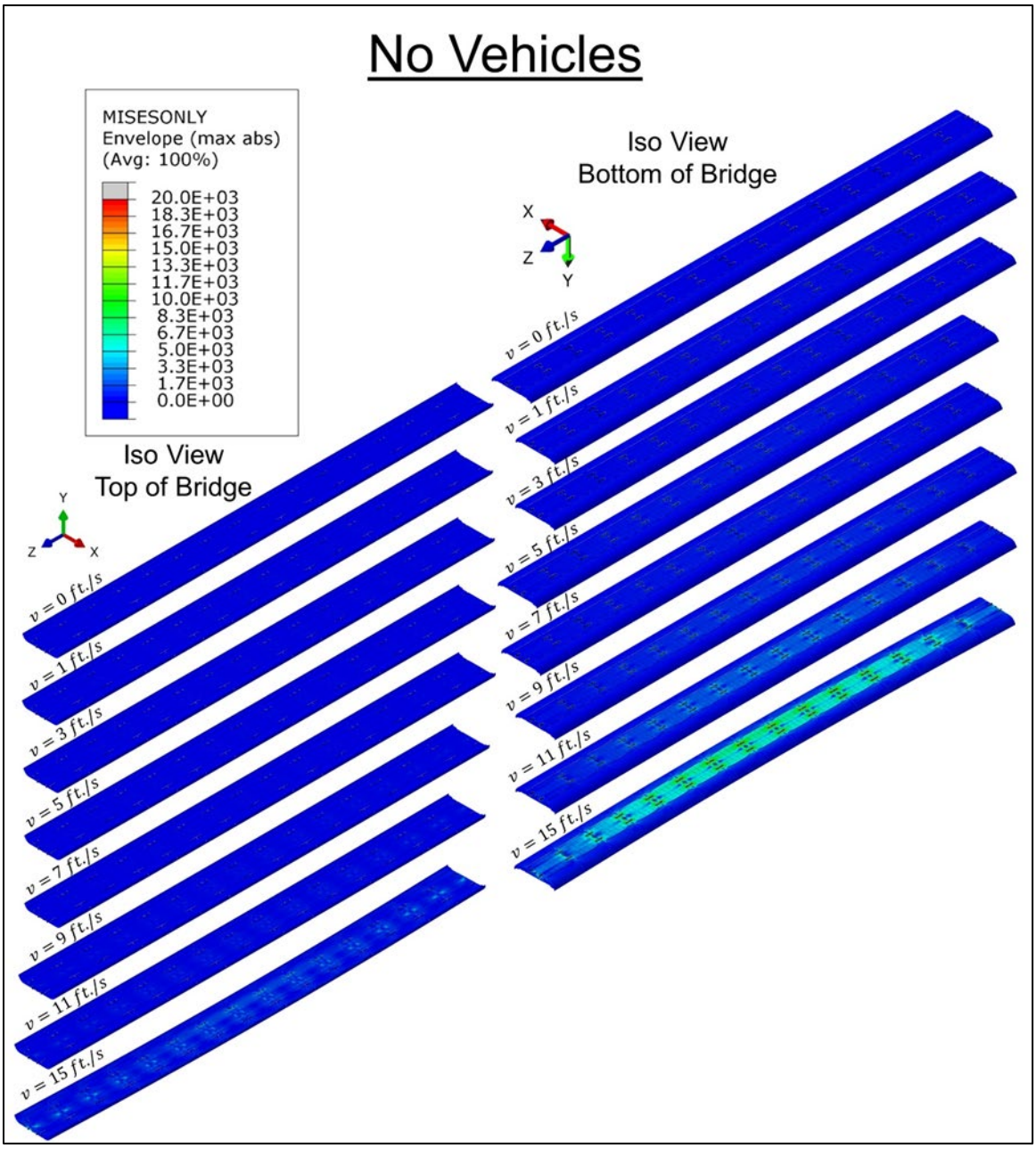


Figure 61. Contour plots of von Mises stress in the aluminum structure over a range of current velocities for the 110 m (15-bay) risk crossing. The images on the left and right view the bridge from above and below, respectively. Flow is in the $+x$ direction.

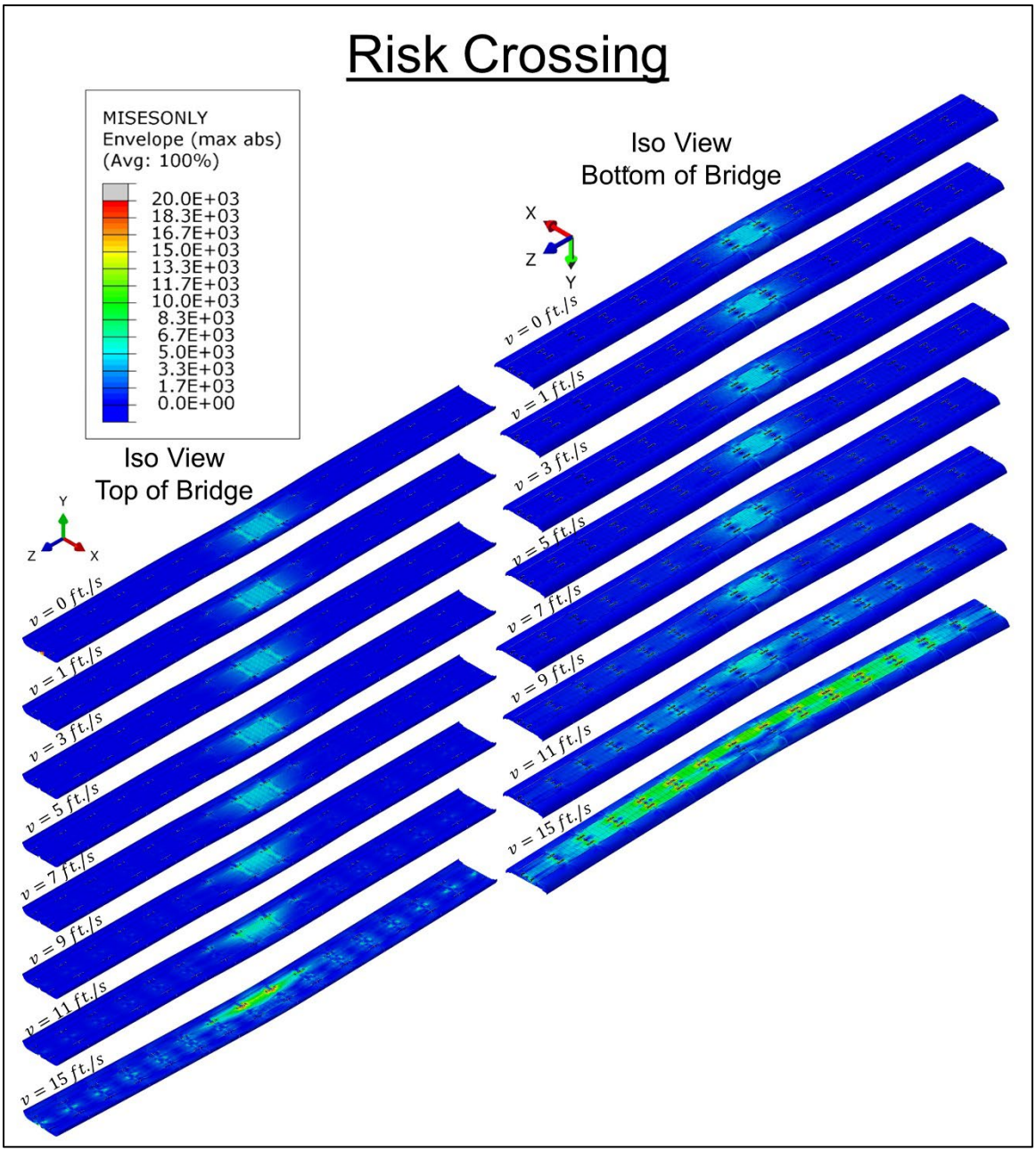
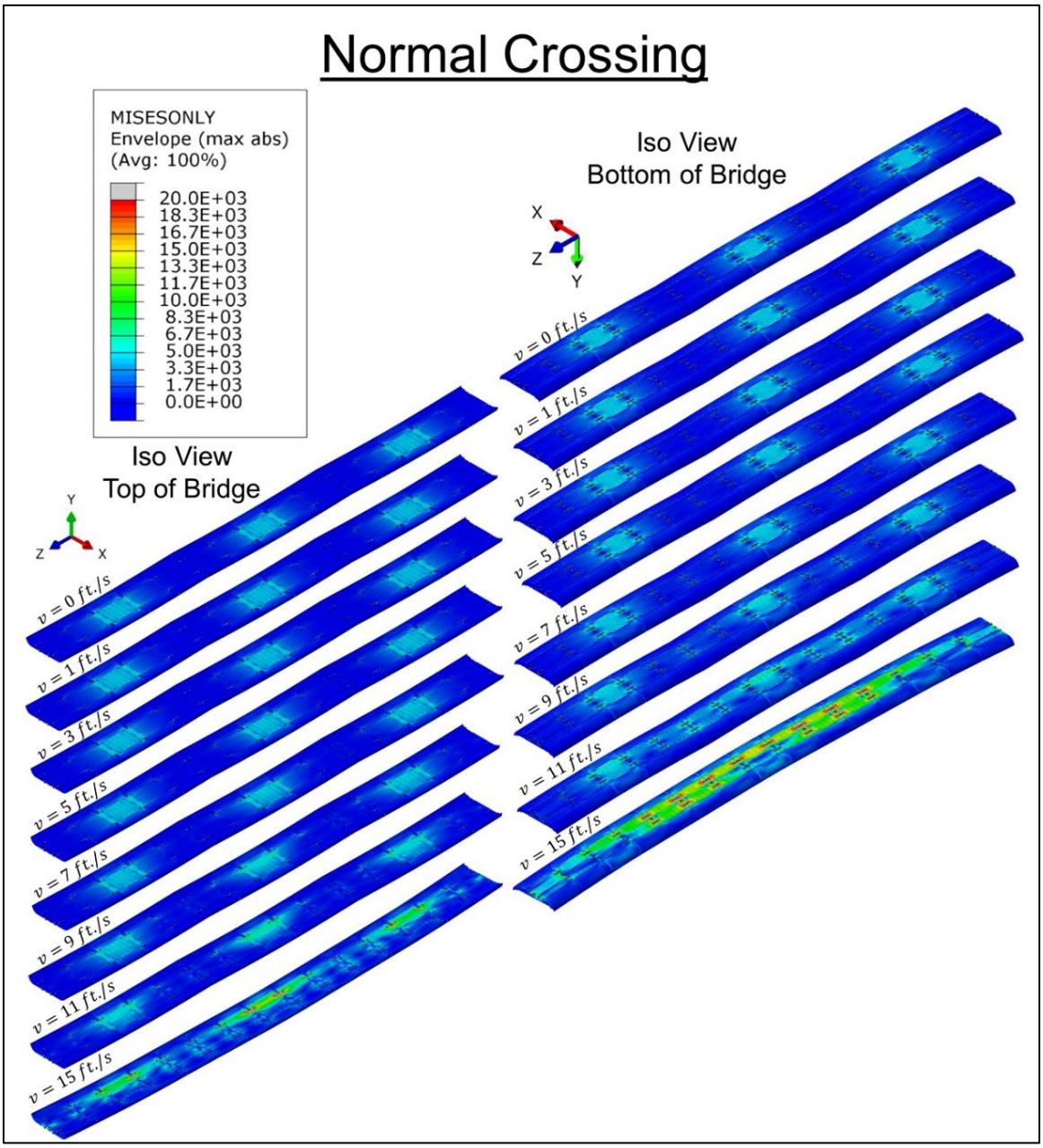


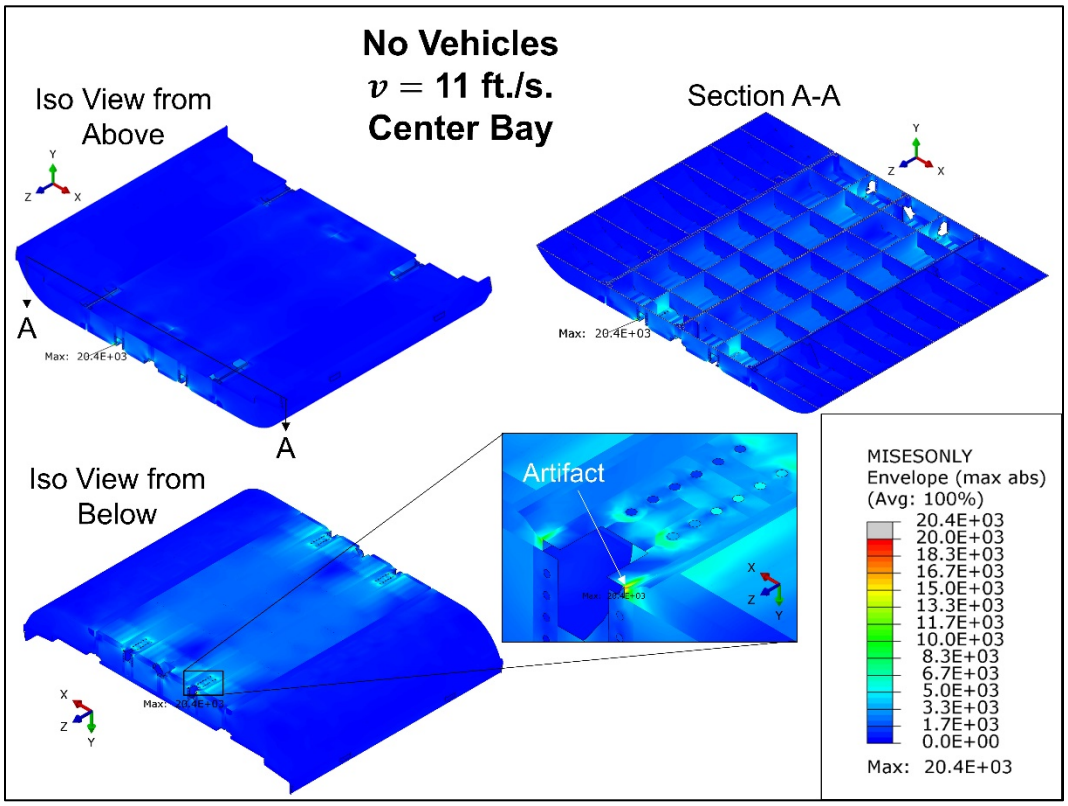
Figure 62. Contour plots of von Mises stress in the aluminum structure over a range of current velocities for the 110 m (15-bay) normal crossing. The images on the left and right view the bridge from above and below, respectively. Flow is in the $+x$ direction.



For each of the three vehicle loading cases, the bay in the center of the bridge experiences the highest stresses. Figure 63 shows the von Mises stress in the center bay for the no-vehicles crossing with a current velocity of 11 ft/s. This was the maximum current speed (determined in section 4.2.4.1) to not produce pin forces in excess of the allowable limit. As shown in Figure 63, a modeling artifact produced a highly localized peak stress of 20.4 ksi at a location on the bottom flange near the main coupling.

Nowhere in the aluminum structure does the stress exceed the 24 ksi allowable, including the location of the modeling artifact. Therefore, structural yielding of the aluminum is not a concerning failure mode.

Figure 63. Von Mises stress in the aluminum structure of the center bay for the 110 m (15-bay) no-vehicles, $v = 11$ ft/s scenario.



The von Mises stress in the aluminum structure of the center bay for the 15-bay risk crossing is shown in Figure 64 for the previously determined maximum safe current speed ($v = 9$ ft/s). The same modeling artifact caused a stress overage with magnitude 31.5 ksi. This was the only location in the entire aluminum structure of the 15-bay bridge where $\sigma_{vm} > \sigma_{\alpha.Al}$. Despite the local stress concentration caused by the artifact, yielding of the aluminum structure is not a concern for the risk-crossing scenario when current velocities are 9 ft/s or less.

Figure 65 is similar to Figure 64 but for the normal crossing. The stress magnitudes and distribution are similar to those in the risk-crossing analysis. As such, for this loading condition, yielding of the aluminum is not of concern for a normal crossing either.

Figure 64. Von Mises stress in the aluminum structure of the center bay for the 110 m (15-bay) risk-crossing, $v = 9$ ft/s scenario.

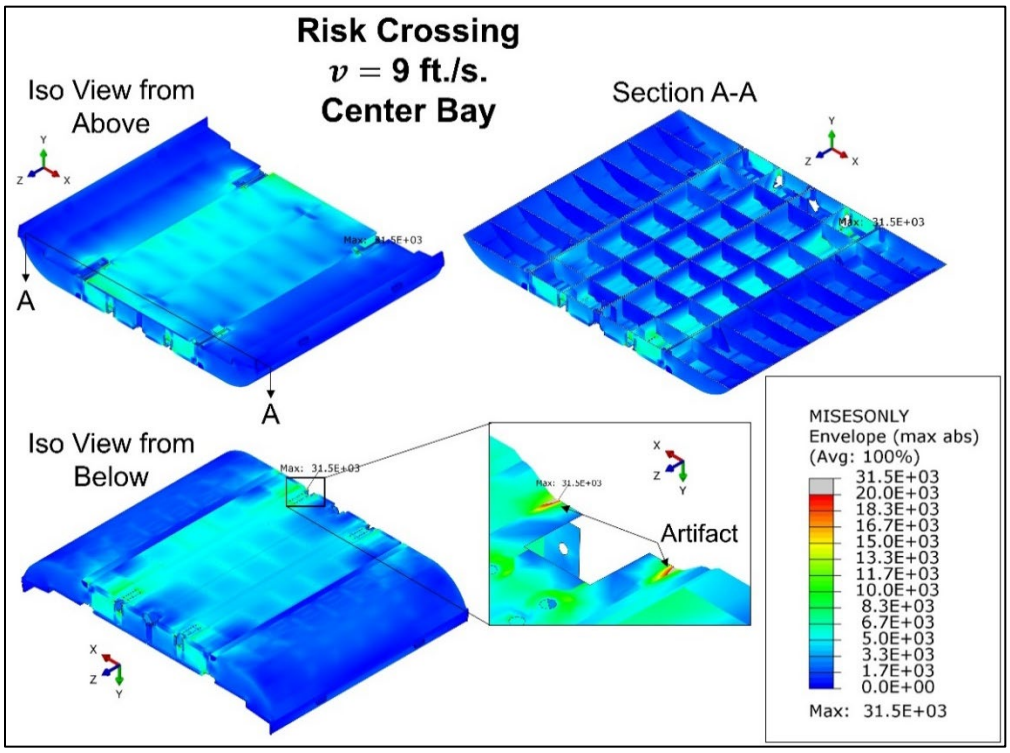
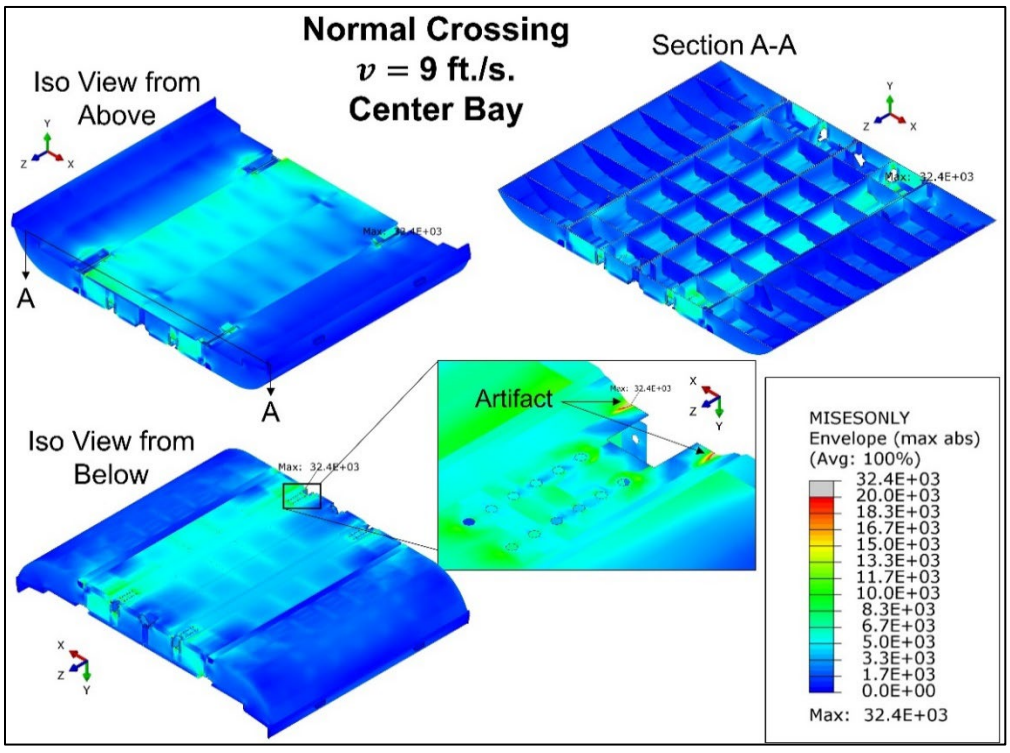


Figure 65. Von Mises stress in the aluminum structure of the center bay for the 110 m (15-bay) normal-crossing, $v = 9$ ft/s scenario.



4.2.4.3 Main coupling clevis/eye stress analysis

In Section 4.1.3, it was determined that the allowable von Mises stress for the steel IRB components is $\sigma_{\alpha.Stl}$ =121.5 ksi. In section 4.2.4.1, it was determined that the maximum safe current speeds for the three vehicular loading scenarios, based on the main coupling pin allowable. These limit states were provided in Table 11. In this section, the steel main couplings were examined to ensure the stress in these components does not exceed the allowable limit of $\sigma_{\alpha.Stl}$ =121.5 ksi.

The most highly stressed connection for all three vehicular load cases was downstream connector 7. Connectors 7 and 8 are the connectors on either end of the central bay (bay 8) in the 15-bay bridge. As such, these are the connectors nearest the mid-span of the bridge and would be expected to carry the largest load.

For the no-vehicles crossing, the maximum safe current speed was previously determined to be 11 ft/s. Figure 66 shows the von Mises stress in downstream connector 7 for 11 ft/s current velocity, with no vehicular loads on the IRB. The peak Mises stress is 50.5 ksi and is extremely localized. Thus, yielding in the main coupling is not a concern for the no-vehicles scenario.

Figure 66. (a) Isometric view with transparency and (b) isometric view from below showing von Mises stress in the most highly stressed main coupling (downstream connection 7) for the 110 m (15-bay) no-vehicles, v = 11 ft/s scenario.

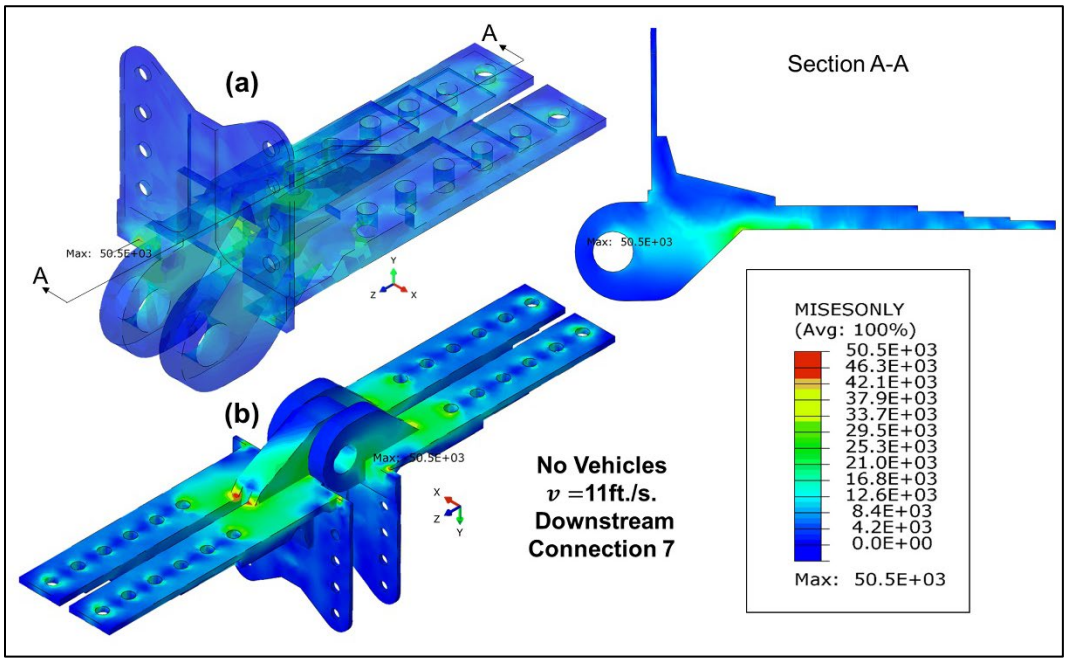


Figure 67 shows the shows the von Mises stress in downstream connector 7 for the risk crossing and a current velocity of 9 ft/s. The peak stress in the steel is 87.4 ksi and is highly localized. As seen in the section view, the average non-localized stress in the section is well below the 121.5 ksi allowable limit.

Figure 67. (a) Isometric view with transparency and (b) isometric view from below showing von Mises stress in the most highly stressed main coupling (downstream connection 7) for the 110 m (15-bay) risk-crossing, $v = 9$ ft/s scenario.

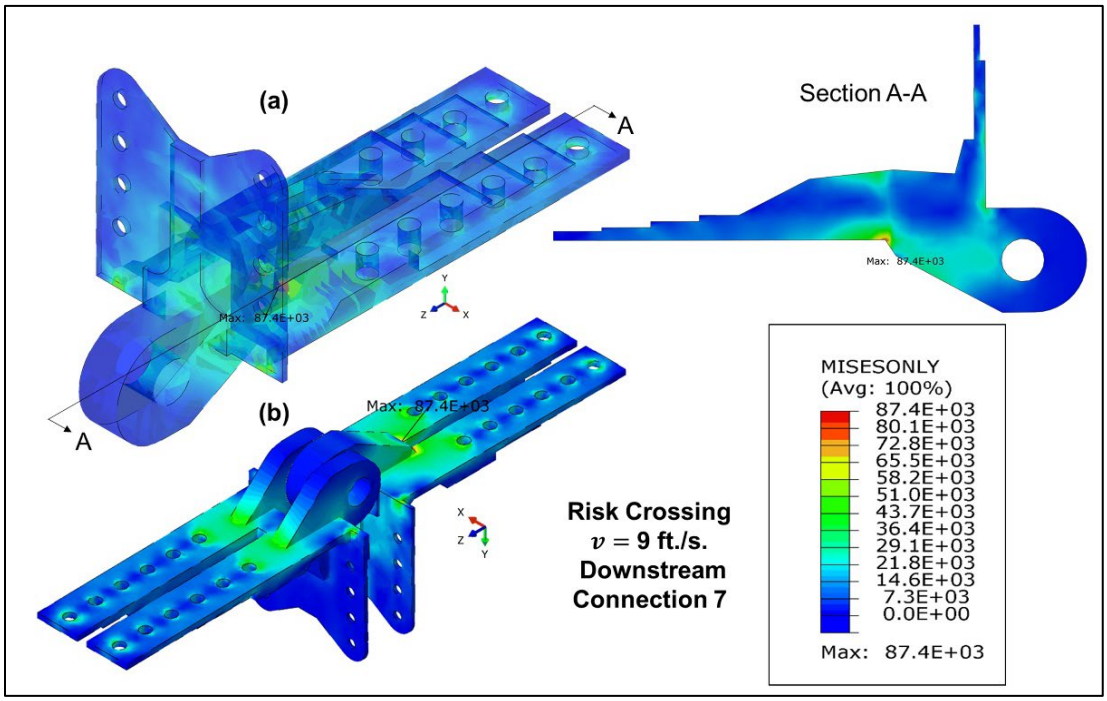
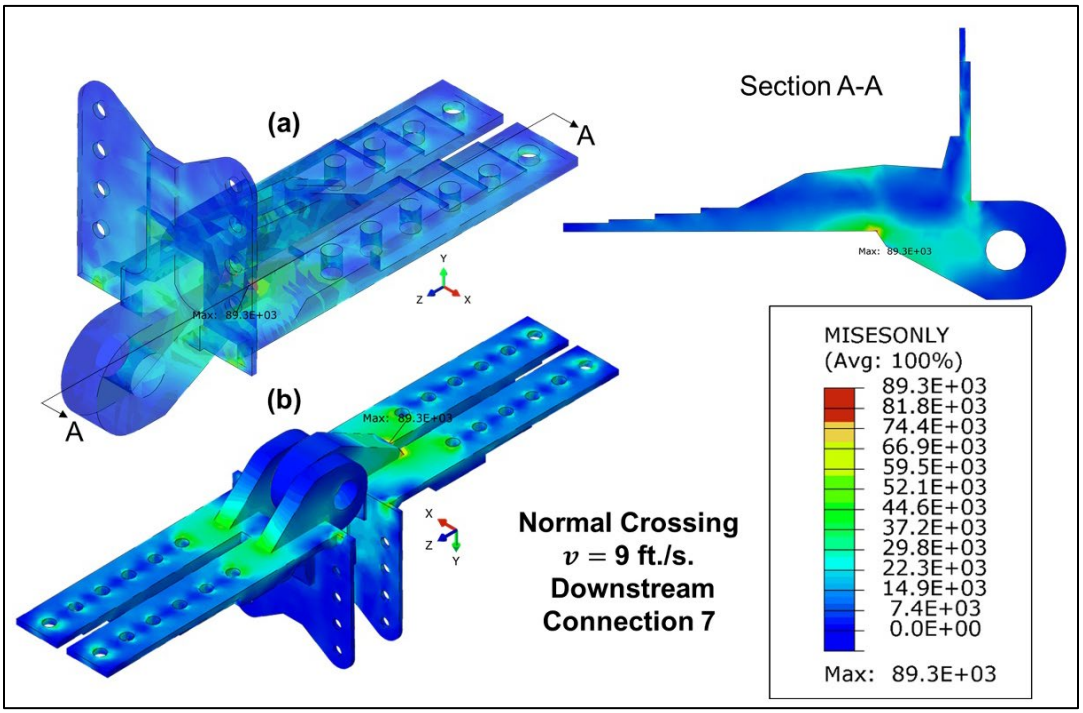


Figure 68 shows similar contours for the normal crossing. Here, the peak stress in the steel is 89.3 ksi, just slightly higher than for the risk crossing. Yielding of the main coupling is not a concern in either case. The peak stresses remain well below the allowable limit of $\sigma_{\alpha.Stl}$ =121.5 ksi.

Figure 68. (a) Isometric view with transparency and (b) isometric view from below showing von Mises stress in the most highly stressed main coupling (downstream connection 7) for the 110 m (15-bay) normal-crossing, $v = 9$ ft/s scenario.



In summary, the main coupling pins were found to be the weakest element in the IRB design. Under combined hydrodynamic and vehicular loading, failure is most likely to occur via yielding in the main coupling pin. M&S results indicate that stresses in both the aluminum structure and steel main coupling clevis/eye remain below allowable values at the onset of pin failure.

4.3 Structural analysis of the 30 bay (210 meter) IRB

In Section 4.2, it was determined that the maximum allowable current speeds for the three 110 m crossing conditions. For the 110 m no-vehicles case, $v_{max.110m.No\ Vehicles} = 11$ ft/s, and for the risk and normal crossings, $v_{max.110m.Risk} = v_{max.110m.Normal} = 9$ ft/s. These will be the maximum velocities considered for the 210 m crossing analyses since the loads on the longer bridge can only be higher compared to the shorter bridge.

Table 12 shows the simulation matrix for the 210 m (30-bay) IRB crossings. A total of 19 simulations were executed using the 30-bay IRB FEM.

Table 12. Simulation matrix for the 210 m (30-bay) IRB crossings.

Crossing Type	Current Speeds (ft/s)
No Vehicles	0, 1, 3, 5, 7, 9, 11
Risk Crossing (1x 72 ton vehicle)	0, 1, 3, 5, 7, 9
Normal Crossing (5x 72 ton vehicles)	0, 1, 3, 5, 7, 9

The subheadings under this section are organized in the same way as for the 15-bay analysis. Section 4.3.1 presents the draft results where no drag load was applied (v = 0 ft/s). The fluid drag loading results are given next in Section 4.3.2. The drag induced displacement results are in Section 4.3.3. Finally, the limit states for the 30-bay IRB are presented in Section 4.3.4.

4.3.1 Draft (vertical displacement) of the 30 bay IRB

Using the same procedure as before for 15 bays, there was application of nonstructural mass (representing the vehicular loads) and gravity loading only to the 30-bay IRB FEM. Figure 69 shows the draft response of the 30-bay bridge for the three vehicular loading cases analyzed (no vehicles, risk crossing, and normal crossing). Figure 70 plots the average draft of each bay along the length of the bridge.

An important difference between the 15- and 30-bay crossings is that a connection exists at the middle of the bridge for the 30-bay crossing whereas the midline of the 15-bay crossing fell on the center bay (bay #8). This symmetry difference, which arises for an even number of bays as opposed to an odd number of bays, influenced the nonstructural mass distribution for the 30-bay crossing. To maintain vehicular loading symmetry, the weight of each vehicle had to be distributed across the decks of two bays, unlike for the 15-bay crossing where the weight of each vehicle was placed on a single deck. For the normal crossing with one vehicle centered on the bridge and additional vehicles offset 100 ft in either direction, the 30-bay crossing had sufficient length for five vehicles to be on the bridge simultaneously. The length of the 15-bay normal crossing allowed for only three vehicles to be on the bridge. The maximum drafts (i.e., y-displacements) are similar to those found earlier for the 15-bay IRB as expected.

Figure 69. Contour plots for the three vehicular loading cases showing draft (*y*-displacement) of the 30-bay (210 m) IRB. Deformation scale = 5x.

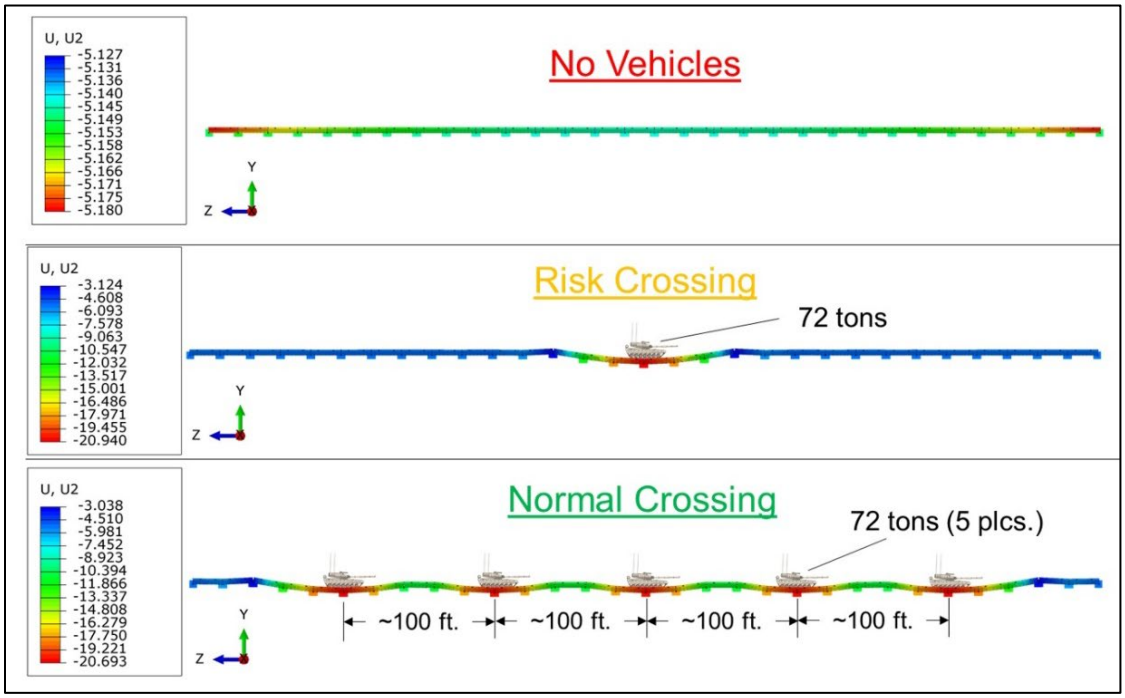
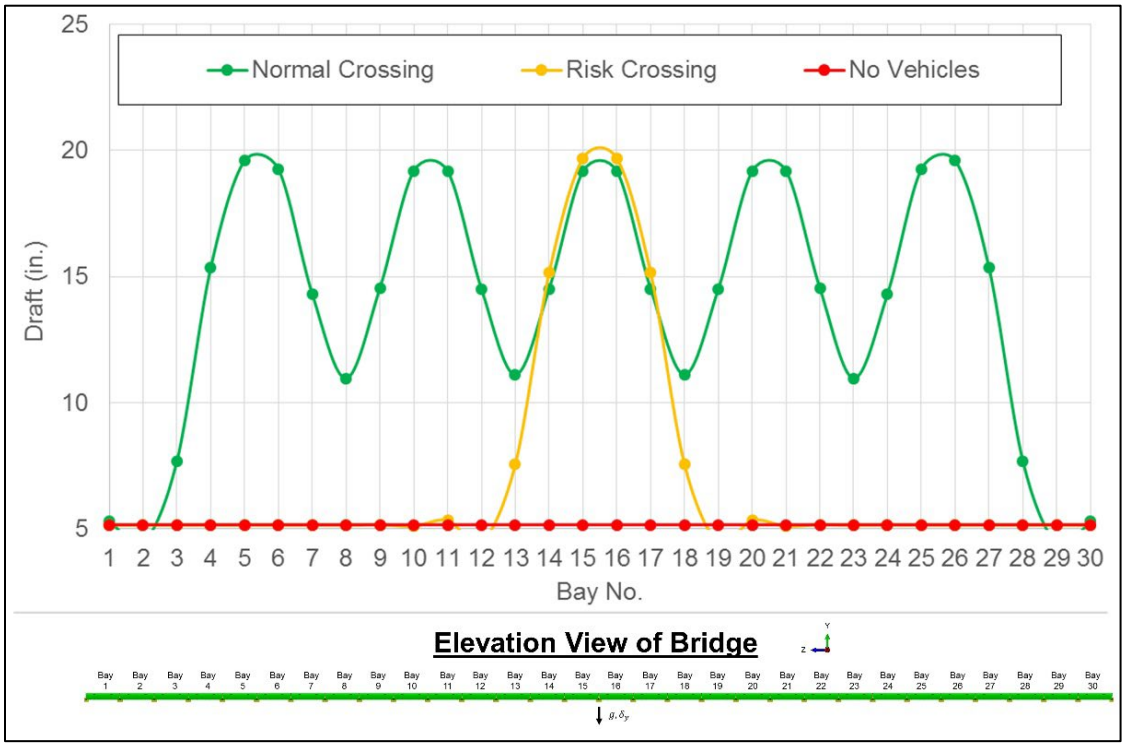


Figure 70. Draft (*y*-displacement) of the 30-bay (210 m) IRB for the three vehicular loading cases (no vehicles, risk crossing, and normal crossing).



With no vehicles on the bridge, the entire bridge drafts approximately 5.2 in. due to self-weight. This is the same draft as for the 15-bay IRB as would be expected. For the risk crossing, the 72-ton vehicle was centered between bays 15 and 16. This resulted in bays 13–18 drafting; however, the bays outside of this six-bay zone of influence were unaffected by the load. A maximum draft of approximately 20 in. was observed in bays 15 and 16. The bays adjacent to those (bay 14 and bay 17) displaced approximately 15 in., and bays 13 and 18 drafted by approximately 7.5 in. The remaining bays drafted approximately the same as in the no-vehicles case. For the normal crossing, vehicles were centered on bays 5–6, 10–11, 15–16, 20–21, and 25–26. All of these bays drafted approximately 20 in., similar to bays 15 and 16 for the risk crossing.

4.3.2 Drag loading on the 30 bay IRB

The draft of each bay (Figure 70) was substituted into Equation 7 to calculate the drag load on each bay over a range of current velocities ($v = 1$ - 11 ft/s). It was previously determined that the maximum allowable velocity for the 15-bay bridge was $v = 11$ ft/s. The loads and stresses on a longer bridge will be higher compared to a shorter bridge. Hence, there was no need to consider current velocities in excess of 11 ft/s.

The resulting drag force distribution along the length of the 30-bay IRB for the no-vehicles scenario is plotted in Figure 71. With no vehicular loading, the draft of the bridge is constant; therefore, the drag force on each bay is constant for a given current velocity. Figure 72 shows the drag force distribution for the risk crossing with one 72-ton vehicle on the center of the 30-bay IRB. Similarly, the drag force on each bay for the normal crossing scenario with five 72-ton vehicles spaced ~100 ft apart along the 30-bay IRB is plotted in Figure 73.

Figure 71. Drag force distribution along the 210 m (30-bay) IRB over a range of current velocities for the no-vehicles scenario.

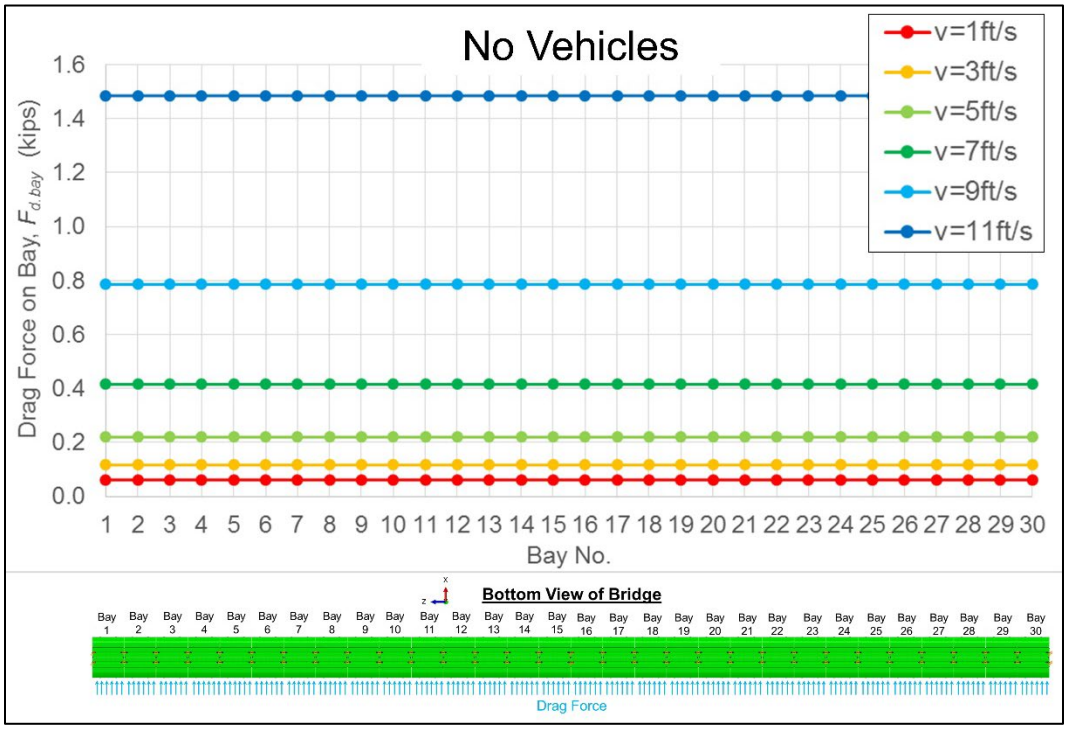


Figure 72. Drag force distribution along the 210 m (30-bay) IRB over a range of current velocities for the risk-crossing scenario.

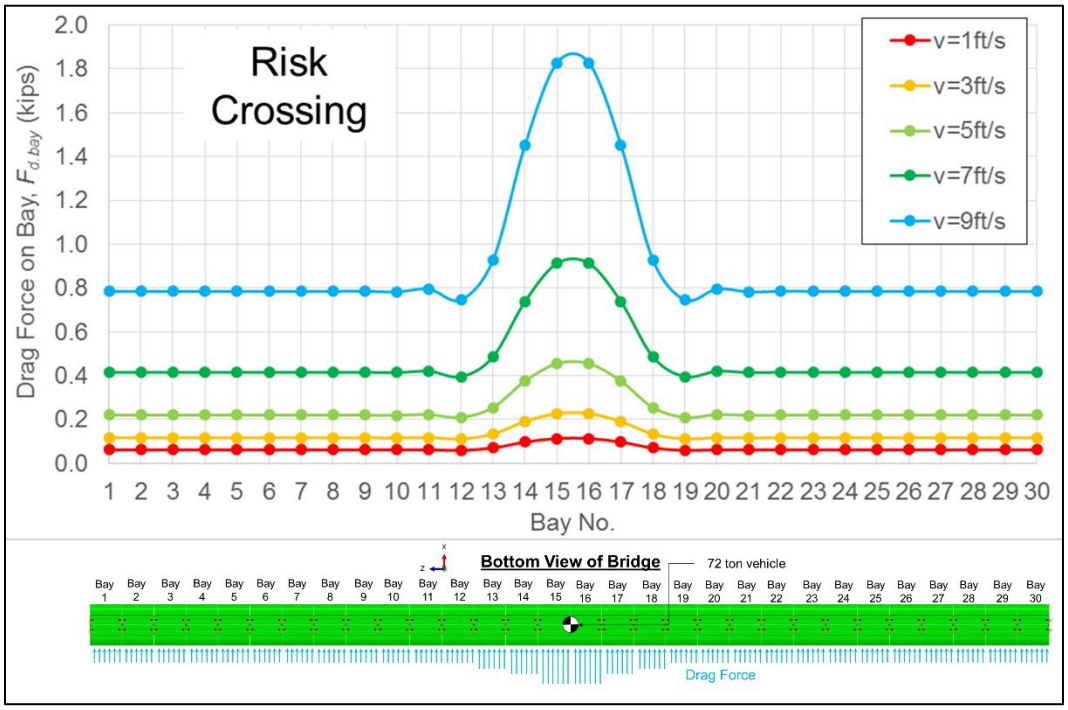
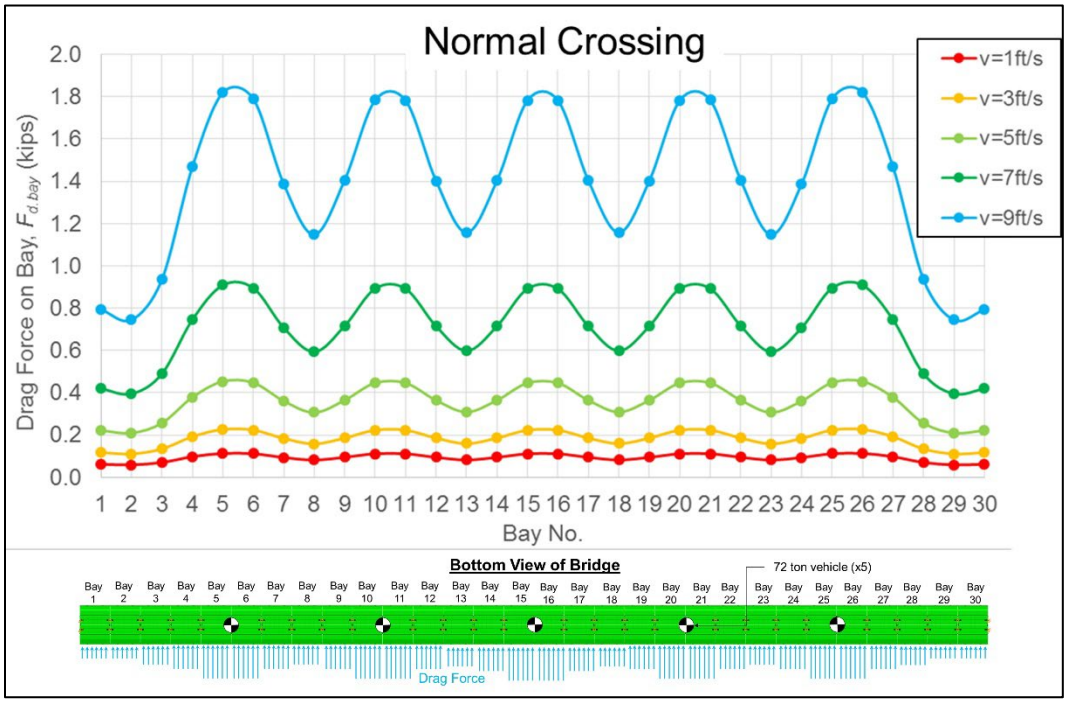
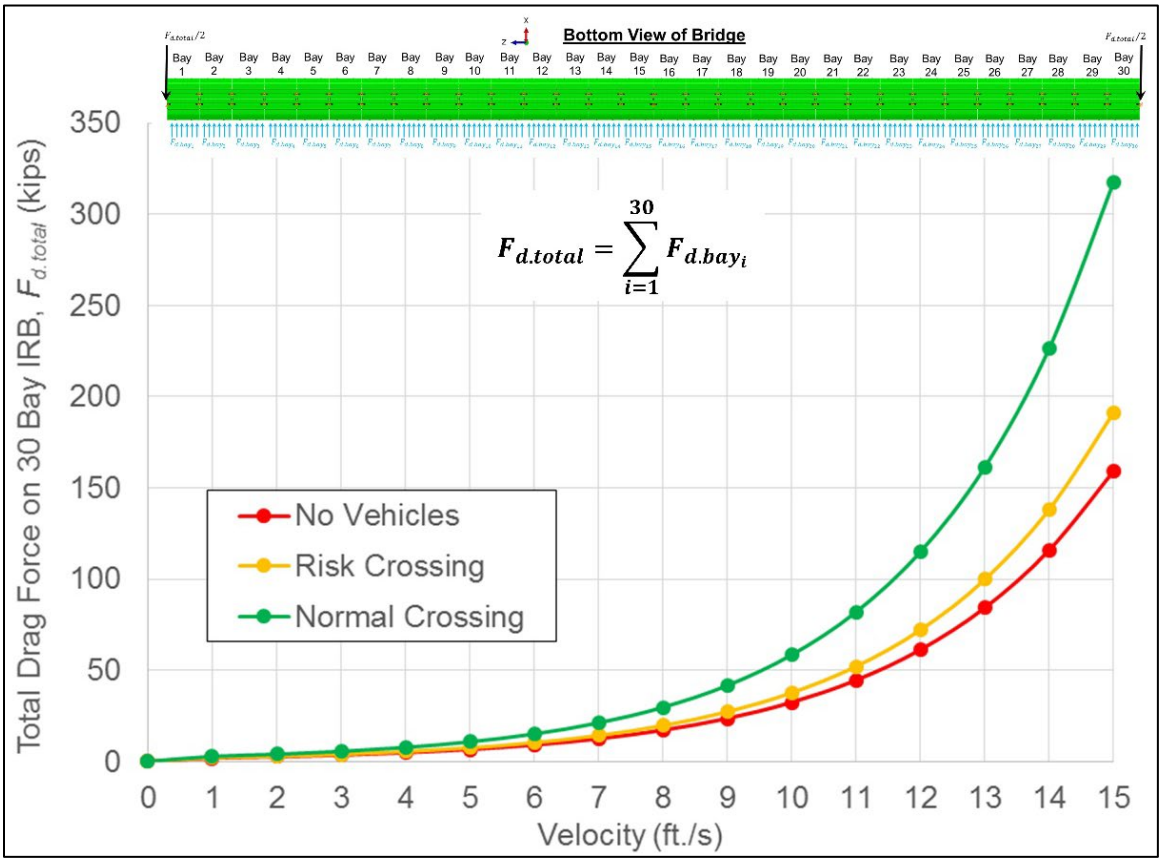


Figure 73. Drag force distribution along the 210 m (30-bay) IRB over a range of current velocities for the normal-crossing scenario.



The drag force on each bay was applied in the same way as previously done for the 110 m crossing, i.e., a distributed traction vector oriented in the $+x$ direction was applied to the bottom, wetted surface of each bay. The total drag force on the entire bridge is given by Equation 11 with $n_{bays} = 30$. Figure 74 plots the total drag force on the 210 m (30-bay) IRB as a function of current velocity for the three vehicular loading cases. Knowledge of the total drag force on the bridge is useful as it can be used to evaluate anchorage requirements if the bridge is anchored only at each end. The load that an anchor on either end of the bridge must resist is $F_{d.total}/2$. For example, the total drag force for the 210 m normal crossing with a 15 ft/s current is 320 kips (see Figure 74). Therefore, to anchor the bridge at the both ends, a resistive force of 160 kips would be required at each end.

Figure 74. Total drag force on the 210 meter (30 bay) IRB as a function of current velocity for the three vehicular loading cases.



4.3.3 Drag induced displacement for the 30-bay IRB

In this section, the transverse displacements resulting from the drag forces on the 210 m IRB are presented. Figure 75 shows representative contour plots of transverse displacement, δ_x, for the no-vehicles, risk-crossing, and normal-crossing scenarios. For the sake of comparison, the same velocity (v =9 ft/s) was used for all three cases.

Figure 75. Representative transverse displacement, δ_x, contour plots for the 210 m (30-bay) IRB for the three vehicular loading cases. Flow is in the $+x$ direction. For each vehicular loading case shown, v =9 ft/s and the deformation scale is 5x.

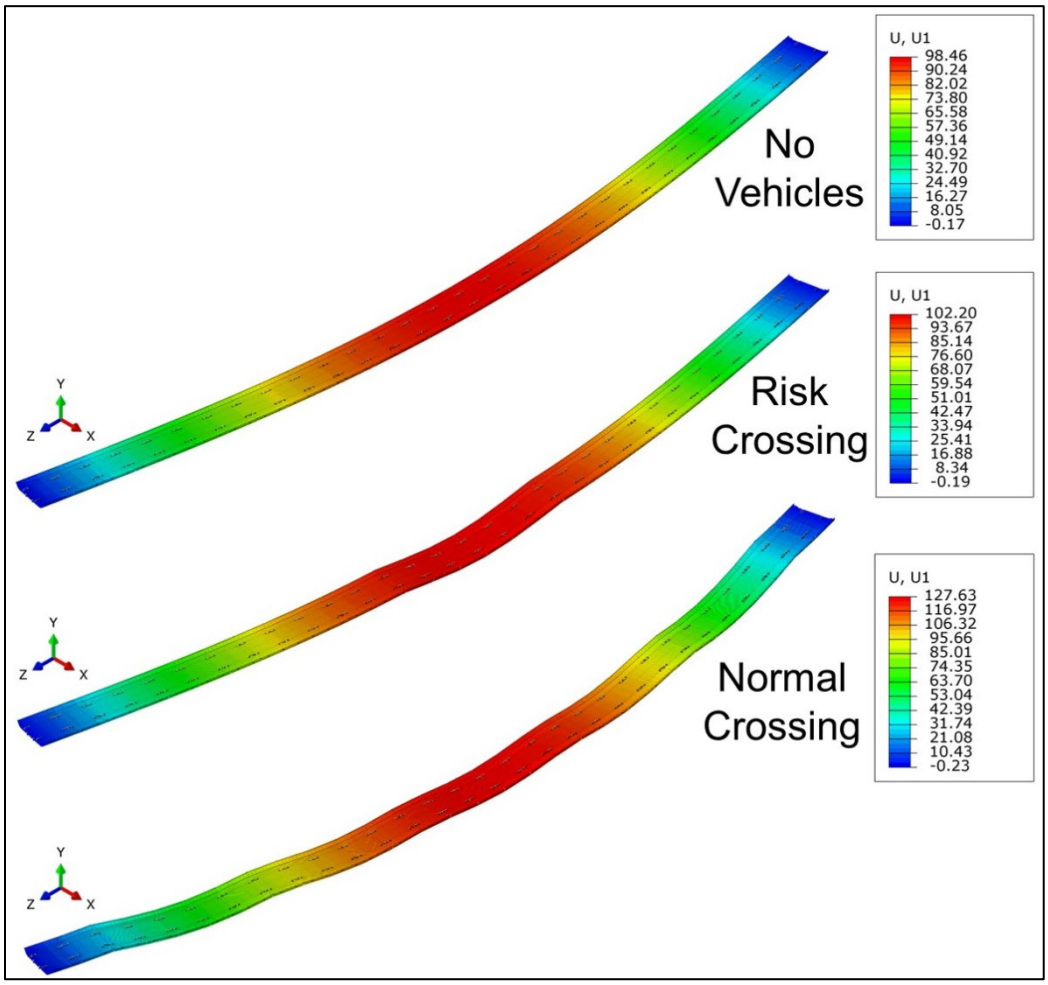


Figure 76 plots δ_x over the length of the bridge for all of the simulations executed where $v > 0$ ft/s. Recall that the maximum velocity considered for the 210 meter no-vehicles crossing was 11 ft/s, but the maximum velocity simulated for the risk and normal crossings was 9 ft/s. Therefore, the maximum velocity for which all three cases can be compared is 9 ft/s. Figure 77 plots the maximum transverse displacement, $\delta_{x.max}$, as a function of flow velocity for the three vehicular loading conditions.

Figure 76. Transverse displacement, δ_x, due to a range of flow velocities along the length of the 30-bay IRB for the three vehicular loading cases.

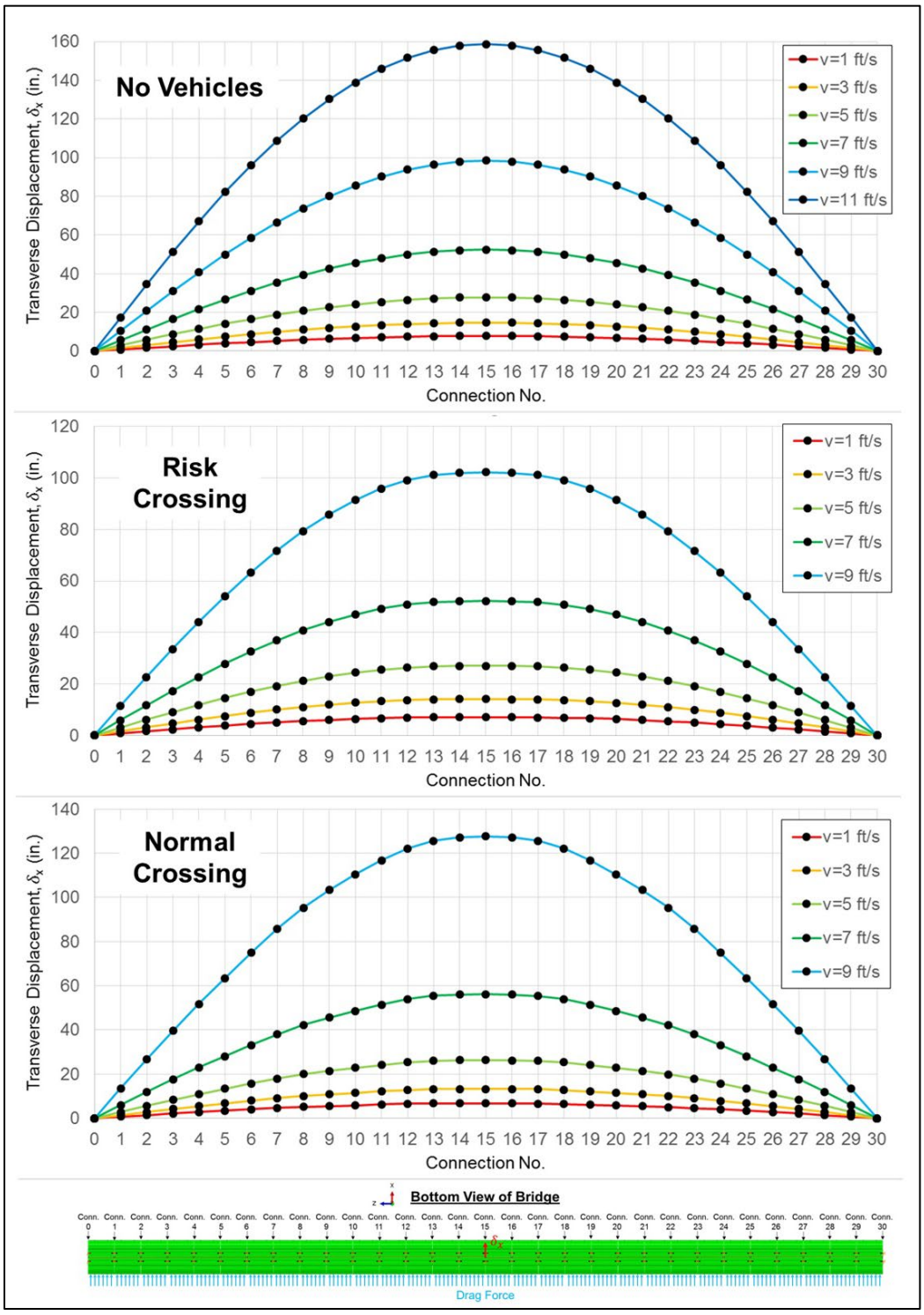
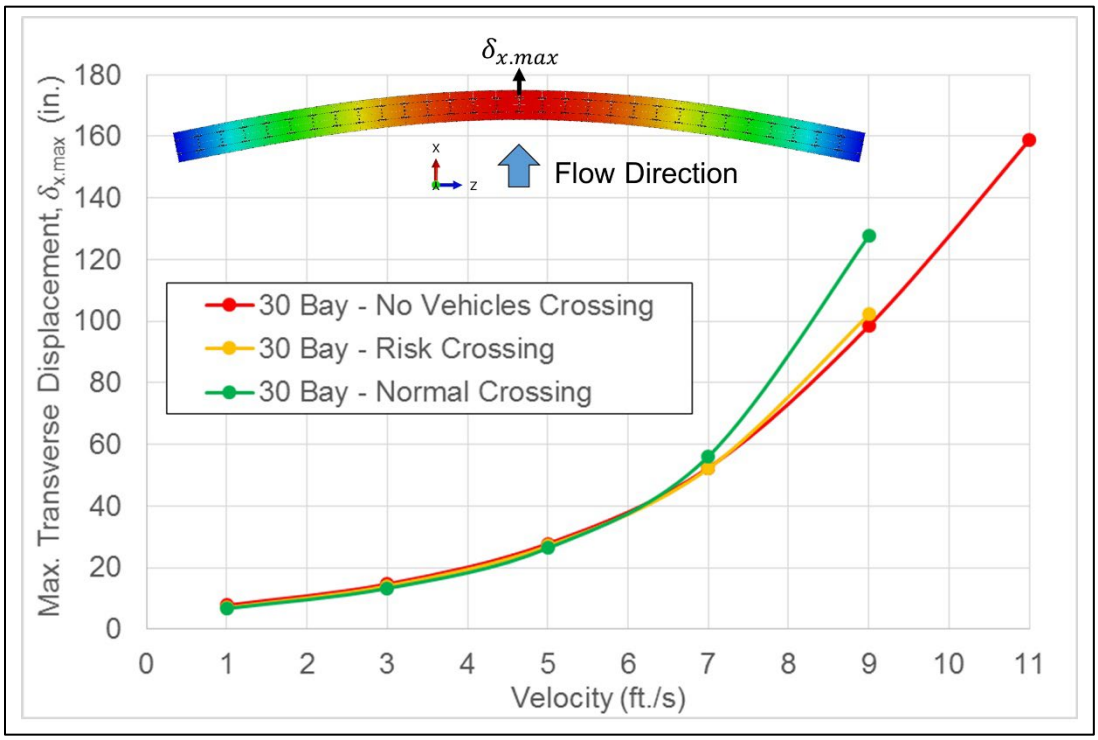


Figure 77. Maximum transverse displacement, $\delta_{x.max}$, as a function of flow velocity for the 30-bay IRB.



Here, it is seen again that there is an exponential increase in displacement as velocity increases. For $v \leq 7$ ft/s, the three curves more or less lie on top of each other; however, above 7 ft/s, the normal crossing begins to deviate from the other curves. The peak displacement for no vehicles and risk crossings show less deviation. This is because the influence of a single vehicle decreases as bridge length increases. The draft and resulting drag increase due to a single vehicle become less significant compared to the total drag on the bridge. This trend can also be observed in Figure 74 where the risk and no-vehicle crossings show less divergence for the 30-bay crossing compared the 15-bay crossing (see Figure 55).

4.3.4 Limit states for the 30-bay IRB

4.3.4.1 Main coupling pins load analysis

In Section 4.1.3, the allowable force in the main coupling pin used to connect IRB bays was determined to be $F_{\alpha.pin} = 250$ kips. In this section, there is an evaluation to determine under what circumstances the M&S pin connector forces (Abaqus output variable CTF) exceed the allowable limit. For the 30-bay IRB, there are 29 bay-to-bay joints, and at each joint there are an upstream connector and a downstream connector. There are also

upstream and downstream connectors on each end of the bridge where a ramp bay would typically be connected. Therefore, there are 31 total upstream couplings and 31 total downstream couplings, for which a number starting with zero on one end of the bridge and ending with 30 on the opposite end was assigned.

Figure 78 shows the downstream and upstream pin connector forces over the length of the 210 m (30-bay) IRB with no vehicular loading. Each curve corresponds to a different velocity ranging from 0 ft/s to 11 ft/s. The main coupling pin connector forces for the risk crossing and normal crossing are presented in a similar fashion in Figure 79 and Figure 80, respectively. However, for these cases, the maximum velocity simulated was 9 ft/s, based on the 15-bay crossing analysis results.

For the no-vehicles case (Figure 78), the maximum velocity that did not result in a connector force exceeding the 250 kip allowable is 7 ft/s. For v = 7 ft/s, a peak pin load of 148 kips occurs in connection 15. Thus, the limit state for 210 m no-vehicles crossing is 7 ft/s.

For the risk crossing (Figure 79) where one 72-ton vehicle is on the center of the bridge, 7 ft/s is again the maximum velocity that does not produce any pin load overages. For the risk crossing when v = 7 ft/s, downstream connector 15 experiences the highest load of 211 kips. Thus, the limit state for 210 m risk crossing is also 7 ft/s.

For the normal crossing (Figure 80) with five 72-ton vehicles spaced ~100 ft apart on the bridge, the pin allowable is barely exceeded in four connectors (12, 13, 17, and 18) when the current velocity is 7 ft/s. The maximum current speed that does not result in exceeding the allowable is 5 ft/s. For v = 5 ft/s, the highest load (206 kips) occurs in downstream connector 15. Therefore, the maximum safe current speed for a 210 m normal crossing is 5 ft/s.

An interesting phenomenon occurs at higher flow velocities when vehicles are on the bridge. The vehicle loads cause the decks of adjacent bays to compress together. Some of that force due to drag gets transferred through the deck contact surface, effectively bypassing the pin connection below. It was this phenomenon that resulted in larger loads in connectors 13 and 17, as opposed to connector 15, for the normal crossing with v =7 ft/s. The effect is also observed in the risk crossing for velocities above 5 ft/s.

Figure 78. Main coupling pin connector forces over a range of current velocities for the 210 m (30-bay) crossing with no vehicles on the IRB.

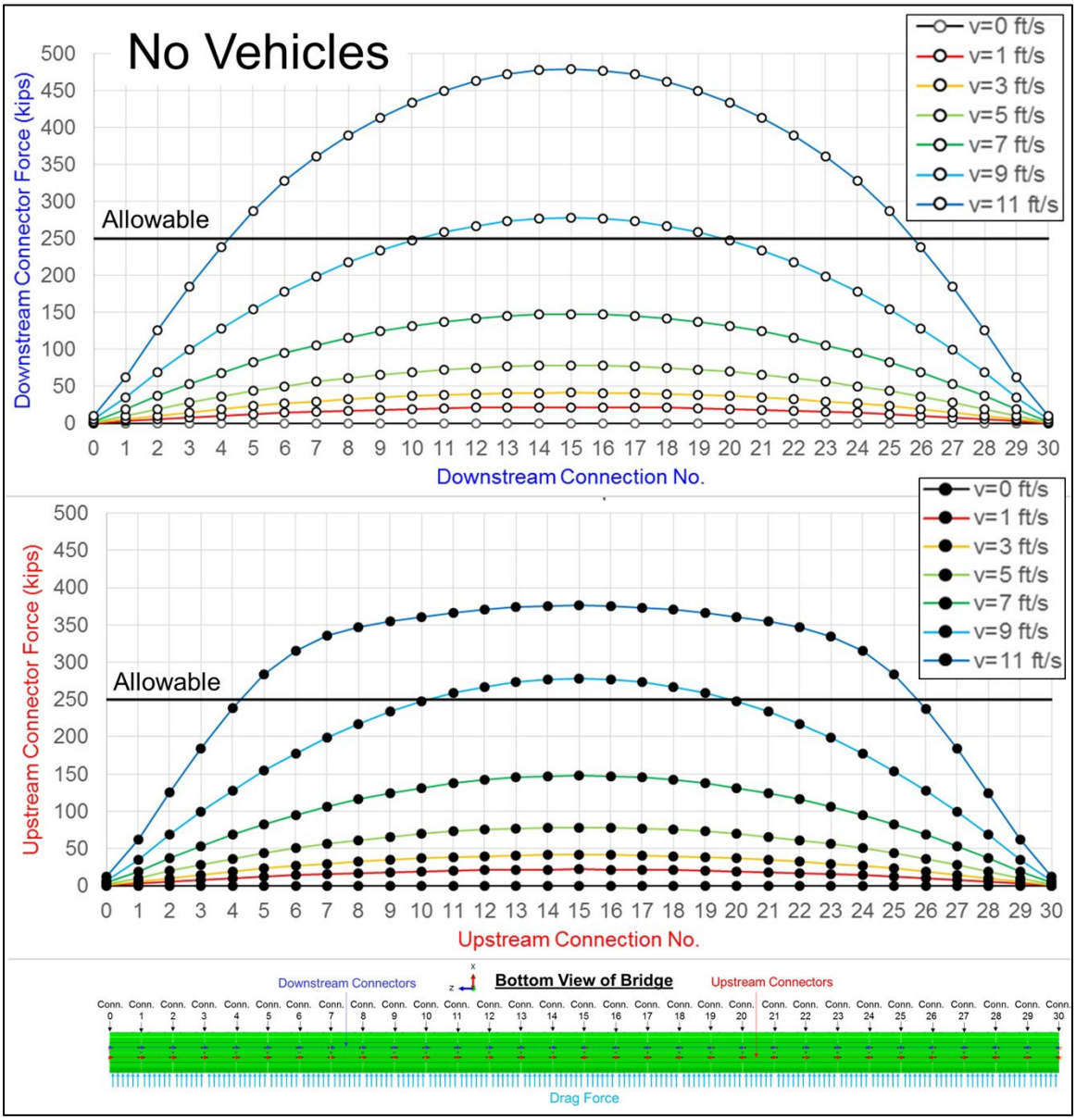


Figure 79. Main coupling pin connector forces over a range of current velocities for the 210 m (30-bay) risk crossing, with one 72-ton vehicle on the center of the IRB.

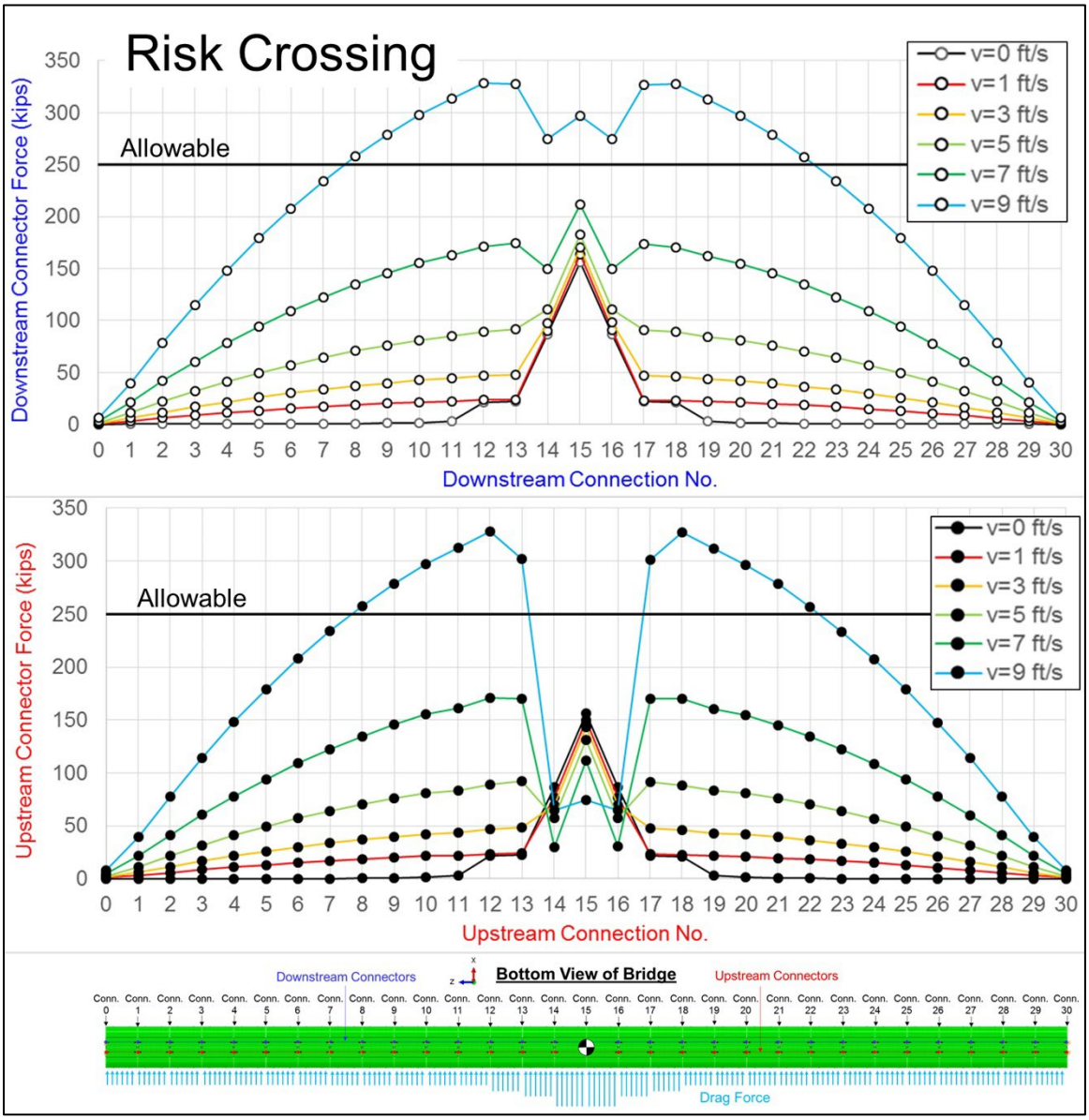
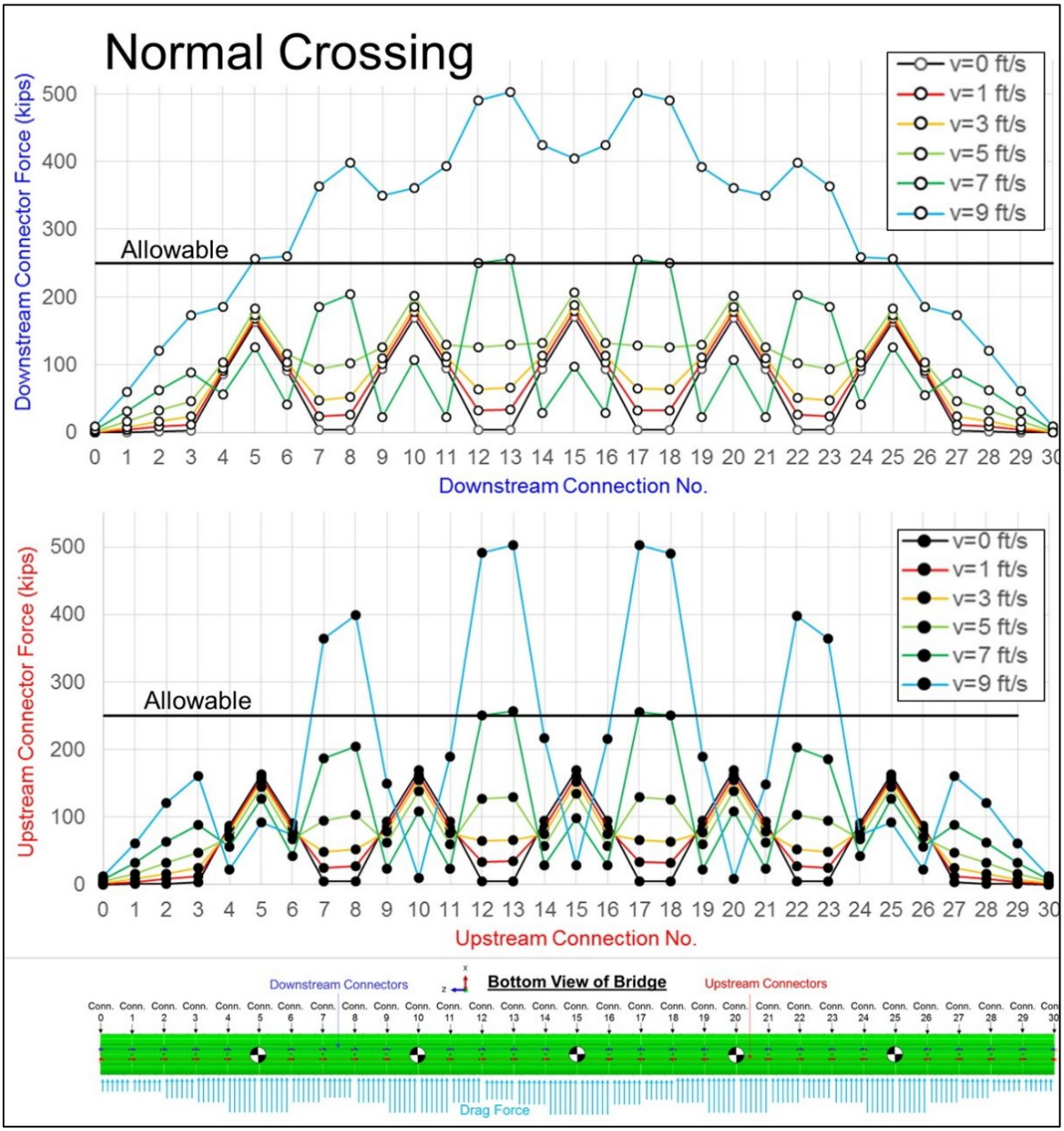


Figure 80. Main coupling pin connector forces over a range of current velocities for the 210 m (30-bay) normal crossing with five 72-ton vehicles on the IRB.



The limit states of the 210 m (30-bay) IRB are summarized in Table 13. These are the maximum current speeds that a 30-bay bridge can withstand before potential yielding occurs a main coupling pin.

Table 13. Limit states for the 210 m (30-bay) IRB crossing types.

Crossing Type	Max. Current Speed
No Vehicles	7 ft/s
Risk Crossing (1x 72 ton vehicle)	7 ft/s
Normal Crossing (5x 72 ton vehicles)	5 ft/s

4.3.4.2 Aluminum IRB structure stress analysis

In Section 4.1.3, the allowable von Mises stress for the IRB aluminum components was found to be $\sigma_{\alpha.Al}$=24 ksi. In this section, there is verification that the von Mises stress in the aluminum does not exceed this allowable for the limit states given in Table 13 for the 210 m IRB.

Figure 81 shows von Mises stress contour plots of the aluminum structure of the 15-bay IRB for the eight velocities simulated. In the image sequence, the velocity is increasing from top to bottom (from $v = 0$ ft/s to $v =$ 11 ft/s). Two views of the 30-bay bridge are provided. The sequence of images on the left show the bridge from above while the images on the right give a view of the underside of the bridge. Figure 82 and Figure 83 show similar image sequences for the risk crossing and normal crossing, respectively. As previously discussed, the maximum velocity analyzed for the 210 m risk and normal crossings was 9 ft/s.

Figure 81. Contour plots of von Mises stress in the aluminum structure over a range of current velocities for the 210 m (30-bay) no-vehicles crossing. The images on the left and right view the bridge from above and below, respectively. Flow is in the $+x$ direction.

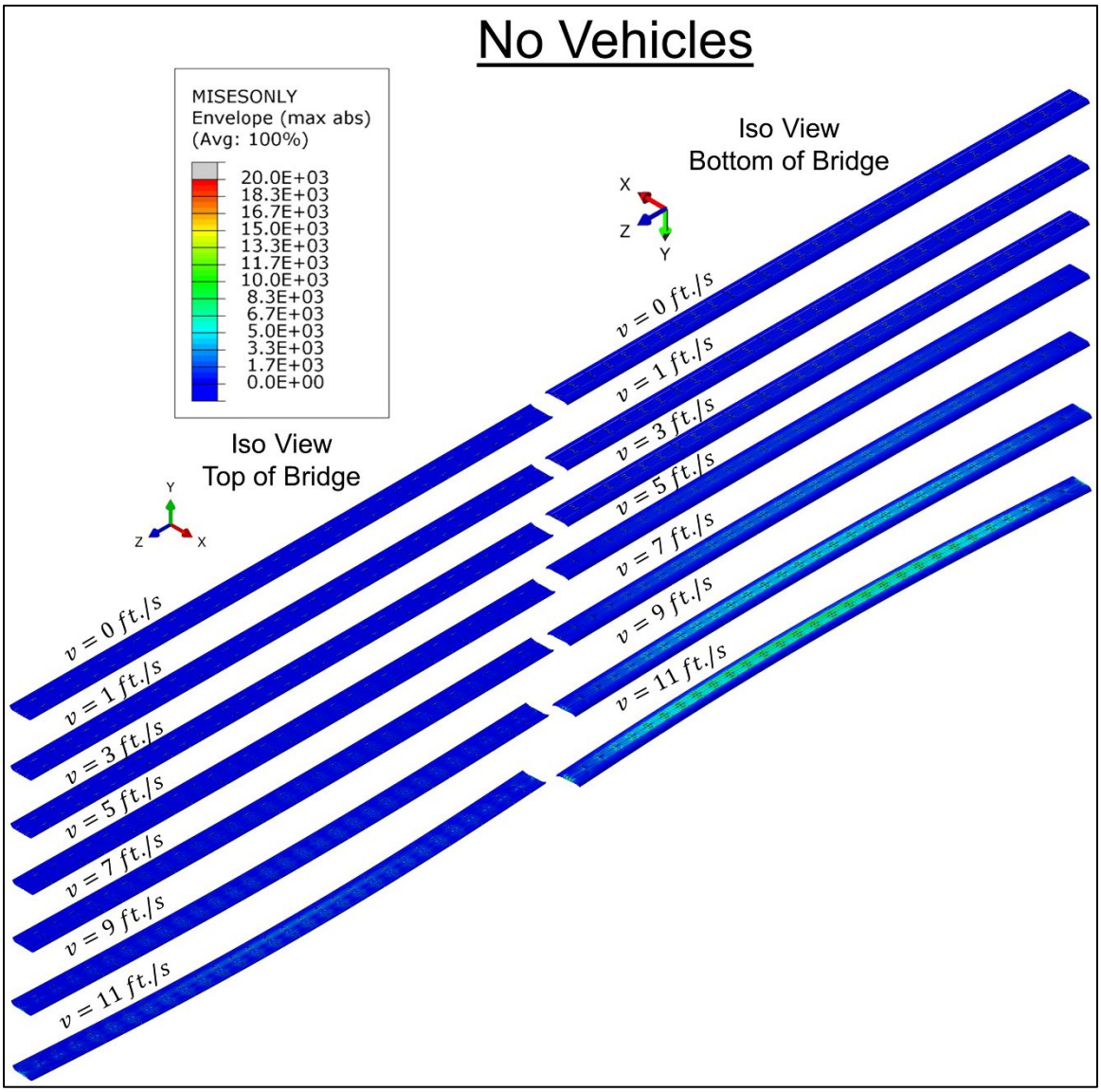


Figure 82. Contour plots of von Mises stress in the aluminum structure over a range of current velocities for the 210 m (30-bay) risk crossing. The images on the left and right view the bridge from above and below, respectively. Flow is in the $+x$ direction.

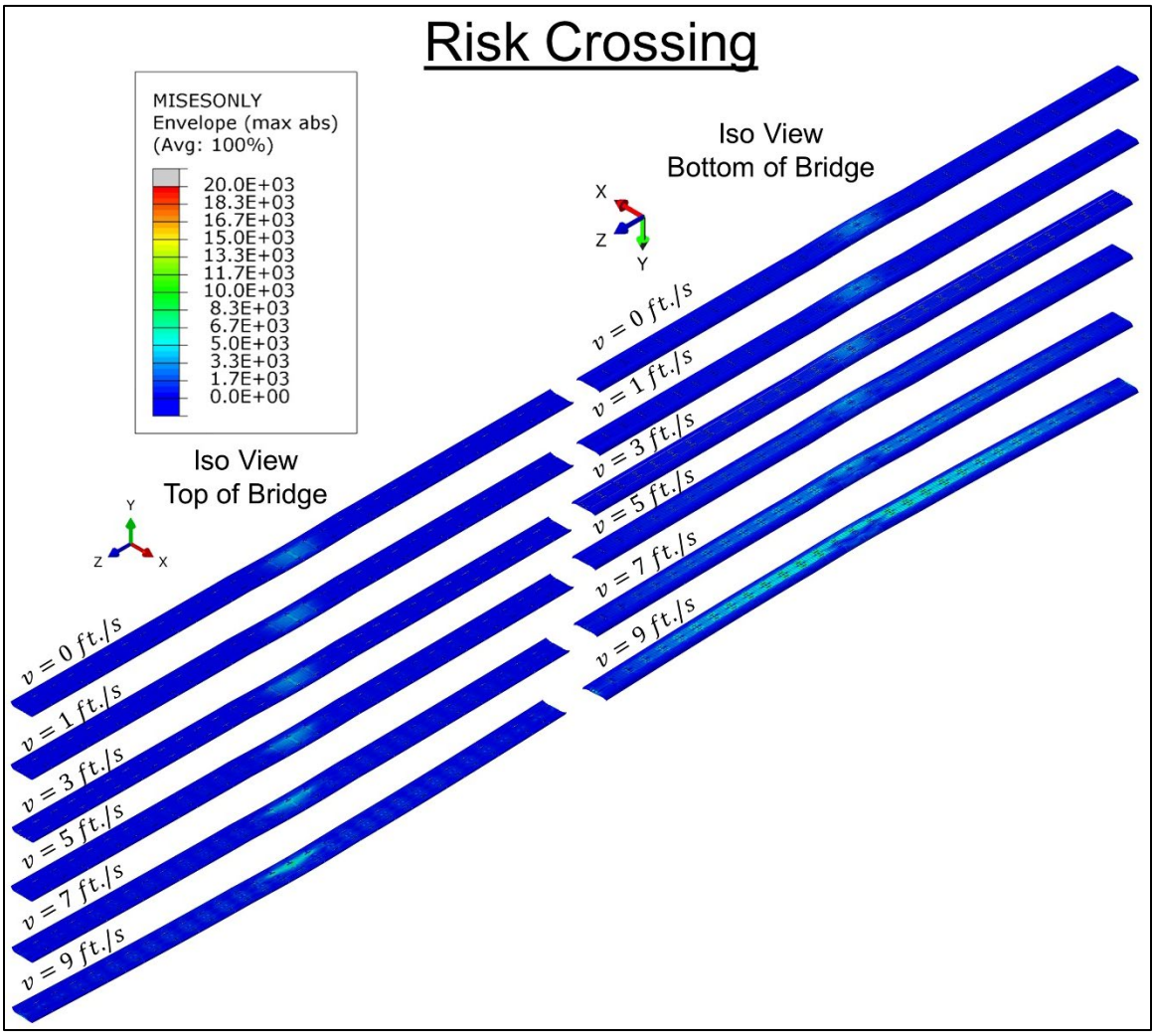
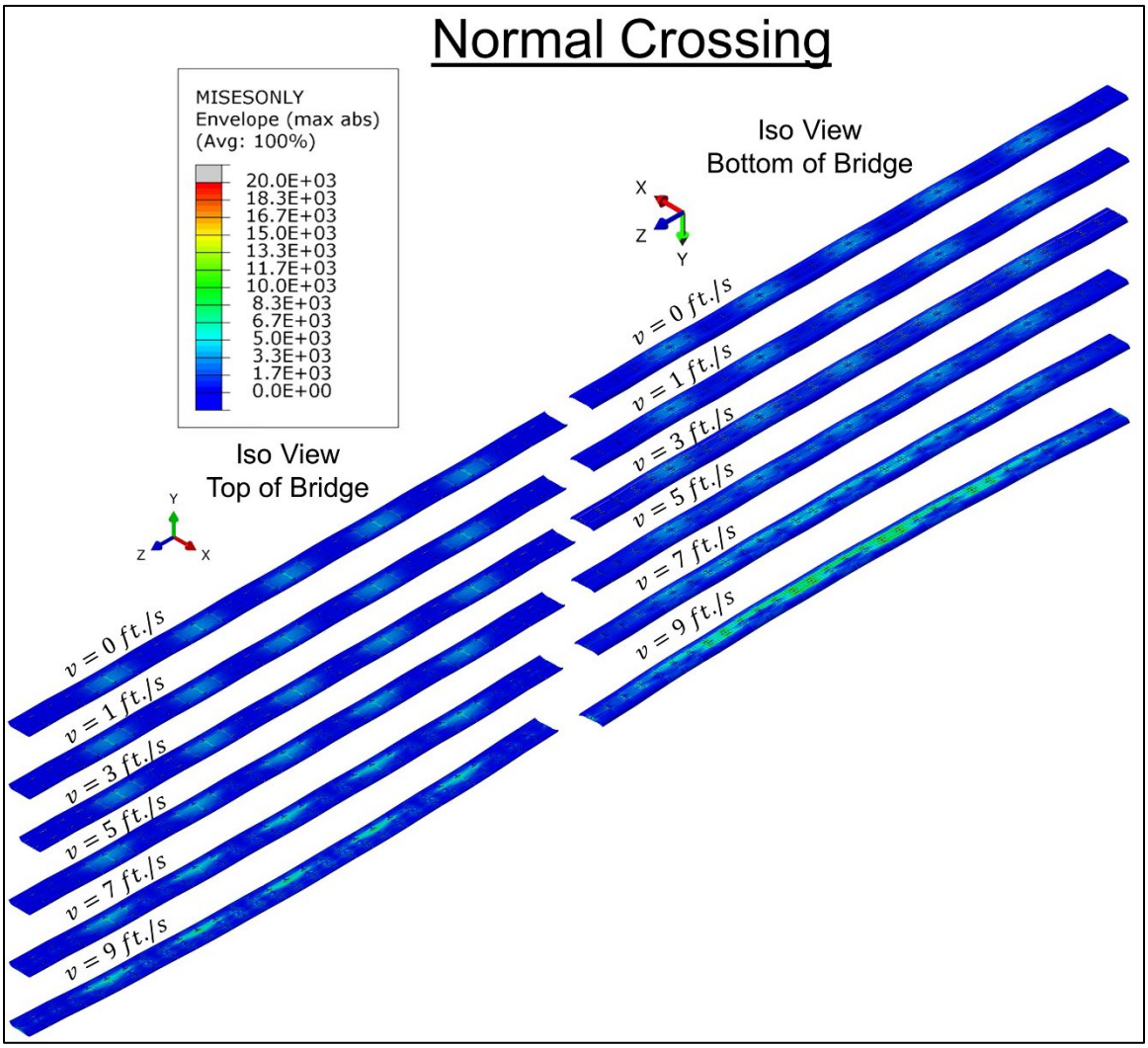
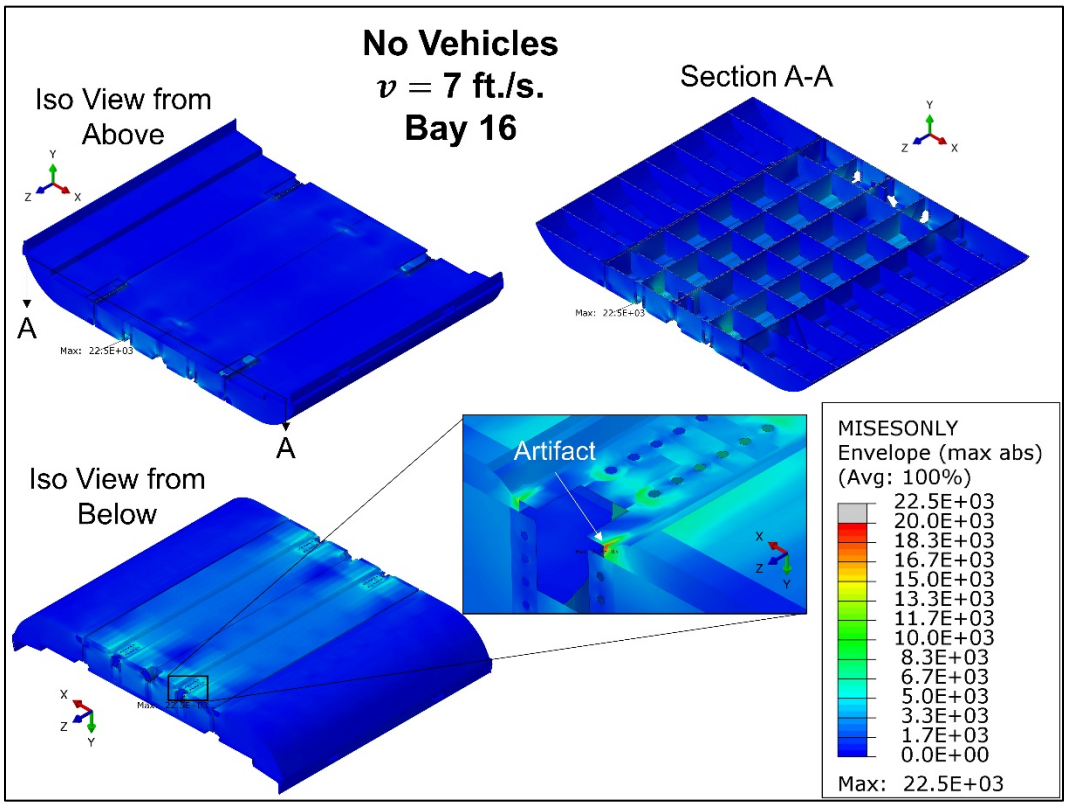


Figure 83. Contour plots of von Mises stress in the aluminum structure over a range of current velocities for the 210 m (30-bay) normal crossing. The images on the left and right view the bridge from above and below, respectively. Flow is in the $+x$ direction.



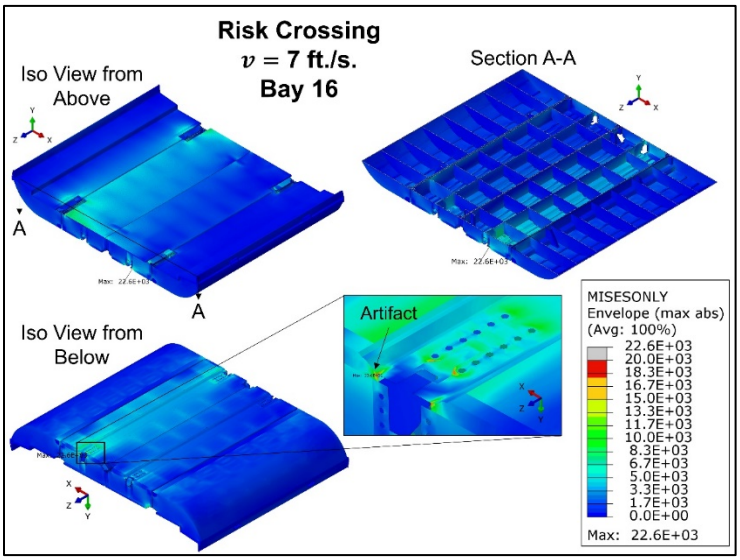
For each of the three vehicle loading cases, the two bays in the center of the bridge (bays 15 and 16) experienced the highest stresses with equal magnitudes. Figure 84 shows the von Mises stress in bay 16 for the no-vehicles crossing with a current velocity of 7 ft/s. This was the maximum safe current speed determined in section 4.3.4.1. As shown in Figure 84, a modeling artifact produced a highly localized peak stress of 22.5 ksi at a location on the bottom flange near the main coupling. Nowhere in the aluminum structure does the stress exceed the 24 ksi allowable including the location of the modeling artifact. Therefore, structural yielding of the aluminum is not a concerning failure mode.

Figure 84. Von Mises stress in the aluminum structure of the most highly stressed bay (bay 16) for the 210 m (30-bay) no-vehicles, $v = 7$ ft/s scenario.



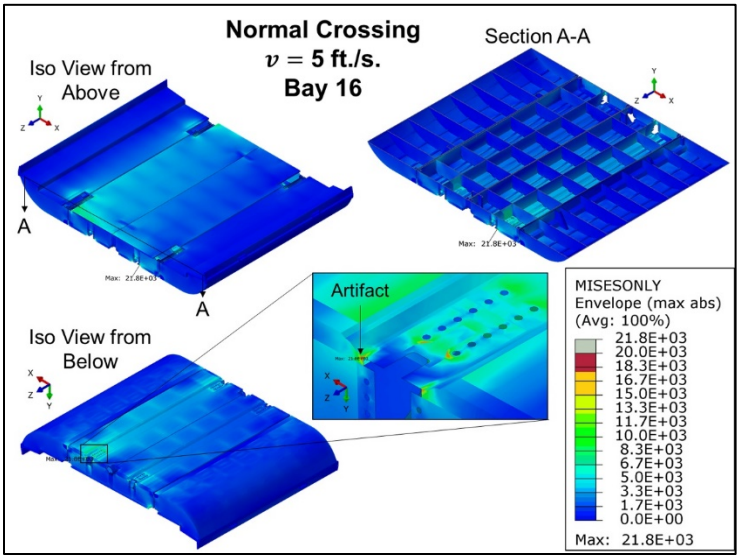
For the 30-bay risk crossing, the highest stresses were also located in the two center bays. The von Mises stress in the aluminum structure of bay 16 for its maximum safe current speed ($v = 7$ ft/s.) is shown in Figure 85. The same modeling artifact caused a stress overage with magnitude 22.6 ksi. Nowhere in the aluminum structure does the stress exceed the 24 ksi allowable, including the location of the modeling artifact. Therefore, structural yielding of the aluminum is not a concerning failure mode for the risk crossing.

Figure 85. Von Mises stress in the aluminum structure of the most highly stressed bay (bay 16) for the 210 m (30-bay) risk-crossing, $v = 7$ ft/s scenario.



For the 30-bay normal crossing, the highest stresses were also located in the two center bays (bay 15 and bay 16). Figure 86 shows the von Mises stress in the aluminum structure of bay 16 for its maximum safe current speed, which was determined in Section 4.3.4.1 to be $v = 5$ ft/s. The peak stress was found to be 21.8 ksi, which is below the 24 ksi allowable. Therefore, structural yielding of the aluminum is not a concerning failure mode for the normal crossing.

Figure 86. Von Mises stress in the aluminum structure of the most highly stressed bay (bay 16) for the 210 m (30-bay) normal-crossing, $v = 5$ ft/s scenario.



4.3.4.3 Main coupling clevis/eye stress analysis

In Section 4.1.3, it was determined that the allowable von Mises stress for the steel IRB components is $\sigma_{\alpha.Stl} = 121.5$ ksi. In Section 4.3.4.1, it was determined that the maximum safe current speeds for the three vehicular loading scenarios based on the main coupling pin allowable. These limit states were provided in Table 13. In this section, the steel main couplings were examined to ensure that the stresses in these components do not exceed the allowable limit of $\sigma_{\alpha.Stl}$ =121.5 ksi.

For the 210 m crossing, the most highly stressed connection for all three vehicular load cases was downstream connector 15. Connection 15 is at the mid-span of the 30-bay IRB. That connection would be expected to carry the largest load.

For the no-vehicles crossing, the maximum safe current speed was previously determined to be 7 ft/s. Figure 87 shows the von Mises stress in downstream connector 15 for 7 ft/s current velocity with no vehicular loads on the IRB. The peak von Mises stress is only 55.1 ksi and is extremely localized. Thus, yielding in the main coupling is not a concern for the no-vehicles scenario.

Figure 87. (a) Isometric view with transparency and (b) isometric view from below showing von Mises stress in the most highly stressed main coupling (downstream connection 15) for the 210 m (30-bay) no-vehicles, $v = 11$ ft/s scenario.

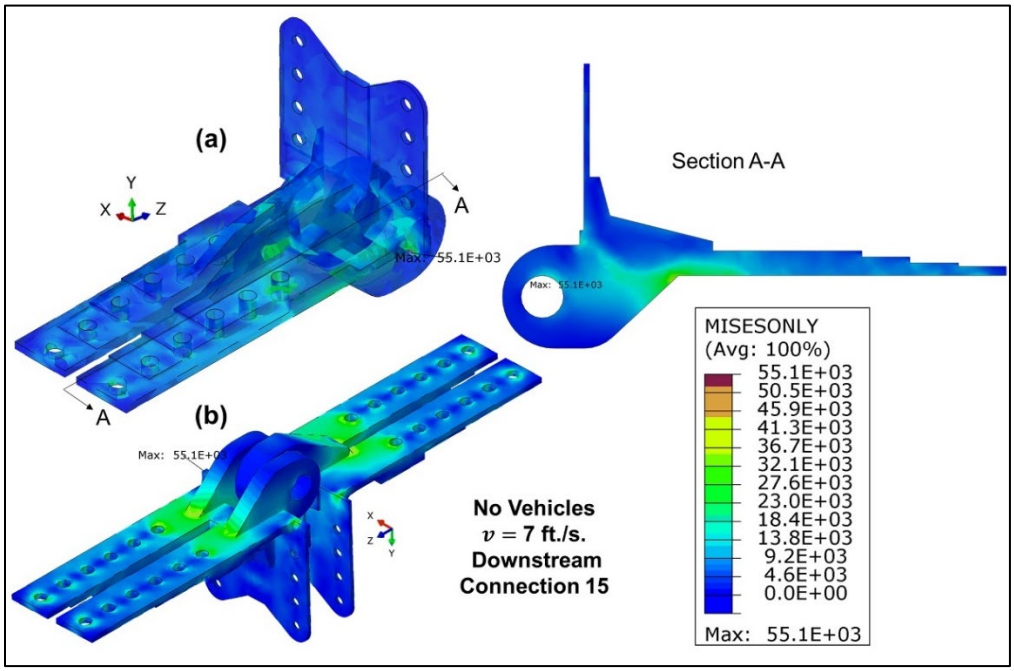


Figure 88 shows the von Mises stress in downstream connector 15 for the risk crossing and a current velocity of 7 ft/s. The peak stress in the steel is 78.5 ksi and is highly localized. As seen in the section view, the average non-localized stress in the section is well below the 121.5=ksi allowable limit.

Figure 89 shows the von Mises stress in downstream connector 15 for the normal crossing for its maximum safe current velocity of 5 ft/s. Here, the peak stress in the steel is 76.4 ksi. Yielding of the main coupling is not a concern in either case considering the allowable limit is $\sigma_{\alpha.Stl} = 121.5$ ksi.

Figure 88. (a) Isometric view with transparency and (b) isometric view from below showing von Mises stress in the most highly stressed main coupling (downstream connection 15) for the 210 m (30-bay) risk-crossing, $v = 9$ ft/s scenario.

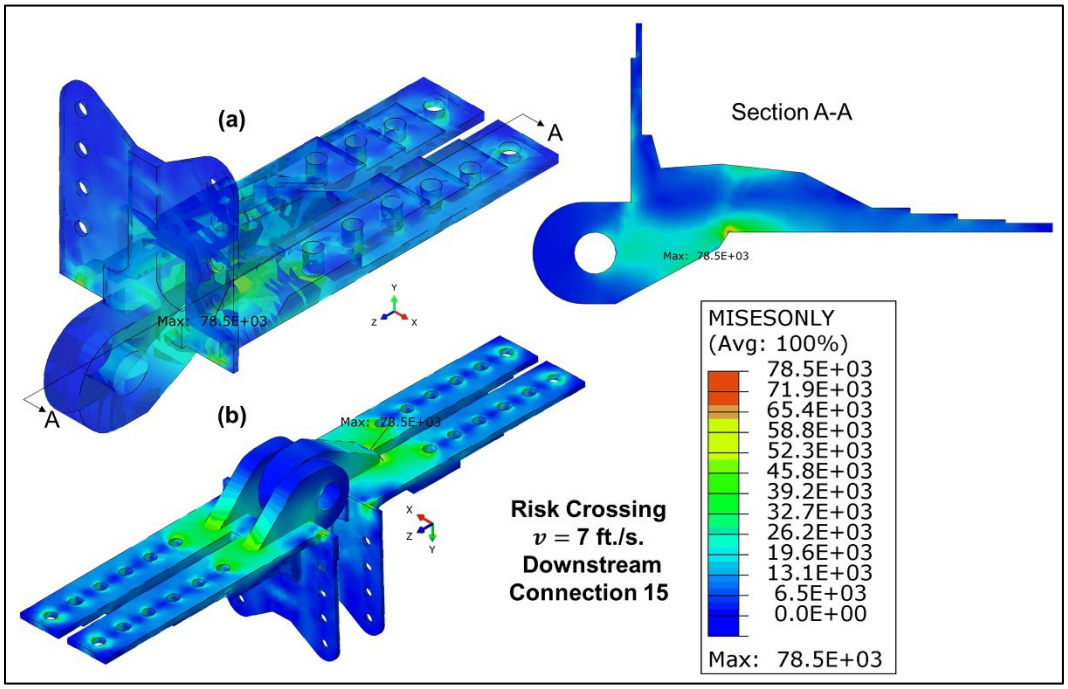
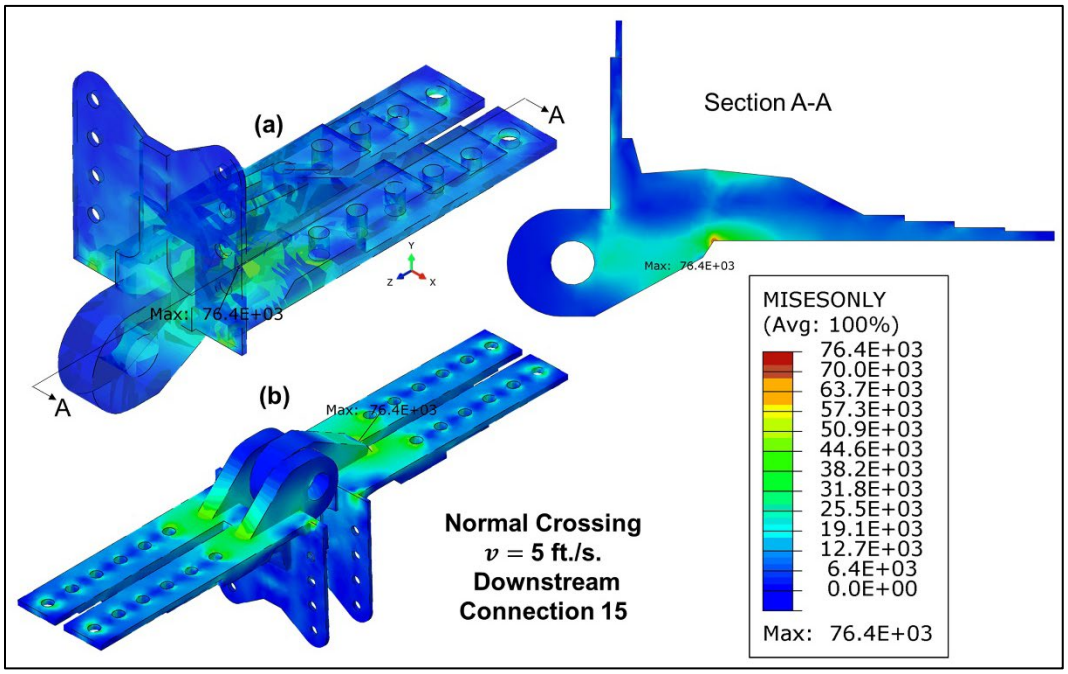


Figure 89. (a) Isometric view with transparency and (b) isometric view from below showing von Mises stress in the most highly stressed main coupling (downstream connection 15) for the 210 m (30 bay) normal-crossing, $v = 9$ ft/s scenario.



5 Summary and Conclusions

Table 14 summarizes the IRB structural M&S analyses performed in this study. In all of the M&S analysis cases, the bridge is assumed to be anchored at each end with no intermediate support, similar to a simply supported beam. Also, current flow is assumed to be transverse to the bridge and uniform across the span.

Table 14. Summary of IRB structural M&S analyses.

Crossing Span	Vehicle Crossing Type	Current Speed (ft/s)
110 m (15 interior bays)	No Vehicles	0, 1, 3, 5, 7, 9, 11, 15
	Risk Crossing†	0, 1, 3, 5, 7, 9, 11, 15
	Normal Crossing‡	0, 1, 3, 5, 7, 9, 11, 15
210 m (30 interior bays)	No Vehicles	0, 1, 3, 5, 7, 9, 11
	Risk Crossing†	0, 1, 3, 5, 7, 9
	Normal Crossing‡	0, 1, 3, 5, 7, 9

† One 72-ton vehicle, centered on the bridge.

‡ Multiple 72-ton vehicles on bridge; one vehicle centered on the bridge, remaining vehicles spaced ~100 ft apart.

The results of this work are summarized in Table 15. The current speeds listed in Table 15 represent the limit states for a 110 m and 210 m IRB. These are the maximum current speeds analyzed where the loads/stresses on the IRB did not exceed allowable values. Table 16 presents these same results in a visual format. The user can quickly determine the permissible crossing conditions for a given IRB crossing span and water current speed from Table 16.

Table 15. Maximum water current speeds for no-vehicle, risk-crossing, and normal-crossing conditions.

Crossing Span	Vehicle Crossing Type		
	No Vehicles	Risk Crossing	Normal Crossing
110 m	11 ft/s	9 ft/s	9 ft/s
210 m	7 ft/s	7 ft/s	5 ft/s

Table 16. Permissible crossing conditions for 110 m and 210 m IRB spans based on water current speed.

Crossing Span	Current Speed						
	1 ft./s	3 ft./s	5 ft./s	7 ft./s	9 ft./s	11 ft./s	>11 ft./s
110 m	Normal	Normal	Normal	Normal	Normal	No Vehicles	No Crossing
210 m	Normal	Normal	Normal	Risk	No Crossing		

Key conclusions from this work include the following:

- A structural, 3D CAD model of an IRB was developed and verified to have an accurate mass distribution.
- A structural FEM of an IRB, with the capability of accessing structural responses due to vehicular and/or hydrodynamic loadings, was developed and validated.
- The weight of a 72-ton vehicle is effectively distributed over approximately six IRB bays under equilibrium conditions. IRB bays outside of this zone of influence experience near-zero load.
- A method for determining the total drag force on an IRB as a function of current velocity was developed, which can be used to evaluate anchorage requirements if the bridge is anchored only at each end. The drag force versus current velocity plots for the 110 m and 210 m IRBs are provided in Figure 53 and Figure 74, respectively.
- Overall, the IRB design is very robust and capable of withstanding significant hydrodynamic and vehicular loadings.
- The main coupling pins that function to connect IRB bays are deliberately the weakest element in the IRB design. In the event of an overload, a pin failure would not compromise the watertight integrity of the IRB.
- A 110 m IRB has the structural capacity to withstand currents up to 11 ft/s with no vehicles on the bridge.
- A 110 m IRB has the structural capacity to withstand a ~MLC 70 normal crossing in currents up to 9 ft/s.
- A 210 m IRB has the structural capacity to withstand a ~MLC 70 risk crossing in currents up to 7 ft/s.
- A 210 m IRB has the structural capacity to withstand a ~MLC 70 normal crossing in currents up to 5 ft/s.

References

ASTM International. 2011. *Standard Test Methods for Tension Testing of Metallic Materials*. ASTM-E8. West Conshohocken, PA: ASTM International.

Bryant, D. B., J. Sharp, and C. Kees. 2019. *Hydrodynamics of the Improved Ribbon Bridge*. ERDC/CERL TR-12-24. Vicksburg, MS: US Army Engineer Research and Development Center.

Dassault Systèmes. 2016. *Solidworks Premium 2016 x64 Edition* [computer software]. Waltham, MA: Dassault Systèmes. https://www.solidworks.com/

Dassault Systèmes Simulia Corp. 2017. *Abaqus/CAE 2017* [computer software]. Providence, RI: Dassault Systèmes Simulia Corp. https://www.3ds.com/fileadmin/PRODUCTS/SIMULIA/PDF/datasheets/simulia-abaqus-cae-datasheet.pdf

Department of the Army. 2003a. *Bridge Anchorage*. WP 0035. *Operator's Manual for Improved Ribbon Bridge (IRB)*. TM 5-5420-278-10. Washington, DC: Department of the Army Headquarters and the Air Force. http://www.combatindex.com/store/tech_man/Sample/BRIDGES/TM_5-5420-278-10.pdf

Department of the Army. 2003b. *Unit, Direct Support, and General Support Maintenance Manual for Improved Ribbon Bridge (IRB), Change No. 1*. TM 5-5420-278-24&P. Washington, DC: Department of the Army Headquarters. http://www.combatindex.com/store/tech_man/Sample/BRIDGES/TM_5-5420-278-24_P.pdf

Department of the Army. 2009. *Engineer Operations - Brigade Combat Team and Below*. FM 3-34.22. Washington, DC: Department of the Army Headquarters. https://archive.org/details/ost-military-doctrine-fm3_34x22

Maddux, G. E., L. A. Vorst, F. J. Giessler, and T. Moritz. 1969. *Stress Analysis Manual*. AFFDL-TR-69-42. Dayton, OH: Air Force Flight Dynamics Laboratory. https://apps.dtic.mil/dtic/tr/fulltext/u2/759199.pdf

Trim, M. W., and R. E. Bennett. 2020. *Improved Ribbon Bridge Structural Response Validation Testing*. ERDC/GSL TR-20-22. Vicksburg, MS: US Army Engineer Research and Development Center.

US Army Tank-Automotive & Armaments Command. 1996. *Trilateral Design and Test Code for Military Bridging and Gap-Crossing Equipment*. Warren, MI: US Army Tank-Automotive & Armaments Command.

Unit Conversion Factors

Multiply	By	To Obtain
degrees (angle)	0.01745329	radians
feet	0.3048	meters
foot-pounds force	1.355818	joules
inches	0.0254	meters
inch-pounds (force)	0.1129848	newton meters
microinches	0.0254	micrometers
microns	1.0 E-06	meters
pounds (force)	4.448222	newtons
pounds (mass)	0.45359237	kilograms
square inches	6.4516 E-04	square meters
tons (2,000 pounds, mass)	907.1847	kilograms

Acronyms and Abbreviations

3D	three-dimensional
BEB	bridge erection boats
CAD	computer-aided design
ERDC	US Army Engineer Research and Development Center
FEM	finite element model
GPS	Global Positioning System
IRB	Improved Ribbon Bridge
M&S	modeling and simulation
MPC	multi-point constraint
MRBC	multirole bridge company
RRAD	Red River Army Depot

REPORT DOCUMENTATION PAGE

Form Approved
OMB No. 0704-0188

The public reporting burden for this collection of information is estimated to average 1 hour per response, including the time for reviewing instructions, searching existing data sources, gathering and maintaining the data needed, and completing and reviewing the collection of information. Send comments regarding this burden estimate or any other aspect of this collection of information, including suggestions for reducing the burden, to Department of Defense, Washington Headquarters Services, Directorate for Information Operations and Reports (0704-0188), 1215 Jefferson Davis Highway, Suite 1204, Arlington, VA 22202-4302. Respondents should be aware that notwithstanding any other provision of law, no person shall be subject to any penalty for failing to comply with a collection of information if it does not display a currently valid OMB control number.
PLEASE DO NOT RETURN YOUR FORM TO THE ABOVE ADDRESS.

1. REPORT DATE	2. REPORT TYPE	3. DATES COVERED *(From - To)*
April 2020	Final Report	

4. TITLE AND SUBTITLE
Structural Analysis of an Improved Ribbon Bridge Subjected to Hydrodynamic and Vehicular Loading

5a. CONTRACT NUMBER

5b. GRANT NUMBER

5c. PROGRAM ELEMENT NUMBER

6. AUTHOR(S)
M. Wesley Trim and Joseph A. Padula

5d. PROJECT NUMBER
Project 464569

5e. TASK NUMBER

5f. WORK UNIT NUMBER

7. PERFORMING ORGANIZATION NAME(S) AND ADDRESS(ES)
Geotechnical and Structures Laboratory
US Army Engineer Research and Development Center
3909 Halls Ferry Road
Vicksburg, MS 39180-6199

8. PERFORMING ORGANIZATION REPORT NUMBER
ERDC/GSL TR-20-13

9. SPONSORING/MONITORING AGENCY NAME(S) AND ADDRESS(ES)
Assistant Product Manager/Project Officer
Office of the Product Manager, Bridging
SFAE-CSS-FP-H, Bldg 230, Mail Stop #401
6501 East 11 Mile Road
Warren, MI 48397-5000

10. SPONSOR/MONITOR'S ACRONYM(S)
N/A

11. SPONSOR/MONITOR'S REPORT NUMBER(S)

12. DISTRIBUTION/AVAILABILITY STATEMENT
Approved for public release; distribution is unlimited.

13. SUPPLEMENTARY NOTES
US Army, PdM Bridging; MIPR 11326139

14. ABSTRACT

Structural modeling and simulations were performed to determine limit states of an Improved Ribbon Bridge (IRB) subjected to hydraulic and vehicle loadings. Measurements of as-built IRB bays were used to construct a three-dimensional, computer-aided design model. The model was used to create a computational finite element model (FEM) that was validated through correlations of simulation results and empirical data. The validated FEM was used to establish limit states (i.e., maximum current and vehicular loading conditions for 110 and 210 m IRB crossings).

Analyses revealed that the primary structural failure mode was yielding in the steel pins that link IRB bays. Assuming the IRB is adequately restrained at the shores, a 110 m IRB can withstand currents up to 11 ft/s with no vehicle traffic; a 210 m IRB can endure up to 7 ft/s under the same conditions. For risk crossings, one Military Load Classification-70 vehicle on the bridge, 110 and 210 m IRBs can tolerate currents up to 9 and 7 ft/s, respectively. Under normal crossing conditions vehicle spaced 100 ft apart, a 110 m IRB has the structural capacity to endure currents up to 9 ft/s; the maximum current for a 210 m IRB is 5 ft/s.

15. SUBJECT TERMS
Hydrodynamics, Matting, Military bridges, Stream crossing, Military, Structural analysis (Engineering), Transportation, Military

16. SECURITY CLASSIFICATION OF:			17. LIMITATION OF ABSTRACT	18. NUMBER OF PAGES	19a. NAME OF RESPONSIBLE PERSON
a. REPORT	b. ABSTRACT	c. THIS PAGE			Wesley Trim
Unclassified	Unclassified	Unclassified	SAR	119	19b. TELEPHONE NUMBER *(Include area code)* 601-634-2701